

SURPRISING IMPROVEMENTS IN LITHIUM ION AND SODIUM ION BATTERY CYCLE LIFE

by

Haonan Yu

Submitted in partial fulfilment of the requirements
for the degree of Master of Science

at

Dalhousie University
Halifax, Nova Scotia
November 2019

© Copyright by Haonan Yu, 2019

TABLE OF CONTENTS

LIST OF TABLES.....	v
LIST OF FIGURES.....	vi
ABSTRACT	viii
LIST OF ABBREVIATIONS AND SYMBOLS USED	ix
ACKNOWLEDGEMENTS	xii
CHAPTER 1 INTRODUCTION	1
1.1 Lithium ion batteries	1
1.2 Operation of lithium ion batteries	2
1.3 Lithium Ion battery electrodes	3
1.3.1 Lithium Ion battery positive electrodes.....	3
1.3.2 Negative electrodes.....	3
1.4 Li-Ion battery binders and electrolytes	5
1.4.1 Liquid electrolytes	5
1.4.2 Lithium salts	6
1.4.3 Additives	7
1.4.4 All solid-state-electrolytes	8
1.5 Electrolyte/Electrode interfaces and SEI	9
1.5.1 The origin of SEI.....	9
1.5.2 SEI characterization	9
1.5.3 SEI impact on cell life.....	11
1.6 Degradation and aging of LIB.....	11
1.6.1 Electrolyte failure	12
1.6.2 Electrode failure.....	13
1.6.3 Age predictions for LIB.....	15
1.7 Sodium ion batteries (SIB)	16
1.7.1 Electrodes for SIB	17
CHAPTER 2 EXPERIMENTAL TECHNIQUES	20
2.1 X-ray Diffraction (XRD)	20
2.1.1 X-ray theory	20
2.1.2 Braggs' law and the Scherrer equation	21
2.1.3 XRD sample preparation	22
2.2 Electron microprobe measurements	23

2.3	Fourier-transform infrared spectroscopy.....	24
2.4	Electrochemical techniques.....	25
2.4.1	Introduction	25
2.4.2	Electrode fabrication	26
2.4.3	Conflat cell fabrication and characterization	27
2.4.4	Coin cell fabrication.....	27
2.4.5	Electrochemical characterization	29
2.5	The gas bubbler.....	30
2.6	Karl Ficsher titration.....	31
CHAPTER 3 THERMOACTIVATION OF COBALT OXIDE IN SIB		33
3.1	Introduction.....	33
3.1.1	The conversion reactions.....	33
3.1.2	The goal of this work	34
3.2	Experimental.....	35
3.2.1	Electrode preparation.....	35
3.2.2	Conflat cell assembly	35
3.2.3	Electrochemical characterization	36
3.3	Results and discussion.....	36
3.3.1	CB/PI Electrochemistry	36
3.3.2	CoO Electrochemistry	37
3.3.3	Thermoactivation of CoO.....	38
3.3.4	Activation of CoO by Ball milling	40
3.3.5	Electrochemistry of Ball milled CoO	41
3.3.6	Thermoelectrochemical Activation of Ball milled CoO.....	44
3.4	Conclusions.....	47
CHAPTER 4 THE IMPACTS OF CARBON DIOXIDE ADDITIVES ON SILICON ALLOY CELLS.....		48
4.1	Introduction.....	48
4.2	Experimental.....	49
4.3	Results and discussion.....	50
4.4	Conclusions.....	57
CHAPTER 5 ENHANCING NMC/SILICON ALLOY FULL CELL CYCLING BY ADDING WATER TO THE ELECTROLYTE		58
5.1	Introduction.....	58

5.2	Experimental.....	59
5.3	Results and discussions	62
5.3.1	NMC-graphite full cells	62
5.3.2	Karl Fischer results.....	63
5.3.3	NMC-silicon alloy full cells	64
5.3.4	GC results.....	66
5.4	Conclusions.....	67
CHAPTER 6 CONCLUSIONS AND FUTURE WORK		68
6.1	Conclusions.....	68
6.2	Ongoing future work.....	69
REFERENCES		71
APPENDIX THE COPYRIGHT PERMISSION LETTER		82

LIST OF TABLES

Table 1.1	Some physical properties of common carbonates	5
Table 1.2	The chemical structure of common additives	7
Table 4.1	Solubility of CO ₂ in different solvents with 1 M LiPF ₆ electrolyte	54
Table 5.1	Major parameters of all electrode coatings used	61
Table 5.2	Karl Fischer results of samples with different water contents	63

LIST OF FIGURES

Figure 1.1	Schematic model of lithium ion battery cell	2
Figure 1.2	Schematic presentation of SEI	9
Figure 1.3	Proposed mechanism for the oxidation of EC with reactive oxygen.....	12
Figure 1.4	Cross-section images of dendrite growth	14
Figure 1.5	Comparison of charge/discharge curves of Li/LiCoO ₂ and Na/NaCoO ₂ cells	16
Figure 1.6	a) O3 and b) P2 structure of sodium transition metal oxide cathode materials.....	17
Figure 2.1	Illustration of the Bragg's law of diffraction.....	21
Figure 2.2	The gas tight XRD holder for air-sensitive samples with a zero-background silicon wafer	22
Figure 2.3	Block diagram of an FTIR instrument.....	24
Figure 2.4	The two electrode conflat cell model and actual image.....	27
Figure 2.5	Components of half coin cells (a) and full coin cells (b).....	27
Figure 2.6	A flow chart showing full coin cell assembly with an aligner	29
Figure 2.7	Sketch of the CO ₂ bubbler device: a ₁ is a three-way valve, a ₂ is a two-way valve and b ₁ is the bubbler. The dashed rectangles indicate where the handle will turn during the measurement.....	30
Figure 3.1	Potential vs capacity curve of the first three cycles of TiN/CB/PI electrodes in sodium half cells (a) at 30°C and (b) 60°C	36
Figure 3.2	Potential vs capacity curves of the first three cycles of cr-CoO/CB/PI electrodes in sodium half cells (a) at 30°C and (b) 60°C	37
Figure 3.3	Potential vs capacity curve of a thermoelectrochemically activated cr-CoO/CB/PI electrode in a sodium half-cell. The first sodiation (black) was conducted at 60°C and subsequent cycling (red) was conducted at 30°C in a fresh cell	38
Figure 3.4	Cycling performance of cr-CoO electrodes cycling at 30°C, at 60°C, and thermoelectrochemically activated (TA) cr-CoO electrode (sodiated at 60°C then placed in a fresh cell at 30°C). Closed symbols: sodiation, open symbols: desodiation.....	39
Figure 3.5	The XRD patterns of cr-CoO powder and bm-(CoO/CB)	40
Figure 3.6	Potential vs capacity curves of the first three cycles of bm-(CoO/CB)/PI electrodes in sodium half cells at (a) 30°C and (b) 60°C.....	41
Figure 3.7	XRD patterns of cr-CoO/CB/PI electrodes: as made, after sodiation at 30°C and after sodiation at 60°C. The purple star represents the impurity	42

Figure 3.8	SEM images of cross sections of (a) the as-made cr-CoO electrode, and (b) the TA cr-CoO electrode.....	43
Figure 3.9	Voltage curve of a thermoelectrochemically activated bm-(CoO/CB)/PI electrode in a sodium half-cell. The first sodiation (black) was conducted at 60°C and subsequent cycling (red) was conducted at 30°C in a fresh cell	44
Figure 3.10	Cycling performance of bm-(CoO/CB) electrodes cycling at 30°C, at 60°C, and a thermoelectrochemically activated (TA) bm-(CoO/CB) electrode (sodiated at 60°C then placed in a fresh cell at 30°C). Closed symbols: sodiation, open symbols: desodiation	45
Figure 3.11	Rate performance study of the (TA) bm-(CoO/CB) electrode.....	46
Figure 4.1	IR spectra of 1 M LiPF ₆ in EC/DEC solutions without CO ₂ and saturated with CO ₂	50
Figure 4.2	IR spectrum of ethanol.....	51
Figure 4.3	CO ₂ solubility results from FTIR and weight variation methods in PC(a) and EC:PC 1:1 (b), respectively. Fitted trendlines are added as a guide to the eye.....	52
Figure 4.4	CO ₂ solubility in EC/DEC 1:2 solvent with 1 M of LiTFSI and LiPF ₆ salt mixtures, where x is the mole fraction of LiPF ₆	53
Figure 4.5	Cycling performance of V6 Electrodes in 1 M LiPF ₆ in EC:DEC electrolytes saturated with CO ₂ and without CO ₂ . Cells with FEC additives are also shown for comparison.....	55
Figure 4.6	CO ₂ solubility in EC/DEC 1:2 solvent with 10%, 15%, 18% DETA including the molecular sketch of DETA. The red cross marks the value without DETA. The dashed line indicates the beginning of phase separation.....	56
Figure 5.1	The cycling performances of NMC-graphite without aligning, aligner, and hand made graphite. Letter C indicates these electrodes are from Novonix commercial NMC-graphite pouch cells. The data of pouch cells cycling is from the Novonix company.....	62
Figure 5.2	The cycling performance of NMC-V6/SFG6L full cells with different additives. The N/P ratio is 1.13.....	64
Figure 5.3	The cycling performance of LCO half cells (top) and NMC/V6-SFG6L vs LCO/V6-SFG6L full cells with and without water additive. (bottom) The N/P ratio is 1.13.....	65
Figure 5.4	The gas chromatograms of NMC-graphite pouch cells with and without 1000 ppm water. Green dash line indicates the CO ₂ standard sample. (The volume of sample is 10 μl) ...	66

ABSTRACT

Lithium ion battery research attracts much attention because lithium ion batteries have such extensive applications. Sodium ion batteries are an emerging field because of the sustainability of Na vs Li. However, issues regarding electrode and electrolyte degradation during cycling have hindered battery performance in both these technologies. In this thesis, thermoelectrochemical activation and ball milling methods were applied to improve the electrochemical performance of inactive CoO in sodium ion batteries. Results show that each method can increase the specific capacity and the combination of both methods can lead to a higher specific capacity and a stable cycling performance.

CO₂ has been shown to have great benefits on the cycle life of silicon alloy anodes. In this thesis, a new method was developed to measure CO₂ concentration in electrolyte quantitatively and accurately by FITR. It was shown that the CO₂ solubility in 1 M Li⁺ EC/DEC (1:2 v/v) solutions depends significantly on the salt anion and in a complicated manner. CO₂ scavengers like DETA can increase the CO₂ solubility effectively at a low concentration, but cause phase separation at higher concentrations.

Water was intentionally added to silicon alloy full cells and was found to improve cycling when NMC was used as the cathode, but minimal impacts when Lithium cobalt oxide was the cathode. Cells with 1000 ppm water additive exhibit similar enhancement as 10% FEC on the cycle life of silicon alloy full cells.

LIST OF ABBREVIATIONS AND SYMBOLS USED

Å	Angstrom as the unit of length
Ah/L	Ampere hour per liter
bm	Ball mill
BMF	Blown microfiber disk
°C	Celsius degree
CB	Carbon black
cr-CoO	Crystalline CoO
d	d spacing
DEC	Diethyl carbonate
DETA	Diethylenetriamine
DMC	Dimethyl carbonate
EC	Ethylene carbonate
EIS	Electrochemical impedance spectroscopy
EMC	Ethylmethyl carbonate
F	Faraday's constant
FEC	Fluoroethylene carbonate
FTIR	Fourier-transform infrared spectroscopy
GC-MS	Gas Chromatography–mass spectrometry
H	Full width at half maximum (FWHM) of a XRD peak
KFT	Karl Ficsher titration
LCO	Lithium cobalt oxide
LIB	Lithium ion batteries
LiBOB	Lithium bis(oxalato)borate
LiTFSI	Lithium bis(trifluoromethanesulfonyl)imide
M	Molarity

MW	Molecular weight
Na_aO_b	Metal oxide
NMC	$\text{Li}(\text{Ni}_x\text{Mn}_y\text{Co}_z)\text{O}_2$ ($x + y + z = 1$)
PAA	Polyacrylate
PC	Propylene carbonate
PEC	Polyethylene carbonate
PEO	Polyethylene oxide
PI	Polyimide
ppm	Parts-per notation (mg/L)
PTFE	Polytetrafluoroethylene
PVDF	Poly(vinylidene fluoride)
Q	The capacity
SC	Super C
SEI	Solid electrolyte interphase
SEM	Scanning electron microscope
SIB	Sodium ion batteries
STM	Scanning Tunneling Microscope
T	Temperature
TA	Thermoelectrochemically activated
T_m	Melting temperature
T_b	Boiling temperature
TMO	Transition metal oxides
V	Voltage
VC	Vinylene carbonate
wt %	Weight ratio
Wh/L	Watts hour per liter

XRD	X-ray diffraction
ϵ_r	Dielectric constant
η	Viscosity
Θ	The angle between incident beam and crystal planes
λ	Wavelength
μ	The chemical potential
τ	The average grain size

ACKNOWLEDGEMENTS

I want to express my highest gratitude to my supervisor Dr. Mark Obrovac for his academic support. His guidance, patience and insights helped me to complete my Master program. Because of him, I gained a lot of deep understandings about the battery field where I want to dedicate myself as my future career.

I would like to thank Dr. Timothy Hatchard for his help and profession in technical support. Then I have to thank the beloved Dr. Jeff Dahn. His excellence and innovative ideas opened my mind to solve problems from different perspectives. In addition, I would like to thank both Jeff and Dr. Gagnon to give me the access to the certain equipment. It will be impossible to finish the whole project without their participation.

I would also like to thank other staff like Dr. Todd Carter and Dr. John Noddin. They kindly helped me to fix the issues in my design and build critical tools in my experiments.

Certainly, I have to thank all current and previous colleagues in my lab. There were always good suggestions and assistance offering by them anytime I need. I had an amazing run and make many friends. These people are Lituo, Peiyu, Simeng, Zilai, Ben, Leyi(Roy), Scott, Jun, Yidan, Wei, Annie, Michael in no particular order.

Finally, special thanks to my parents, girlfriend and family. They motived me to finish the journey by their support and faith.

CHAPTER 1 INTRODUCTION

1.1 Lithium ion batteries

Demand for global electricity has grown rapidly over the last few decades. In Canada the annual electricity production was 19709 PJ in 2016, with over 70% of this energy being produced by fossil fuels. This results in enormous CO₂ emissions and accelerates climate change. Therefore, searching for renewable energy resources has drawn huge attention.

The efficient storage is necessary for continuous and renewable energy sources. Metal-ion batteries are expected to fulfill the request for energy storage devices. They are highly efficient, have stable cycling, and have high energy density. Based on these advantages, rechargeable metal-ion batteries, especially lithium ion batteries have been widely applied in advanced electrical vehicles and electronic devices for daily communication. The lithium ion batteries market has grown from \$15 billion in 2013 to \$45 billion in 2018.(1) This flourishing of lithium ion batteries has driven battery scientists to pursue greater achievements. One is the development of next generation lithium ion batteries in terms of longevity and high energy density in particular. As a result, energy density experienced a continuous improvement from 200 Wh/L in the first generation Li-ion batteries to 770Wh/L currently and is estimated to increase above 1000 Wh/L by 2050.

Another research focus is to minimize safety issues. Since lithium ion batteries were invented, their safety issues have never been fully resolved. Early lithium batteries suffered from internal shorts in the densely compacted battery structure or fires involving combustive organic solvents initiated by self-heating and thermal runaway. Yoshino(2) first invented the Li-ion cell by replacing lithium metal with stable graphite to prevent the formation of lithium dendrites. MacNeil et al.(3) subsequently pointed out that exponentially activated reactions are the main reason for thermal runaway and introduced a more complete safety standards for lithium ion batteries testing. Moving into the 21st century, numerous research efforts have made tremendous progress including redox shuttles, all solid-state electrolytes or novel cooling and monitoring systems for battery packs. All these techniques are dedicated towards achieving improved safety.

Another important research area is finding alternative metal ions that can be used in batteries instead of lithium. Lithium resources are thought to be insufficient for the growing demand for Li-ion batteries. Since Li constitutes only 0.4% of the earth's crust, the depletion of lithium resources is inevitable. Other alkali elements are ideal choices including sodium, magnesium and potassium, but metal-ion batteries based on these alternative metals are not competitive with lithium ion batteries yet in terms of overall performance.

1.2 Operation of lithium ion batteries

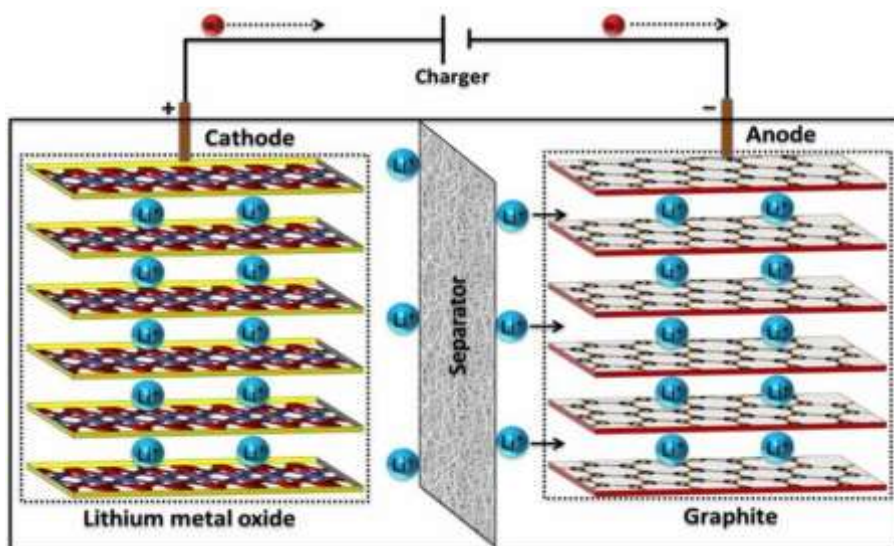


Figure 1.1 Schematic model of lithium ion battery cell. Copyright permission from T. Wegayehu, Y. Mulushoa, N.Murali , B.Vikram Babu, T.Arunamani, *Int. J. Adv. Res.*, **5**(4), 1658(2017).

A typical Li-ion cell consists of a cathode, anode, separators, and electrolyte as shown in Figure 1.1. The electrolyte can conduct ions between the cathode and anode where reduction and oxidation reactions occur. Meanwhile, electrons flow through the external circuit to balance the charge. Rechargeable Li-ion batteries are expected to have perfectly reversible charge/discharge reactions. When ions are removed from the host material of one electrode and intercalate into the other electrode, every component should ideally stay unchanged. The energy density of a lithium ion battery is related to its capacity and the potential difference between the cathode and anode, which are dominated by the properties of the active electrode materials.

1.3 Lithium Ion battery electrodes

1.3.1 Lithium Ion battery positive electrodes

Lithium ion battery electrodes act as either hosts or providers for lithium ions. For the cathode, during charging oxidation occurs as lithium ions are deintercalated from the material, while the whole process is reversed during discharge. Ideally, cathode materials should have stable structures during cycling and high volumetric capacity. LiCoO_2 and $\text{Li}(\text{Ni}_x\text{Mn}_y\text{Co}_z)\text{O}_2$ ($x + y + z = 1$) (NMC) are the most common types of cathode materials used commercially today. LiCoO_2 has an ordered rock-salt structure with cations located in alternating ordered planes where lithiation and delithiation can easily take place. Regardless of its amazing success, lithium cobalt oxide is questioned by its potential pollution to the environment and high production cost. LiNiO_2 shares a similar layer structure with lower cost for Ni, but LiNiO_2 has intrinsic issues of spontaneous reduction from Ni^{3+} to Ni^{2+} and H2-H3 phase transition, which causes severe capacity fade.(4) Therefore, alternatives such as NMC (mixture of Ni, Mn, and Co) were created. The substitution of three transition metals is expected to combine high capacity from LiNiO_2 , thermal stability from LiMnO_2 and energy density from LiCoO_2 . The electrochemical properties of NMC is determined by the ratio of the three elements. For instance, NMC111 (Ni:Mn:Co=1:1:1) has a very high specific capacity (~ 275 mAh/g), but the full extraction of lithium is limited by high upper cut off voltage.(5) On the other hand, NMC811, with a large Nickel content, is favorable with a lower voltage window for delithiation, although its capacity retention is worse than NMC111 because of Ni migration.

1.3.2 Negative electrodes

In contrast to the positive electrode, reduction reactions occur on the negative electrode during cells charging. Negative electrodes for lithium ion batteries should ideally have a high volumetric capacity, excellent cycling stability and a low operating voltage window. Graphite basically satisfies all the requirements above. It has relatively a high volumetric capacity (764 Ah/L), a low working potential(6) as well as excellent cycle life. In graphite, each hexagonal graphene layer has sp^2 orbitals, resulting in good electron conductivity. Between the graphene layers, highly mobile π electrons form van der Waals bonds that weakly attach all graphene layers.

Another popular negative electrode material is silicon and its alloys. Silicon is expected to be a promising candidate to supplement graphite in negative electrodes. It has several attractive properties; 1) its volumetric capacity is the second highest (2047Ah/L), lower only to lithium metal;(7) 2) its relatively low operation voltage of 0.3 V vs Li/Li⁺,(8) so studies on attempts to utilize silicon as negative materials have been conducted extensively. However, one major issue with silicon is its tremendous volume expansion of 270% of its initial size during lithiation as opposed to graphite, which only changes in volume by 10%. The large volume change of Si may cause severe structural damage and cell failure.

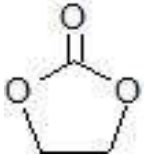
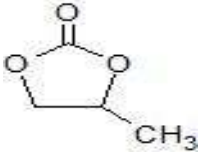
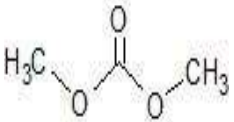
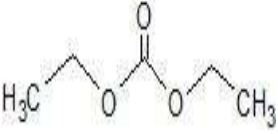
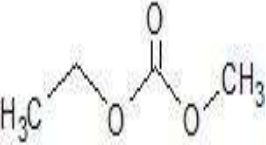
Many efforts have been made to minimize the volume expansion of Si negative electrodes. One method is to create advanced supporting structures. Either novel core-shell silicon nanowires designed by Chan et al.(9) or nanotubes from Song(10) were proven to reduce volume expansion dramatically,(11) so cells exhibited good capacity retention, but their high working potential and production cost made their commercialization nearly impossible. Other than nanomaterials synthesis, coatings, especially carbon coatings have been reported to modify the surface and prevent microcracks. However, a nonuniform carbon coating will decrease average kinetic energy of lithium ions and slow down the diffusion process.(12) In addition to coating, Si/C hybrid materials are also worthy of attention due to the combination of high electronic conductivity of carbon and high specific capacity of silicon.(13) Liu et al.(14) prepared a Si-C composite with a pomegranate structure. A conductive carbon layer encased a single Si nanoparticle and provided enough space for silicon contraction and expansion. The cycle life was improved by this structure comparing to pure silicon, but the purity control of Si/C products, especially on a big scale, is very difficult since SiC is almost undetectable in most of characterization tools.(15) Analogous to Si/C, alloys of silicon and other inactive phases (Fe, Mn and Co) can exhibit exceptional properties. In such alloys the volume expansion can be reduced to 105% with an 86% first cycle coulombic efficiency, and with less than 15% capacity loss after 150 cycles.(16)

1.4 Li-Ion battery binders and electrolytes

In order to achieve the best performance from lithium ions cells, the electrolyte choice is very critical. Li-ion battery electrolytes expected to have high electrochemical, thermal stability, and have a fast ion transportation rate. Since electrolytes are responsible for the transportation of ions between the positive and negative electrodes, they will inevitably interact with electrode surfaces to initiate parasitic reactions. The reaction products include gases, inorganic and organic species. Such reactions can result in volume expansion and capacity loss. Therefore, electrolytes are being developed with the aims to avoid irreversible reactions and increasing cell safety.

1.4.1 Liquid electrolytes

Table 1.1 Some physical properties of common carbonates.

Solvent	Structure	$T_m/T_b(^{\circ}\text{C})$	$\eta(\text{cP})$ 25 $^{\circ}\text{C}$	ϵ_r 25 $^{\circ}\text{C}$
EC		36.4/248 ^a	1.9(40 $^{\circ}\text{C}$) ^a	89.78(40 $^{\circ}\text{C}$) ^a
PC		48.4/242 ^b	2.53 ^b	64.92 ^b
DMC		4.6/91 ^c	0.59 ^c	3.1 ^c
DEC		74.3/126 ^d	0.75 ^d	2.8 ^d
EMC		-53/110 ^a	0.65 ^e	3.0 ^e

a Ref. 17(17) b Ref. 18(18) c Ref. 19(19) d Ref. 20(20) e Ref. 21(21)

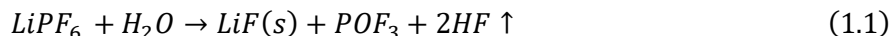
Liquid electrolytes comprise organic solvents with dissolved lithium salt.(22) The majority of solvents consist of combinations of binary or ternary organic esters and ethers. Different types of solvents have their own strengths, so solvent combinations can possibly bring all these advantages into one electrolyte. Several physical properties of common solvents in electrolyte are listed in Table 1. EC(Ethylene carbonate) is practically indispensable because of its superior electrochemical properties as shown in Table 1. EC has the highest dielectric constant, which can facilitate lithium salt dissolution, whereas its high viscosity can negate ion transportation. In contrast, these values are significantly lower for linear carbonates such as Dimethyl carbonate (DMC) or Diethyl carbonate (DEC). However, linear carbonates usually have a wider voltage stability window up to 5 V.(23) Therefore, cosolvents of EC with linear carbonates started to be applied in commercial lithium ions batteries in 1994,(24) and it received a huge success. It was reported that the merits of each solvent were imparted on the mixture including high ion transportation from EC and high voltage tolerance. This discovery set the theme for upcoming electrolyte design and currently, almost all electrolyte solvents for LIBs have been exclusively EC mixed with other types of linear carbonates.

Surprisingly, some recent studies started to question the need for EC in the electrolyte. Lin(25) pointed out that EC could decompose on the negative side and lead to capacity fade. Petibon et al.(26) used a small amount of vinylene carbonate (VC) as an additive or “enabler” to replace EC and a better cycling performance was shown. Additionally, Lin(25) tried a variety of additives as enablers and evaluated their individual performance, but their enabling mechanisms are still unknown so their adoptability to further commercialization of EC-free electrolytes is unclear.

1.4.2 Lithium salts

In contrast to the wide spectrum of solvent options in LIB electrolytes, there are only a few for lithium salts. The reason is that most simple anions fail to meet both requirements of solubility and oxidative stability simultaneously, so the majority of commercial lithium salts are made of complex anions such as LiClO_4 , LiAsF_6 , LiPF_6 , etc. LiPF_6 is the most successful lithium salt for the industry currently. Well-balanced properties and strong resistance to oxidation make it

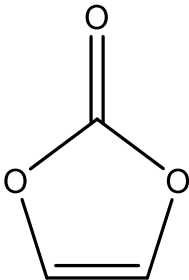
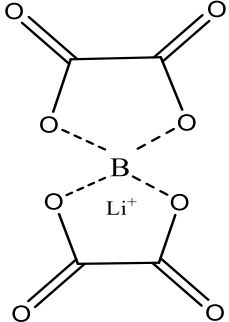
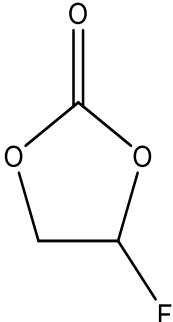
unrivaled when cells are charged above 5 V. However, its chemical instability and sensitivity to moisture can lead to cell failure. Some scientists(27) found that HF gas will be generated in the presence of tiny traces of moisture, as explained by equation 1.1, and cause capacity fade.



Another interesting trend is the use of salts with long chain complex anions, such as lithium bis(trifluoromethanesulfonyl)imide (LiTFSI). It has excellent thermal tolerance that can enable high temperature LIB operation. However, practical applications of LiTFSI are very limited since it causes corrosion on aluminum and its high production cost.(28)

1.4.3 Additives

Table 1.2 The chemical structure of common additives.

		
VC	LiBOB	FEC
Vinylene carbonate	lithium bis(oxalato)borate	Fluoroethylene Carbonate

The key to maintain the reverse chemical reactions in rechargeable batteries is the formation of a stable SEI (Solid Electrolyte Interphase).(29) One method to form a stable SEI is by adding additives to electrolytes. Previous work indicated that a tiny amount of electrolyte additives can affect the SEI composition immensely. Common electrolyte additives are shown in Table 1.2. For graphite anodes, VC and LiBOB were found to suppress the growth of the SEI layer by forming radical polymer products. This improved cycling performance.(30) Likewise, benefits from electrolyte additives were also observed on the silicon side. FEC or VC are almost necessary additives for achieving good cycle life in cells with silicon alloy electrodes. Especially for FEC, extra fluorine atoms are believed to enhance the SEI by preventing LiPF₆ decomposition.(31) However,

most studies on discovering the mechanism by which electrolyte additives work were conducted using theoretical simulations, so actual reaction pathways in real cells are still relatively unknown.

1.4.4 All solid-state-electrolytes

Eliminating the safety issues of liquid electrolytes and potentially enabling the use of Li metal electrodes are goals of all solid-state-electrolyte research. Conceptually, all solid-state-electrolytes use solid phase materials, predominately polymers, to replace flammable organic liquids. As noted in Armand's study, ion transportation in solid electrolytes relies on the movement of polymer chains and segments.(32) Therefore, solid electrolytes for LIB should be amorphous and extremely polar. The amorphous structure provides enough flexibility for the movement of polymer chains, and the high polarity enables a high concentration of lithium salt. Work on synthesis and characterization of solid states electrolytes has been done progressively including polyethylene oxide (PEO), polyethylene carbonate (PEC) and polytrimethylene carbonate, etc. PEO was the first solid polymer electrolyte discovered in 1979.(33) It has a uniquely low activation barrier for movement of polymer chains, but its semi crystallinity froze the polymer chains and completely impeded the ion transportation under room temperature. The ion conductivity of PEO-based electrolytes, which is a critical indicator for ion transportation abilities, is too slow for sufficient lithium migration in electrolytes with only $10^{-8} \text{ S}\cdot\text{cm}^{-1}$ at 25°C .(34) However, inspired by PEO work, researchers started to develop other polymers by modelling the structure of PEO. PEC was created by replacing the O-H groups with carbonate units to duplicate a carbonate polymer similar to liquid carbonate electrolytes. Its ion conductivity is excellent, lower than $10^{-4} \text{ S}\cdot\text{cm}^{-1}$, but the uncontrolled polymerization during the synthesis is impractical for large scale production. Another method is to dope PEO with nano-sized particles such as $\text{Al}_2\text{O}_3, \text{TiO}_2$.(35) The dispersal of nano particles was found to effectively decrease crystallinity of the PEO and improve the ion conductivity.(36) In spite of being immature technology, all solid electrolytes showed great potentials to solve issues of leaking and incineration from electrolytes, and hopefully, a safer and more reliable LIB will come upon us soon.

1.5 Electrolyte/Electrode interfaces and SEI

1.5.1 The origin of SEI

During the operation of LIB, parasitic reactions take place on the electrolyte-electrode interfaces throughout the whole cell lifetime. Some of the insoluble reaction products will deposit on the electrode surface forming a permanent layer called the SEI. The SEI typically starts to form in the range 1.7–0.5 V (Li vs Li⁺) and continues until the anode is fully lithiated.(37) However, its final form can vary dramatically by conditions in the cell such as the electrolyte solvent, active materials and cycling temperature.

1.5.2 SEI characterization

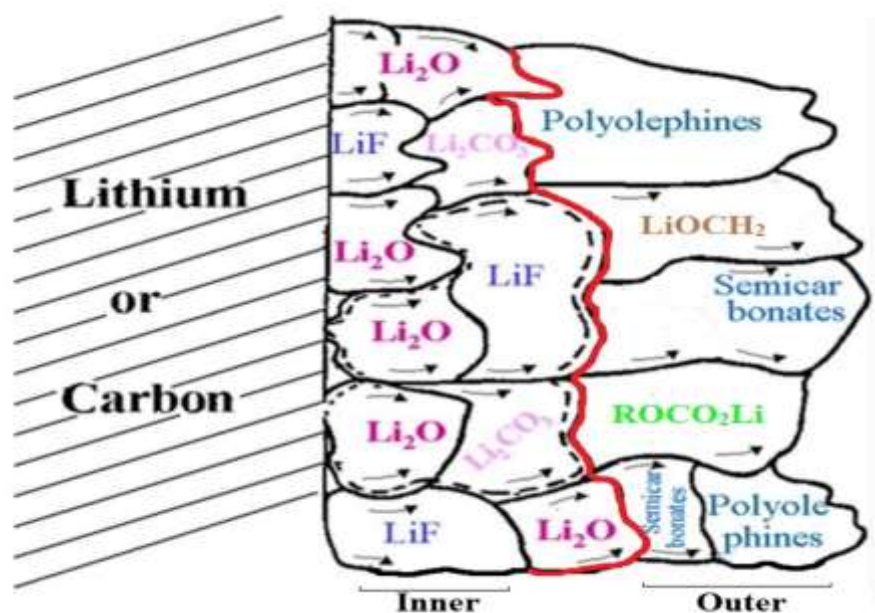


Figure 1.2 Schematic presentation of SEI. The red line indicates the separation between inner and outer regions. Copyright with permission from E. Peled, S. Menkin, *J. Electrochem. Soc.*, 164 (7), A1704 (2017).

It is generally believed that the SEI structure can be divided into an inner compact microphase and a outer porous layer. The inner layer usually has a higher density and crystallinity with a contoured structure, while the outer layer is relatively porous and amorphous.(38) Apart from the structural difference, the composition of the inner layer mainly consists of inorganic

compounds such as Li_2CO_3 or LiF ,⁽³⁹⁾ while the outer layer consists of polymers. A summary description of the SEI structure is outlined as Figure 1.2.

Experimentally, the SEI is very hard to observe because of its nano thickness and instability in air. Many groups^(40,41,42) attempted to prepare pure SEI after cycling for characterization, but impurities introduced by their ex-situ techniques undermined the creditability of their results. Besides direct visualization, great effort has gone into studies of SEI composition analysis. In-situ X-ray photoelectron spectroscopy (XPS) from McArthur⁽⁴³⁾ and vibrational spectroscopy study from Aurbach⁽⁴⁴⁾ gave a preliminary understanding about SEI composition and surface chemistry on carbon anodes at a variety of voltages. Another interesting technique is ellipsometry. As a surface sensitive tool, it can derive surface morphology by capturing the tiny polarization change between incident and reflected beams. McArthur et al.⁽⁴³⁾ applied this technique to silicon cells with and without electrolyte additives. Interestingly, he found that the interphase thicknesses increased with the presence of these additives, with an 18 nm thickness for baseline electrolyte versus 25 nm for 2% VC. However, the accuracy started to decrease when the technique was used for silicon alloy electrodes where multiple interference sources tended to overlap due to the massive structural change of the Si alloy.

The thickness of SEI is an important parameter to determine the overall cell performances. However, the exact thickness of the SEI is under debate. Results cover a wide range, from 5 to 500 nm, as measured by different experimental means. Electrochemical impedance spectroscopy (EIS)⁽⁴⁵⁾ is a universal tool to measure the SEI thickness where increasing impedance is related to the growth rate and thickness of the SEI. According to EIS work of Dahn and his coworkers, the thickness of the SEI layer keeps increasing, but at a decreasing rate $\left(\frac{dx}{dt}\right)$ during cycling. The rate can be estimated by equation 1.2 below.⁽⁴⁶⁾

$$\frac{dx}{dt} = \left(\frac{1}{2k}\right)^{\frac{1}{2}} t^{-\frac{1}{2}} \quad (1.2)$$

Here x, t, k represent thickness, reaction time, and a proportional constant, respectively. Dahn assumed that new surface areas are continuously exposed to the electrolyte by

unavoidable microstructural cracks. This contradicted the previous theory, which stated that SEI formation completes after the first cycle.(47)

1.5.3 SEI impact on cell life

It is generally believed that the SEI is essential for the successful operation of lithium ion batteries. A good SEI behaves as an electrically insulating layer on electrode surfaces to exclusively facilitate lithium ion transportation, indicating the cation transportation number close to unity. Besides, uniform and passivating SEI can reduce the concentration polarization and have a high tolerance to expansion stress.(48) Despite many benefits of a good SEI, the exact approach to form a good SEI has been a huge mystery since the final SEI formation can be affected by a number of factors. In the case of graphite with EC versus PC solvents, Aurbuch(49) demonstrated that an efficient SEI forms by fast kinetic solvents like EC. This was further explained by the rate constant in electron-host interactions called k_e in Peled's model.(37) In his theory, fast kinetic solvents will form SEI faster than their own cointercalation, so the chances for solvents to form good SEI will be more favorable. He then showed EC or CO₂(50) are excellent SEI precursors that form a stable and passivating SEI because of their large values of k_e . Similarly, FEC can form a passivating SEI on silicon surfaces to achieve better capacity retention. Schroder(51) showed that fast decomposition of FEC would create a fluorine rich SEI where lithium ion transportation is faster than normal SEI.

However, the SEI is a double-edged sword. Terrible SEI formation may also bring the end of cycle life. It was suggested that SEI stability will weaken in the presence of unstable polymers and carbonates like LiCH₂CH₂OCO₂Li.(49) These species tend to dissolve in electrolyte to form a new SEI in the replacement of old SEI. This ongoing transition will consume lots of lithium and eventually terminate cell life.

1.6 Degradation and aging of LIB

Unfortunately, LIB cells start to degrade and age as soon as they are assembled. Capacity loss occurs consistently throughout the cell lifetime regardless of the type of cells, but degradation mechanisms may vary significantly. Therefore, for the sake of a clear understanding, cell degradation can be discussed from three perspectives.

1.6.1 Electrolyte failure

According to results from previous studies, electrolyte instability is accountable for over 70% of cell failure.(52) Essentially, most non-aqueous electrolytes will be susceptible to a series of decomposition reactions. For example, EC can change into EMC during electrochemical reactions. Alkyl radicals, as one of reaction products, will likely propagate to start irreversible polymerization on the surface. As reported by Endo,(53) this polymer formation by alkyl radicals will occur consistently during cell cycling, leading to an unstoppable degradation of electrolyte components. In addition, elevated temperature will accelerate the rate of side reactions, resulting in an exponentially large impedance.(54)

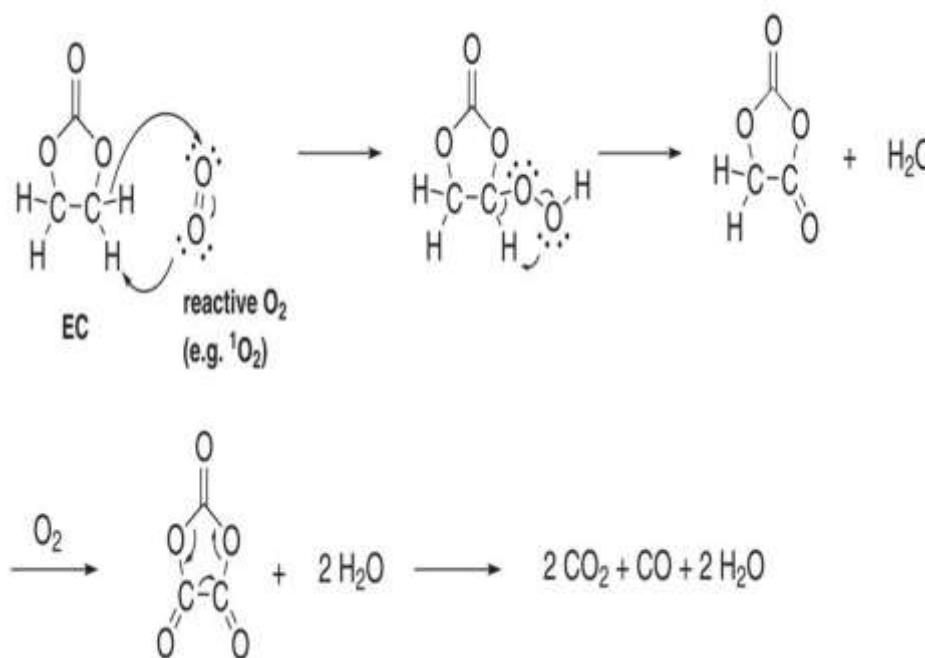


Figure 1.3 Proposed mechanism for the oxidation of EC with reactive oxygen. Reprinted with permission from R. Jung, M. Metzger, F. Maglia, C. Stinner, H.A. Gasteiger, *J. Electrochem. Soc.*, 164 (7), A1361 (2017).

Electrolytes for LIB are also very sensitive to the moisture or air. Reactions between electrolytes and water or oxygen are a major contributor to the formation of unwanted products. Most cathode materials will release gas during cycling, including H₂, O₂, CO₂, etc. Confirmed by

recent results, the pathway for CO/CO₂ emission actually begins from ring-opening reactions of EC with oxygen impurity. The free oxygen molecules will attack C-H bonds to break the ring then react with organic electrolytes to generate CO/CO₂ and the proposed pathway is indicated in Figure 1.3.

1.6.2 Electrode failure

Electrodes in LIB should maintain the same structure during cycling. However, irreversible structural changes can occur in real situations, which causes cell fade. For instance, LiMnO₂ was predicted to be a promising cathode material with exceptionally high capacity (250 mAh/g), but its spontaneous conversion from layered to spinel structure results in cell fade. Specifically, when LiMnO₂ is fully discharged, the Jahn-Teller distortion anisotropically changes the cubic spinel lattice into a tetragonal phase, which has a volume 6% larger than the former,⁽⁵⁵⁾ so gigantic stresses between these phases will damage the structure. Analogues to LiMnO₂, LiNiO₂ undergoes phase transitions from H2 to H3 phases when the occupancy of lithium is over 0.75. This dramatic structural shift will break down electrode particles and cause them to lose electrochemical contact. The higher the charge, the more cracks are generated.

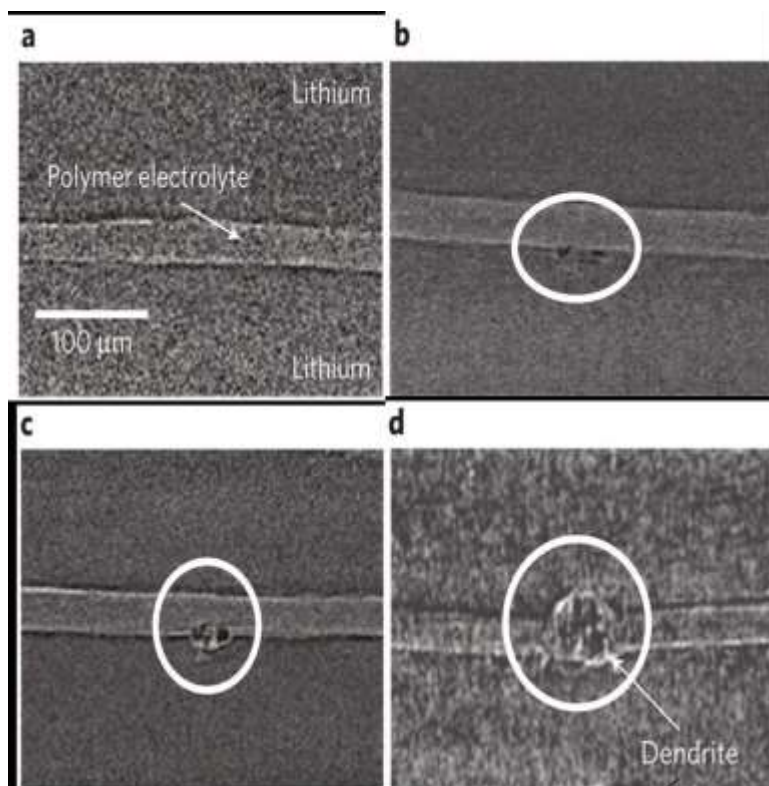


Figure 1.4 Cross-section images of dendrite growth. The current density increases from a (0 C/cm^2), b (9 C/cm^2), c (84 C/cm^2) to d (296 C/cm^2). Copyright with permission Katherine J. Harry, Daniel T. Hallinan, Dilworth Y. Parkinson, Alastair A. MacDowell, Nitash P. Balsara, *Nat. Mater.*, 13 (1), 69 (2014).

In addition to the positive side, volume expansion by anode materials can cause more severe capacity loss. In terms of silicon, the volume of lithiated silicon became 280% larger than its original size and this huge expansion/contraction process can easily fracture the particles, resulting in disintegration between active materials and unavoidable capacity loss. Apart from volume expansion, lithium metal plating is another catastrophic problem. Usually, lithium plating is very unlikely at low C-rates because the deposition potential is below 0 V vs Li/Li^+ , so lithium intercalation becomes more favorable above 0 V . However, when cells are cycled at high-rates, polarization becomes high and the overpotential, η , may drive lithium ions to plate on the anode surface,⁽⁵⁶⁾ as shown in Figure 1.4. The morphology of lithium plating can vary from heterogeneous spikes to a homogeneous film and its growing locations can be on the defects or the edges of the active materials depending on actual conditions. Unwanted lithium plating is

like cancer for cell life. It will not only react with electrolyte to consume lithium ions continuously, but it will possibly pierce through separators, then cause overheating or short circuit. Therefore, studies dedicated to monitoring and eliminating lithium metal plating are being conducted vigorously.

Interestingly, recent work showed that some other components, which were presumably “stable” before, are now considered reactive and may contribute to part of capacity loss. Yan(57) used a new type of symmetric two lithium half cells termed as “double half cells” to precisely measure reactivity of copper current collector. He illustrated that copper can actively be involved in irreversible reactions with electrolyte leading capacity loss. In addition, the reactivity can be enhanced by higher temperatures and electrolyte additives such as VC. Although real copper collectors are more inert with less surface area compared to the extreme case in Yan’s work, this result alerted researchers that roles of inactive components should be also rigorously examined.

1.6.3 Age predictions for LIB

The aging of LIB cells is a complicated phenomenon that incorporates thermodynamic processes, organic reactions, structure analysis, etc. It is very difficult to identify a single factor and track every process during cycling, so building a comprehensive model for an accurate prediction of cell’s aging process is highly desired. The most popular model is Safari’s(58) physical model that combines both quantifiable physical properties related to oxidation/reduction and diffusion process in the electrolyte. The physical model is adversely applied because it introduced a great method for not only adding macro physical parameters but explicitly demonstrating their individual impact on the overall magnitude of cell degradation. Regardless of its early success, the physical model is inadequate for molecular changes by only considering macro physical properties. As discussed in 1.6.1, parasitic reactions will yield plenty of complex organic radicals and these radicals are the triggers for a majority of electrolyte failures. Therefore, many theoretical chemists used computational tools including Monto Carlo simulation and density functional theory (DFT)(58) to obtain a better interpretation of irreversible cell reactions, phase transitions and their relationship to cell fade. However, the unity between micro simulations and macro observations is a challenging task for the completion of LIB aging models.

1.7 Sodium ion batteries (SIB)

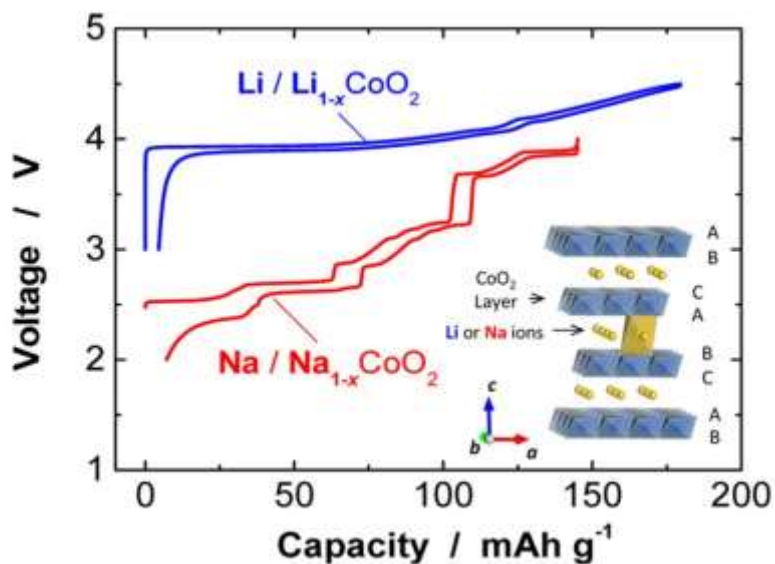


Figure 1.5 Comparison of charge/discharge curves of Li/LiCoO₂ and Na/NaCoO₂ cells. Copyright with permission from Naoaki Yabuuchi, Kei Kubota, Mouad Dahbi, Shinichi Komaba, *Chem. Rev.*, 114(23), 11639(2014)

The popularity of LIBs has exponentially increased the consumption of lithium. Because it is a rare element, it is clearly insufficient for gigantic growth in Li-ion cell manufacture in the future. Sodium is an excellent substitution for lithium due to its similar alkali metal properties and high abundance. Historically, studies on SIB and LIB both started in the 1980s, with the same “rocking chair” battery structure including a layered metal oxide cathode, host anode and electrolyte. However, SIBs have lower energy density than LIBs. As is common knowledge, sodium has a larger atomic radius (1.02 vs 0.76 Å) and a higher reduction potential (3.04 vs 2.71 V) than lithium, so SIBs will have a lower volumetric capacity than a corresponding LIB, as shown in Figure 1.5.

1.7.1 Electrodes for SIB

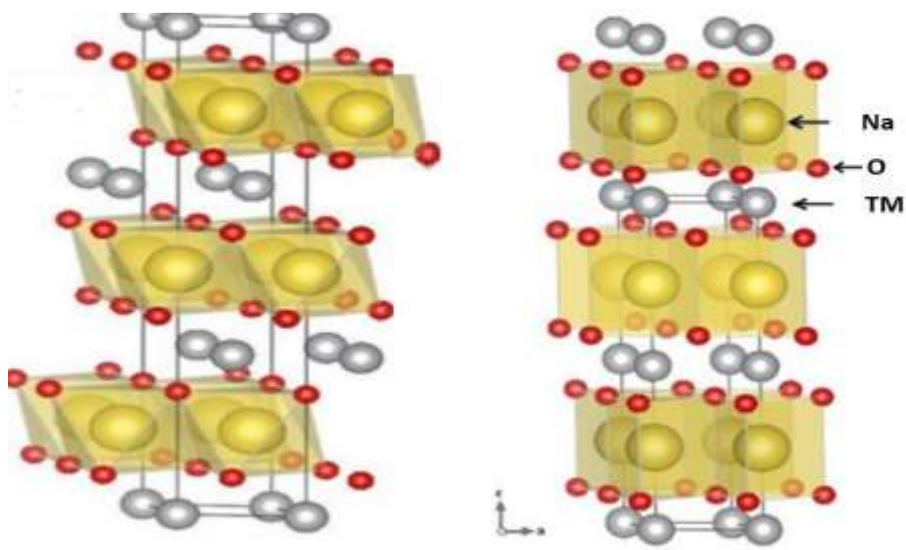


Figure 1.6 a) O3 and b) P2 structure of sodium transition metal oxide cathode materials.

Copyright with permission from S. Guo, P. Liu, H. Yu, Y. Zhu, M. Chen, M. Ishida, H. Zhou, *Angew. Chem.*, 54 (20) , 5894 (2015).

Many options for positive electrodes in SIBs were derived from LIBs, based on similar structures. Layered metal oxides (Na_xMO_2) with P2 or O3 structures are the most commonly studied due to their high energy density and simple synthesis. The capital letters refer to the location of metal ions such as prismatic (P) and octahedral (O), and the number indicates the number of repeating layers, as shown in Figure 1.6.

Besides the similarities between lithium and sodium, some differences were also discovered. Regarding structure, unlike almost the exclusive octahedral sites formed by lithium, sodium sites have more flexibility between prismatic and octahedral sites. Although both types of cathodes can achieve good cycling performance, cathodes with P2-type structures generally have better rate capabilities than O-type cathodes because of faster Li^+ diffusion. However, phase transitions are a huge drawback in some of P2-type Na_xMO_2 materials. It was reported that oxygen will no longer maintain its original structure but shift to tetrahedral sites after the removal of sodium from P2 sites. As a result, huge polarization can be exhibited. Regarding the chemical stability, most of sodium cathode materials are air sensitive. They will spontaneously react with

water or air to form complex compounds, so the cost of its storage is significantly higher than normal lithium cathodes. Regarding intercalation behavior, some amazing facts were found in the sodium case. LiCrO_2 is known to be inactive, whereas NaCrO_2 is electrochemically active. One of reasons is that smaller lithium ions have a strong tendency to mix with Cr layers, while larger sodium ions are comparatively unwilling to mix to prevent phase transitions.

Currently, the biggest obstacle for current SIBs is finding appropriate materials for the host anode. In contrast to the amazing compatibility between lithium and graphite, sodium cannot intercalate into graphite except for trivial insertion in diglyme-based electrolytes.(60) On the other hand, hard carbon is surprisingly accessible for sodium intercalation and delivers above 300mAh/g reversible capacity.(61) Many studies and models(62) attempted to explain the mechanism of massive sodium insertion into hard carbons, but only the “micropore” model is broadly accepted.(63) This model divides sodium intercalation into two stages. In the first stage, sodium ions intercalate between wider carbon layers, and in the second stage, they intercalate into the micropores. These two stages correspond to the sloped region above 0.2 V (vs Na/Na^+) and the plateau close to the equilibrium Na potential. Komba(64) specifically explained the difference in intercalation between Lithium and sodium at the second stage. The isolated sodiums will form quasi-metallic cluster structure inside micropores with a very low entropy, so hard carbon is able to accommodate substantial amount of sodium ions in the second stage and a huge reversible capacity will be obtained.

Transition metal oxides (TMO) are an interesting choice for anodes in SIB. TMO is not a typical host for anodes in LIB because of its high intercalation voltage, while sodium has a lower intercalating voltage, so the overall energy density will be actually increased. For instance, $\text{Na}_2\text{Ti}_3\text{O}_7$ studied by Fielden,(65) which has a potential between 1.0 – 1.6 V vs. Li, has been shown to reversibly intercalate Na at only 0.3 V with a decent capacity of 178 mAh/g. But tremendous amount of conductive carbon is required to maintain good cycling for this material. This can be improved by mixing the Ti in $\text{Na}_2\text{Ti}_3\text{O}_7$ with other transition metals to make the titanium more conductive. Fielden(66) synthesised $\text{Na}_x\text{Ni}_{x/2}\text{Ti}_{1-x/2}\text{O}_2$ by solid state reactions. Its intercalation voltage was lower than TMO with pure titanium and delivered a good reversible capacity of 100

mAh/g with minimal hysteresis. He furthered investigated other first-row transition metals such as Cr or Mn. Although cycling performance of those materials are acceptable, it is hard to compromise between capacity and structural stability in these materials. Essentially for these TMO compounds, sodium intercalated and occupied the vacancies, therefore, the capacity of TMO is directly associated with the amount of vacancies. The more vacancies (a lower number for x in Na_xMO_2) there are, the higher capacity it will achieve. However, more vacancies (x is less than 0.4) will possibly wreck the stable P2 structure and an irreversible phase transition will start to take place. This limitation hindered applications of TMO as a sodium anode and more comprehensive studies on vacancy mechanism are absolutely needed.

CHAPTER 2 EXPERIMENTAL TECHNIQUES

2.1 X-ray Diffraction (XRD)

2.1.1 X-ray theory

X-rays are electromagnetic radiations, whose wavelength is in the range of 0.01 ~ 10 nanometers, corresponding to frequencies between 3×10^{16} to 3×10^{19} Hz and energies from 100 eV to 1 MeV. High energy X-rays have extensive applications in drug detection, medical imaging, and analytical chemistry. Another important application is X-ray diffraction (XRD). This technique is used to determine crystal structures and obtain other information about materials by investigating diffracted X-ray beams. Diffracted X-ray angles and intensities are directly associated with overall crystal structures, chemical composition, physical properties of solids, etc.

In an XRD experiment, X-rays are generated from the collision between metal anode (copper is the most common one) and high energy electron beams.(67) Typically, electrons are emitted from a heated tungsten filament. These electrons obtain sufficient kinetic energy from being accelerated by a high potential to collide with a metal anode and knock out electrons from the inner shell of the metal. Meanwhile, other electrons in higher energy levels will fall to lower levels and release X-rays with various wavelengths. The highest intensity X-ray radiation comes from electron transitions to K orbitals, identified as K_{α} , K_{β} , and K_{γ} , in the order of decreasing wavelength. Sequentially, K_{β} and K_{γ} radiation can be selectively rejected by a monochromator, but two emissions, $K_{\alpha 1}$ and $K_{\alpha 2}$, are allowed to pass to the detector. $K_{\alpha 1}$ is a stronger emission than $K_{\alpha 2}$, yet both have nearly identical wavelengths ($K_{\alpha 1}$ 0.154056 nm, $K_{\alpha 2}$ 0.154439nm),(68) so both of these X-rays are retained for XRD measurements.

2.1.2 Bragg's law and the Scherrer equation

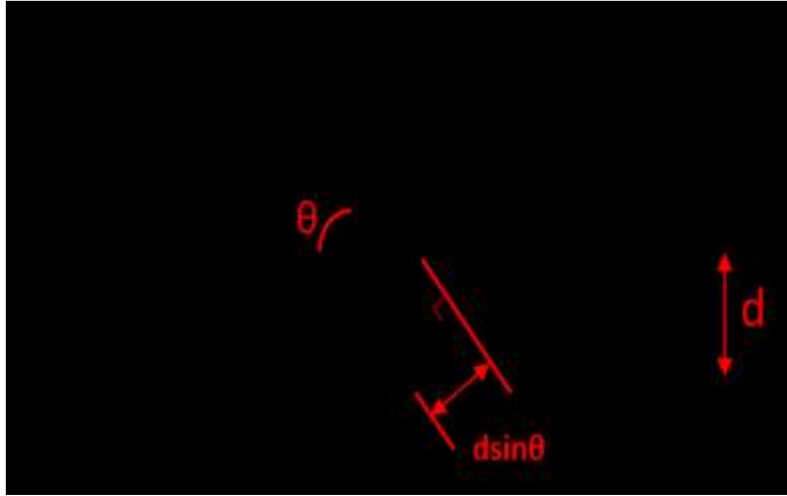


Figure 2.1 Illustration of the Bragg's law of diffraction

Incident X-rays should have a wavelength comparable to the lattice plane spacings of a target sample. As shown in Figure 2.1, when two X-ray beams are incident upon a crystal, they diffract along different path lengths. In this diagram, the lower beam travels along a longer path than the higher beam. If the extra path length equals an integer number of wavelengths, constructive interference will be obtained. The relationship can be summarized as Bragg's law.

$$n\lambda = 2d \sin \theta \quad (2.1)$$

Where n is an integer, λ is the incident X-ray wavelength, d lattice spacing distance, and θ is the angle between incident beam and crystal planes. Therefore, planes with specific orientations that match the Bragg condition will exhibit characteristic peaks in the XRD patterns, from which unknown samples can be identified and crystal structures can be elucidated.

The average grain size, τ , of crystalline phases can be estimated by the Scherrer equation:

$$\tau = \frac{k\lambda}{H \cos \theta} \quad (2.2)$$

Here, K is a dimensionless shape factor with a common value of 0.9, λ is the X-ray wavelength, H is the full width at half maximum (FWHM) of a XRD peak (in radians), and θ is the angle between the incident X-rays and the lattice planes. According to the Scherrer equation, the

broadening of peaks is related to reduction in grain size. Highly ordered crystals show sharp XRD peaks, as opposed to broad peaks from small amorphous grains.

2.1.3 XRD sample preparation

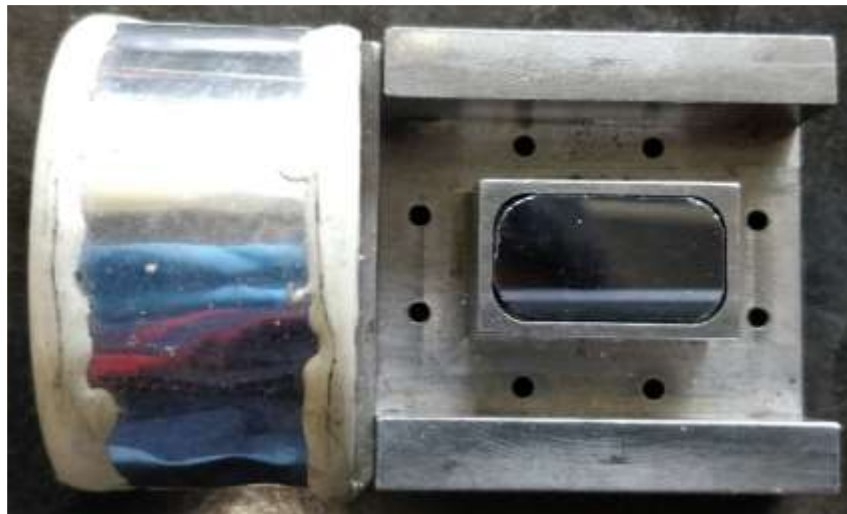


Figure 2.2 The gas tight XRD holder for air-sensitive samples with a zero-background silicon wafer

In this thesis, XRD patterns of all samples were measured with a Rigaku Ultima IV diffractometer equipped with a copper target X-ray tube, a scintillation counter detector with a diffracted beam monochromator and a D/TeX Ultra linear detector with K_{β} filter. The X-ray generator accelerating voltage was 45 kV and the filament current was set at 40 mA.

For XRD sample preparation, the air sensitivity of samples should be taken into account. Powder samples that are not air-sensitive were placed in a stainless steel sample holder with an open well. However, for air sensitive samples, a special designed gas-tight holder (DPM Solutions, Hebbville NS) was used, as shown in Figure 2.2. The gas-tight holder has an aluminized Mylar™ window and silicon crystal substrate, both of which have zero background and no impact on XRD patterns. Air-sensitive samples were placed on the silicon crystal surface and loaded in an Ar-filled glove box to avoid air exposure.⁽⁶⁹⁾ All XRD measurements were conducted at a scattering angle (2θ) range of 20° to 80° degrees with a step size of 0.05° and a 3 second dwell time at each step.

2.2 Electron microprobe measurements

Scanning electron microscopy (SEM) is a technique used for investigating surface topography and elemental composition. The resolution of SEM images can reach nm level and SEMs can operate at magnifications that are easily adjusted from about $10\times \sim 300,000\times$.⁽⁷⁰⁾

During SEM operation, electrons emitted from an electron gun travel through one or two condenser lenses, accelerated by an electromagnetic field. Another electromagnetic field rasters the electron beam over the specimen surface, where interactions occur that either absorb or scatter electrons, causing the emission of secondary electrons, back scattered electrons and X-rays. Specifically, secondary electrons resulting from inelastic collisions can be extraordinarily helpful to give a well defined, three-dimensional surface images, while back scattered electrons can be used to image electron density variations. Therefore, all these signals can provide a comprehensive analysis of material surfaces.

In this study, changes in particle size and surface morphology were studied using SEM images of sample cross sections before and after cycling. After cycling tests, cells were disassembled, and working electrodes were washed with DMC thoroughly to remove remaining electrolyte. Ion beam polished cross sections were obtained with a JEOL IB-09010CP cross section polisher. Cross section imaging was performed with a TESCAN MIRA 3 LMU Variable Pressure Schottky Field Emission Scanning Electron Microscope.

2.3 Fourier-transform infrared spectroscopy

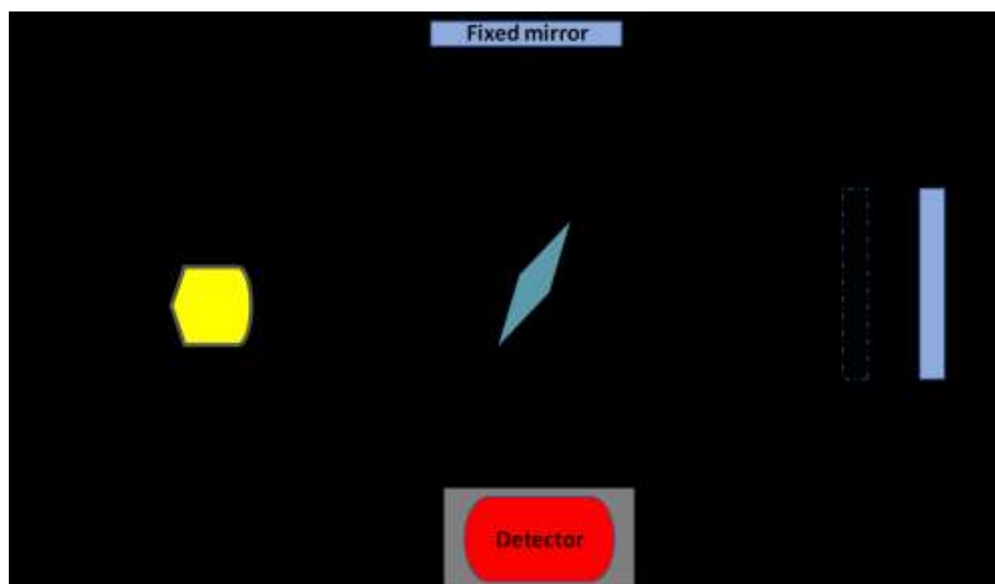


Figure 2.3 Block diagram of an FTIR instrument

Fourier-transform infrared spectroscopy (FTIR) is a technique used to obtain infrared spectra of gas, liquid or solid samples. Due to molecular vibrations, homonuclear diatomic molecules will absorb infrared beams in certain wavelengths and internal information regarding molecular bonding and functional groups can be obtained from FTIR spectra. For example, the carbon-carbon triple bond has a signature absorption peak near 2120 cm^{-1} , which is an important indicator for the existence this triple bond.(71)

The simplest interferometer is the Michelson interferometer.(71) It includes a light source, detector, beam splitter and two perpendicular mirrors, as shown in Figure 2.3. Infrared light converges at the beam splitter, interacts the sample and then is collected by the detector. One moving mirror and one stationary mirror create different optical paths. When the distance between the beam splitter and the moving mirror is the same as that between the beam splitter and the stationary mirror, the interference will be constructive, and the maximum intensity will be obtained. When the moveable mirror moves to other positions, the intensity will change accordingly. As the mirror oscillates, data is collected by the detector (intensity vs. time) then processed into a spectrum (intensity vs. wavenumber) by applying a Fourier transformation.(72)

In this thesis, FTIR spectra were collected using a Bruker Alpha FTIR equipped with a standard quartz liquid sample holder. The sample holder was loaded with liquid samples in an Ar-filled glove box and sealed with a cap, so that FTIR measurements could be conducted without sample air exposure. The volume of sample in the holder was 3.8 mL. The scanning range of the FTIR spectra were 3000 cm⁻¹ to 500 cm⁻¹. Thirteen scans were conducted for each background and sample measurement and the spectra were analyzed using Omnic™ software.

2.4 Electrochemical techniques

2.4.1 Introduction

During LIB cell operation, the negative electrode is where oxidation reactions occur and the positive electrode is where reduction occurs during discharge. The potential of LIB cells is defined according to Equation 2.3.

$$V = \frac{-(\mu_{positive} - \mu_{negative})}{ne} \quad (2.3)$$

Where V is the cell potential measured in volts, $\mu_{positive}$ and $\mu_{negative}$ are the chemical potentials of positive and negative electrodes, respectively, n is the number of active electrons per ion (n = 1 for lithium or sodium), and e is the charge of an electron. In half cells, working electrode potentials are measured against a lithium or sodium metal foil reference/counter electrode. In full cells, the cell potential can be measured, but individual electrode potentials cannot be separately determined.

Capacity (Q) is defined as the total amount of electrical charge participating in electrochemical reactions. Active material theoretical capacity can be calculated as:(73)

$$Q \left(\frac{mAh}{g} \right) = \left[\frac{(F * n_{Li/Na})}{MW} * 3600 \right] * 1000 \quad (2.4)$$

Where F is Faraday's constant (96500 coulombs per gm equivalent), $n_{Li/Na}$ is the number of Li/Na per formula unit of the electrode material, and MW is the molecular mass of the electrode material.

Gravimetric capacity is typically expressed in units of mAh/g. Volumetric capacity is more appropriate for assessing anode materials for use in most practical applications, and the unit is mAh/L. The theoretical capacity is the maximum number of lithium that can react electrochemically with an active material, but the real capacity is typically lower than the theoretical number due to the restriction of limited cutoff potentials and electrochemical stability. The term "C-rate" refers to the current required to complete one complete charge or discharge in one hour, so the testing current is the product of the reversible capacity and the amount of active materials multiplied by the C-rate factor (1 in 1C).

2.4.2 Electrode fabrication

Electrodes in this study consisted of active materials (silicon alloy, NMC, CoO, etc.), carbon black (CB, Super C65, Imerys Graphite and Carbon) and a binder in certain weight ratios. These components were thoroughly mixed in solvents with three tungsten carbide balls in a Retsch PM200 rotary mill (100 rpm, 30 minutes) under argon or air atmosphere to create a uniform slurry. The slurry was then coated onto copper or aluminum foil (Furukawa Electric, Japan) and dried at 120 °C overnight under argon. Following the drying process, some electrodes were cured by heating at higher temperatures.⁽⁷⁴⁾ Circular electrodes were punched from the resulting coatings for cell assembly. This thesis involves different types of active materials tested in different kinds of cells. Therefore, exact details regarding electrode and cell preparation are elaborated in the following chapters.

2.4.3 Conflat cell fabrication and characterization

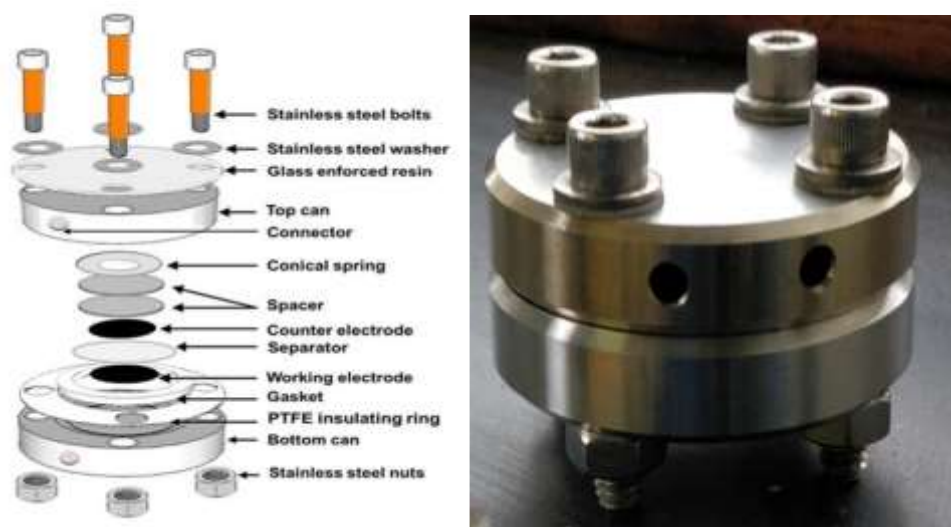
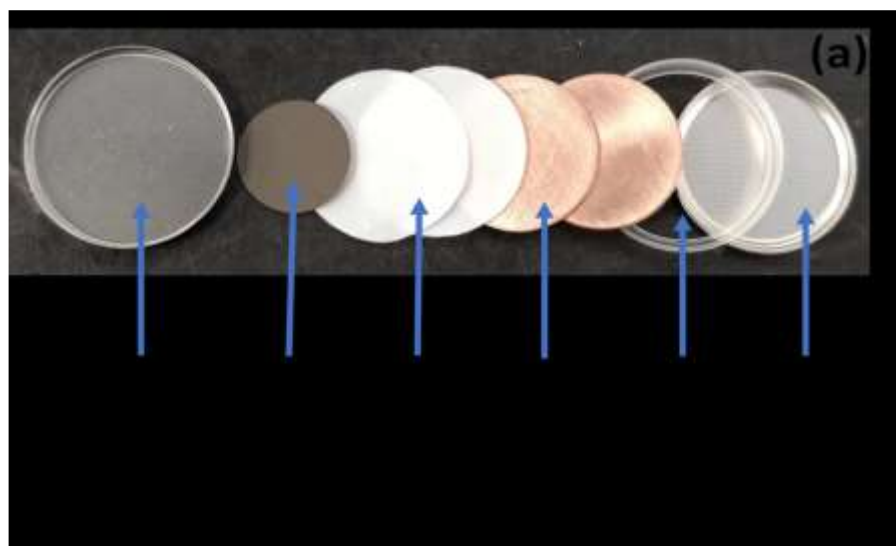


Figure 2.4 The two electrode conflat cell model and actual image

In this thesis, cells operating at high temperatures were required, so conflat cells, shown in Figure 2.4, were used. Unlike Swagelok cells sealed by PTFE ferrules, (75) conflat cells are sealed by means of knife edges that impinge on plastic gasket as the bolts are tightened. A PTFE insulating ring is used as a spacer, so that the top and bottom can are always separated by the same distance. Such cells can be operated under high vacuum or at temperatures as high as 200°C, making them suitable for thermoelectrochemical activation studies.

2.4.4 Coin cell fabrication



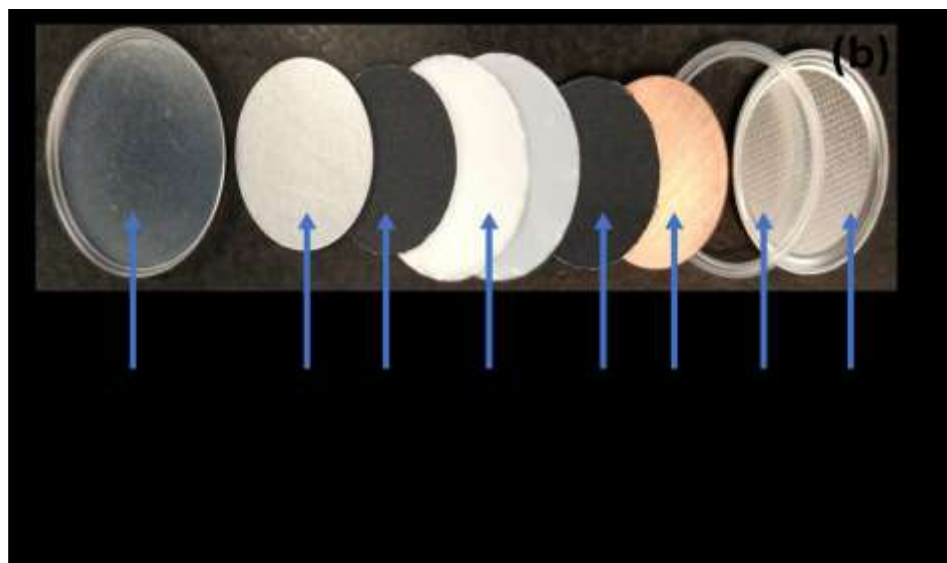


Figure 2.5 Components of half coin cells (a) and full coin cells (b)

Coin half cells are commonly used for testing battery materials.⁽⁷⁶⁾ In this thesis, coin half cells (2325 type) were assembled in an Ar-glove box, each with a working electrode, lithium metal counter electrode, two Celgard 2300 separators and about 100 μL of electrolyte, as shown in Figure 2.5. Li disks were punched from a thick Li foil (99.9%, Sigma Aldrich). A polyethylene gasket acted as an insulator between the top and bottom casings to prevent cell shorting.

Coin full cells are commonly used for testing overall battery performance and understanding the interactions between positive and negative electrodes. The components for full coin cells are similar to half coin cells, except the lithium metal is replaced with a cathode. One major hurdle of assembling full cells is to perfectly align both electrodes. It was reported that electrode misalignment can cause great variation in cell performance.⁽⁷⁷⁾ However, reliable methods to make full Li-ion coin cells are rarely discussed in the literature.⁽⁷⁸⁾ Here in this thesis, a newly designed aligner is used to align the electrodes in full cells.

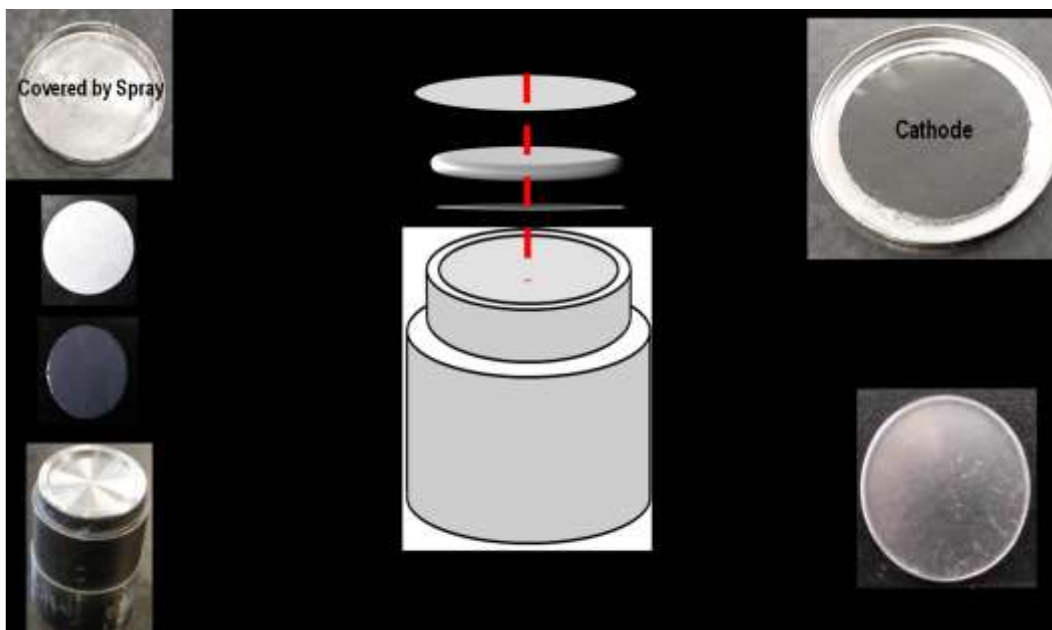


Figure 2.6 A flow chart showing full coin cell assembly with an aligner

The flow chart in Figure 2.6 demonstrates the assembly process of full coin cells with an aligner. During cell preparation, both cathode and anode were punched into a circular shape with an equal size as the copper spacer. The aligner has two concentric circles. The inner and outer circle have the same diameter as the cell spacer and the bottom can, respectively. The electrodes are fixed on the center of the bottom can by placing them into the inner circle and applying a thin layer of 3M spray adhesive, and then placing the cell can on top of the aligner. Since vacuum heating is needed for silicon alloy electrodes, positive electrodes were pre-fixed onto the can, as describe above, while the rest of the cell components were assembled in an Ar-filled glove box.

2.4.5 Electrochemical characterization

Both half and full cells were tested at 30.0 ± 0.1 °C using a Neware battery testing system at 0.1C for the first cycle and 0.2C for subsequent cycles in a potential range of 5 mV - 0.9 V for half cells and 2.8 V – 4.4 V for full cells. Here C-rate is defined as the current required to fully lithiate the 3M V6 Si alloy/SFG6L graphite electrode based on a theoretical capacity of 950 mAh/g and 360 mAh/g for V6 and SFG6L, respectively.

2.5 The gas bubbler

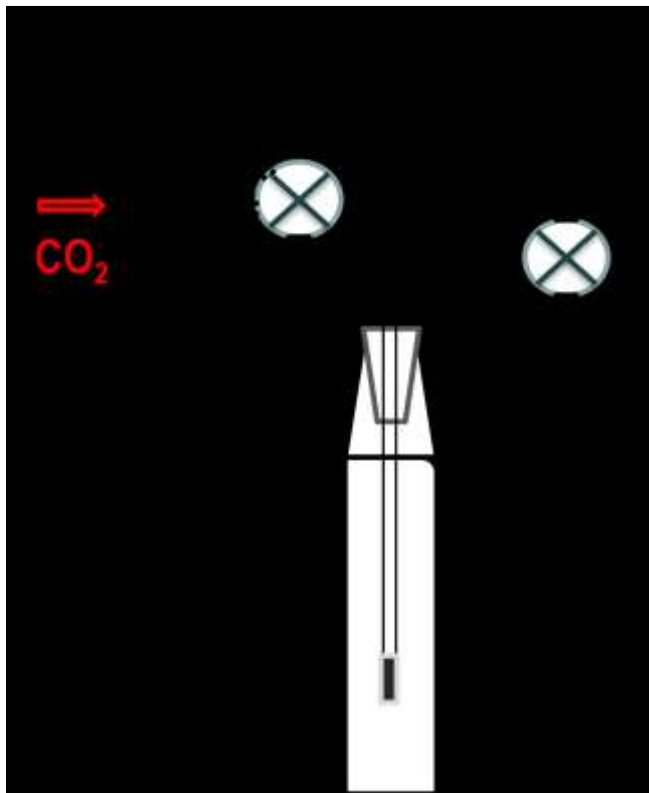


Figure 2.7 Sketch of the CO₂ bubbler device: a₁ is a three-way valve, a₂ is a two-way valve and b₁ is the bubbler. The dashed rectangles indicate where the handle will turn during the measurement.

Various methods and apparatuses⁽⁷⁹⁾⁽⁸⁰⁾ have been established to introduce gas into liquid solvents and electrolyte solutions. Good mixing is key to efficient gas dissolution. In order to incorporate CO₂ into electrolytes, a gas bubbler device was built as in Figure 2.7. It consists of a quartz bubbler, a three-way valve (a₁) and a two-way valve (a₂). A tube in the three-way valve serves as the gas inlet and the top tube is opened to the atmosphere for pre-air evacuation. This device worked well for dissolving CO₂ into electrolytes.⁽⁸¹⁾

To dissolve CO₂ into liquids, the left and top gate of a₁ valve are open and the rest of the device is closed. CO₂ gas is flowed through the inlet line and allowed to escape into the open air through the 3-way valve, in order to flush air from the system. Then, the 3-way valve is positioned to allow CO₂ to bubble into the electrolyte, while valve a₂ is opened to allow CO₂ to

flow out of the device via an oil-filled bubbler. Finally, after CO₂ bubbling, both a1 and a2 are closed to enable transfer of the electrolyte back into the glove box for further characterizations.

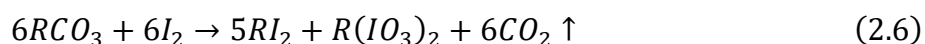
2.6 Karl Ficsher titration

Karl Ficsher titration (KFT) is a common analytical method to measure the water content of samples. The water determination is based on the reaction described by Bunsen.¹⁶



The main component of a typical Karl Ficsher titrator is the anode solution, comprising an alcohol, a base, SO₂ and I₂. There are two different techniques to introduce iodine into the system. The titration process is controlled by the small polarization current and the potential change between two Pt electrodes in both volumetric and coulometric KFT. In the early stage of titration, water reacts with iodine as soon as they come in contact, so no free iodine exists. The external circuit needs to maintain constant current by applying a high potential. Upon approaching the equivalence point, excessive free iodine causes ionic conduction and the applied potential will significantly reduce to maintain the same current. Therefore, this potential drop is the indication of the end point of the titration.

In this thesis, a METTLER TOLEDO C30 coulometric KFT was used for Karl Fischer measurements. The method used for the liquid sample is Coulometric direct titration C120 as in reference 82(82). Procedures of C120 include sample injection, 300s of steady mixing time, titration, calculation and record. The voltage limit is set to 100mV as the ending point of the titration and the constant current between electrodes is 200mA. A high stirring rate (250 rpm) and enough mixing time provide a homogeneous system during the titration to ensure the accuracy of results. Furthermore, organic carbonate solutions are the majority of samples for KFT in this thesis, so background measurement and picking the first end point are required to alleviate the impact from the reaction between carbonates and iodine.¹⁷ The reaction can be expressed as below.



Thus, three blank samples are used to measure the background and the final result in KFT is the result of the first end point minus the background.

CHAPTER 3 THERMOACTIVATION OF COBALT OXIDE IN SIB

3.1 Introduction

As mentioned in chapter 1, the lack of practical high energy density negative electrode materials limits SIB development. Binary transitional metal oxides such as Fe_2O_3 , Fe_3O_4 , Co_3O_4 , Mn_3O_4 , CuO , and NiO have been shown to have significant capacity with sodium. (83–85) Given that the standard molar Gibbs formation energy of Na_2O is larger than Li_2O , conversion reactions with oxides have a lower theoretical potential vs. Na, making them desirable for anode materials for SIB.

3.1.1 The conversion reactions

Binary transition metal oxides have been reported to have large reversible capacity with lithium via conversion reactions, compared to materials that undergo intercalation mechanisms. (86) In conversion reactions, alkali metal ions will replace transition metal in transition metal oxide converting it into lithium or sodium oxide and pure transition metal. The overall mechanism is expressed as the equation below.



The performance of conversion reaction materials relies on the complete reduction from positive state to neutral state of transition metals, thereby accessing all possible oxidation states. Therefore, disruption and reorganization of structures will presumably take place through the entire reactions. Thorp described the conversion stages of FeF_3 by analysing STM (scanning tunneling microscope) surface patterns and concluded that the conversion reaction started from the uncoordinated edges or defects sites where bonding energy is significantly lower than highly ordered sites. (87) It was also found that further reaction will preferentially occur on those nucleated sites before lithium ions diffuse inside the solid structure. This reaction mechanism results in kinetic limitations deemed as the major rate determining step in conversion reactions. The contoured length of the lithium or sodium ion diffusion path into the binary oxide and electrolyte wettability of the electrode material further contribute to kinetic limitations.

The key to optimize the performance of conversion reactions is to overcome kinetic barriers and enhance the conductivity between electrolyte and active materials. Improvement of

conversion reaction kinetics has been achieved by, for example, particle size minimization, use of conductive coatings, and porosity optimization.(88) Reducing particle size to the nanoscale has proven to be successful for accessing the majority of the theoretical capacity of some binary materials, such as FeF_3 and CoP , however this increase in interfacial area leads to more electrolyte decomposition.(89) In the case of binary oxides, metal nanoparticles as well as side reaction products like LiOH , LiH that are formed during lithiation or sodiation conversions catalyze electrolyte decomposition, creating extra capacity upon discharge.(90,91) This process is typically characterized by a sloping region in the voltage curve below 0.8 V vs. lithium metal.(90,91) The exact nature of this reversible SEI is not well known, although it has been evidenced that ethylene oxide oligomers and lithium methyl carbonate can be formed on materials undergoing conversion reactions.(92) This SEI is also consumed during delithiation or desodiation and can reach reversible capacities as high as 150 mAh/g.(90) This mechanism can result in an initial increase in reversible capacity, but eventually, due to its electrolyte consuming nature, leads to capacity fade.(90,93)

Higher temperature electrochemistry might be able to overcome kinetic limitations. There are recent examples of activating materials through high temperature lithiation/delithiation of alloys and transition metal oxides such that they can reversibly cycle at room temperature.(94,96) This phenomenon has been termed as thermoelectrochemical activation.(96) In the case of alloys, high temperature cycling can create new phases that are electrochemically active with lithium.(94) For oxides, high temperature lithiation has been observed to reduce particle size of the conversion reaction products such that the activation barrier is low enough for the reaction to proceed reversibly at room temperature.(95) Attempts of these thermoelectrochemical procedures have not been reported for sodium-ion electrode materials.

3.1.2 The goal of this work

Among all binary metal oxides, CoO has shown decent capacity retention and voltage output over 30 cycles. Badway et al. assembled a CoO vs. LiCoO_2 full cell with a specific energy of 120 Wh/kg, quite comparable to graphite cells (180 Wh/kg).(97) Interestingly, CoO , has been reported to have negligible electrochemical activity with sodium.(95) Therefore, the conversion

reaction of sodium with CoO must be kinetically limited. In this chapter, thermoelectrochemical activation, particle size reduction, and the combination of both methods were studied for achieving electrochemical activity of CoO with sodium.

3.2 Experimental

3.2.1 Electrode preparation

Electrodes consisted of crystalline CoO (cr-CoO, 95%, Sigma-Aldrich Alfa Aesar) or TiN (99.7% Alfa Aesar), carbon black (CB, Super C, Timcal) and polyimide (PI, HD MicroSystems PI 2555) binder in an 80:12:8 weight ratio. These components were thoroughly mixed in N-methyl-2-pyrrolidone (Sigma Aldrich, anhydrous 99.5%) with three tungsten carbide balls in a Retsch PM200 rotary mill (100 rpm, 60 minutes) under argon atmosphere to create a uniform slurry. The slurry was then coated onto copper foil and dried at 120 °C overnight under argon. Following the drying process, electrodes were cured at 300°C under argon for two hours in order to cure the polyimide binder.⁽⁹⁸⁾

Circular electrodes, 2 cm² in area, were punched from the resulting coatings for cell assembly. Electrodes were also prepared by ball milling the cr-CoO with carbon black in an 8:1 mass ratio (total sample size ~3 g) in 64 mL hardened steel ball-mill vials with five 0.5" stainless steel balls for 2 hours using a Spex mixer-mill (SPEX CertiPrep). This resulted in a ball milled CoO / carbon black composite, referred to here as bm-(CoO/CB). Electrodes comprising bm-(CoO/CB)/PI in the 80:10:10 mass ratio were prepared in the same method as described above.

3.2.2 Conflat cell assembly

In this CoO work, Na/CoO conflat half cells were assembled as mentioned in chapter 2. Na foil disk anodes were punched from foil 0.015" (0.38 mm) thick that was rolled from Na ingots (Sigma Aldrich, ACS reagent grade). The electrolyte used was NaPF₆ (Sigma Aldrich 98%) dissolved in 50:50 EC: DEC by volume, with 10% by FEC (all from BASF). Two Celgard 2300 membranes and one blown microfiber disk (BMF, 3M Company) were used as separators.

3.2.3 Electrochemical characterization

Cells were tested with a Maccor Series 4000 Automated Test System (Maccor Inc., Tulsa, Oklahoma). Cells were cycled at 30°C and 60°C constant rates of 0.1C with a trickle discharge to 0.05C, where C-rates were calculated from the theoretical specific capacity CoO (715 mAh/g). CoO electrodes were also sodiated in cells at 60°C, removed under inert atmosphere and placed in a cell with fresh electrolyte and a fresh sodium metal electrode, and then cycled at 30°C. In addition, the rate capability was tested at 0.1C, 0.2C, 0.5C and 1C for 10 cycles each.

3.3 Results and discussion

3.3.1 CB/PI Electrochemistry

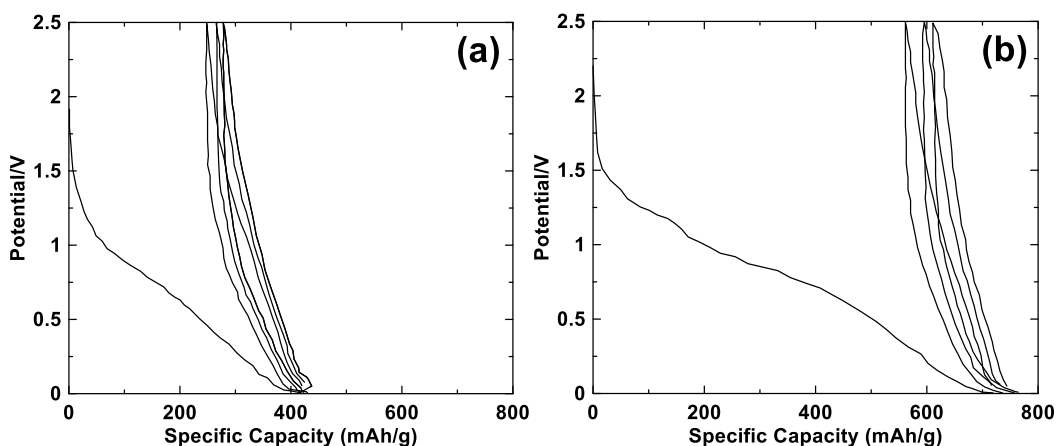


Figure 3.1 Potential vs capacity curve of the first three cycles of TiN/CB/PI electrodes in sodium half cells (a) at 30°C and (b) 60°C.

It has been shown previously by the Obrovac group that TiN can be used as a chemically inert conductive diluent in electrodes, so that the electrochemistry of non-active electrode components can be effectively characterized.⁽⁹⁹⁾ In this study, a TiN/CB/PI 80:12:8 by mass electrode coating was used to characterize the capacity contribution from CB and PI in Na cells. Figure 3.1 shows potential vs capacity curves of this electrode at 30°C and 60°C. The first sodiation capacity of CB/PI increases from 420 mAh/g at 30°C to 720 mAh/g at 60°C. These capacities correspond to 105 mAh/g and 180 mAh/g, respectively, when calculated with respect to the active weight of the 80:12:8 by weight active/CB/PI coating. However, upon subsequent desodiation/sodiation the reversible capacity of the electrode is about 175 mAh/g and does not

change significantly in this temperature range. This reversible capacity corresponds to 44 mAh/g when calculated with respect to the active weight of 80:12:8 by weight active/CB/PI coating. Overall, the CB and PI contribute significantly to irreversible capacity and a small amount to reversible capacity for the CoO electrodes of 80:12:8 composition in sodium cells. The potential profiles of the electrodes also exhibit larger capacity slippage at 60°C than 30°C, indicating severe decomposition of electrolyte during cycling under high temperatures.

3.3.2 CoO Electrochemistry

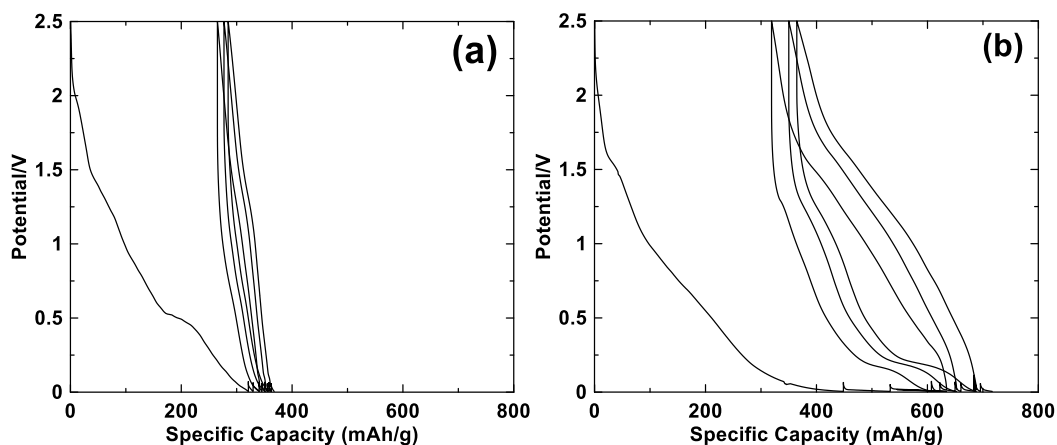


Figure 3.2 Potential vs capacity curves of the first three cycles of cr-CoO/CB/PI electrodes in sodium half cells (a) at 30°C and (b) 60°C.

The first three cycles of the potential vs capacity curves of cr-CoO cycled at 30°C are shown in Figure 3.2 (a). The cr-CoO electrode has a first sodiation capacity of 343 mAh/g and the reversible capacity is 80 mAh/g. This corresponds to a 238 mAh/g first sodiation capacity and a 36 mAh/g reversible capacity for cr-CoO after the CB and PI capacity contributions are subtracted. Therefore, the cr-CoO contributes to the electrode's irreversible capacity but is essentially inactive. This inactivity agrees with previous reports.⁽¹⁰⁰⁾ The slippage is small at 30°C, and is comparable to that of the TiN/CB/PI electrode. Therefore, the amount of electrolyte decomposition on cr-CoO during cycling at 30°C must be small. Figure 3.2(b) shows the potential profile of the first three cycles of cr-CoO cycled at 60°C. The first sodiation and reversible capacities of this electrode have increased significantly at 60°C. At this temperature, the first sodiation capacity and desodiation capacity is 631 mAh/g and 336 mAh/g for cr-CoO, respectively,

after the CB and PI capacity contributions are subtracted. The electrode slippage rate has also increased significantly. This indicates that although the cr-CoO electrode has become active at 60°C, electrolyte decomposition during the first and subsequent cycles has increased dramatically over what can be accounted for from the CB and PI components of the electrode. Such excessive electrolyte decomposition can lead to SEI growth and electrolyte depletion and may be caused by catalytic activity at the cr-CoO electrode surface or the large volume changes associated with the conversion reaction.

3.3.3 Thermoactivation of CoO

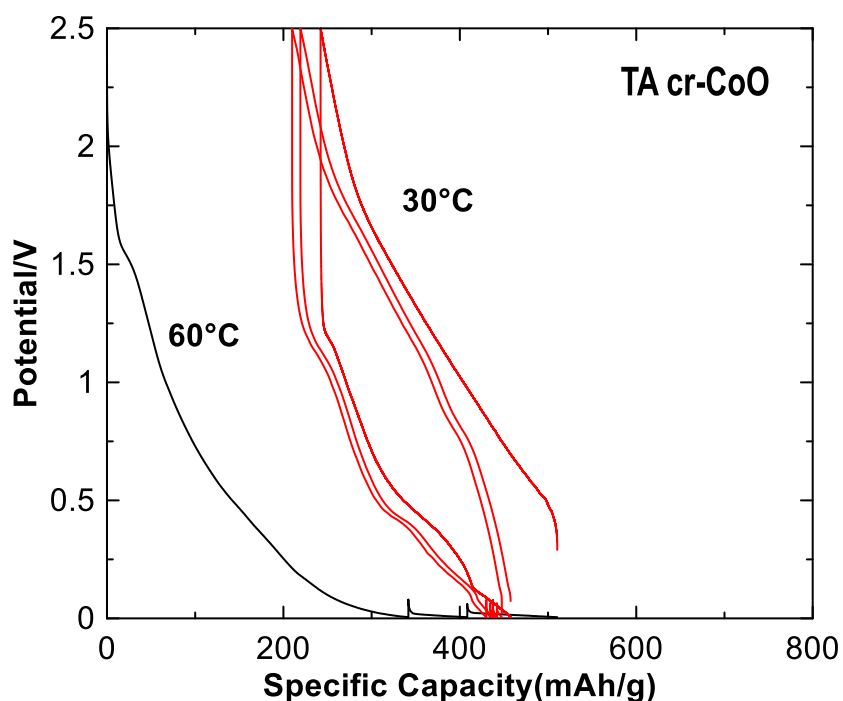


Figure 3.3 Potential vs capacity curve of a thermoelectrochemically activated cr-CoO/CB/PI electrode in a sodium half-cell. The first sodiation (black) was conducted at 60°C and subsequent cycling (red) was conducted at 30°C in a fresh cell

In order to take advantage of the increased electrochemical activity at high temperature, but avoid electrolyte decomposition, the thermoelectrochemical activation method was applied. After a first sodiation at 60°C, cr-CoO cells were then disassembled and the sodiated electrode were assembled in new cells and cycled at 30°C. Figure 3.3 shows the potential vs capacity curve of such a cr-CoO electrode. The first sodiation occurred at 60°C. Then three subsequent cycles

are shown for this electrode at 30°C. Surprisingly, the capacity of this electrode at 30°C is now 220 mAh/g. Therefore, the initial sodiation at 60°C has resulted in the electrochemical activation of the cr-CoO and most of this activity has been retained even at 30°C. In addition, the low reactivity of cr-CoO with electrolyte at 30°C has been maintained, as low electrode slippage occurs in this electrode even though the cr-CoO is now actively cycling. This indicates that most of the electrode slippage at high temperature is likely due to catalytic electrolyte decomposition at the cr-CoO surface and not from the effects of volume expansion.

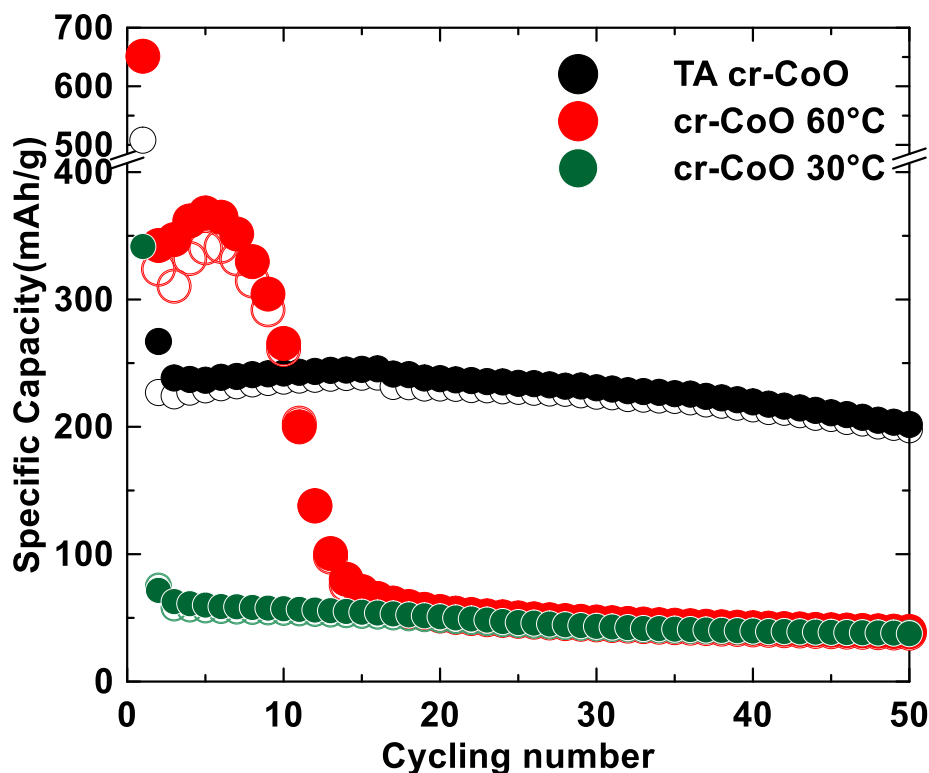


Figure 3.4 Cycling performance of cr-CoO electrodes cycling at 30°C, at 60°C, and thermoelectrochemically activated (TA) cr-CoO electrode (sodiated at 60°C then placed in a fresh cell at 30°C). Closed symbols: sodiation, open symbols: desodiation.

Figure 3.4 shows a plot of the capacity vs. cycle number of the cr-CoO electrodes cycled at 30°C, at 60°C, and the thermoelectrochemically activated (TA) electrode at 30°C. The cr-CoO electrode has low capacity at 30°C. At 60°C the reversible capacity increases from 340 mAh/g to 370 mAh/g during the first 10 cycles, but subsequently there is severe capacity loss. This capacity loss at high temperatures is probably a reflection of severe electrolyte decomposition reactions

encountered when cycling at this temperature as described above. The thermoelectrochemically activated electrode cycled at 30°C has much improved capacity than the electrode without thermoelectrochemical activation and much improved cycling retention (~20% fade from cycles 3-50) than the electrode cycled at 60°C. The greatly improved cycling retention of this electrode compared to the electrode cycled exclusively at 60°C is likely due to the reduced electrolyte reactivity at 30°C. Despite the successful activation of cr-CoO at 60°C, only about 240 mAh/g reversible capacity could be achieved, which is less than half of the CoO theoretical capacity (715 mAh/g). This capacity impotence is likely due to poor kinetics of the conversion reaction, making the core of the relatively large sized cr-CoO particles inaccessible to Na diffusion from the particle surface as suggested in earlier studies.(101)

3.3.4 Activation of CoO by Ball milling

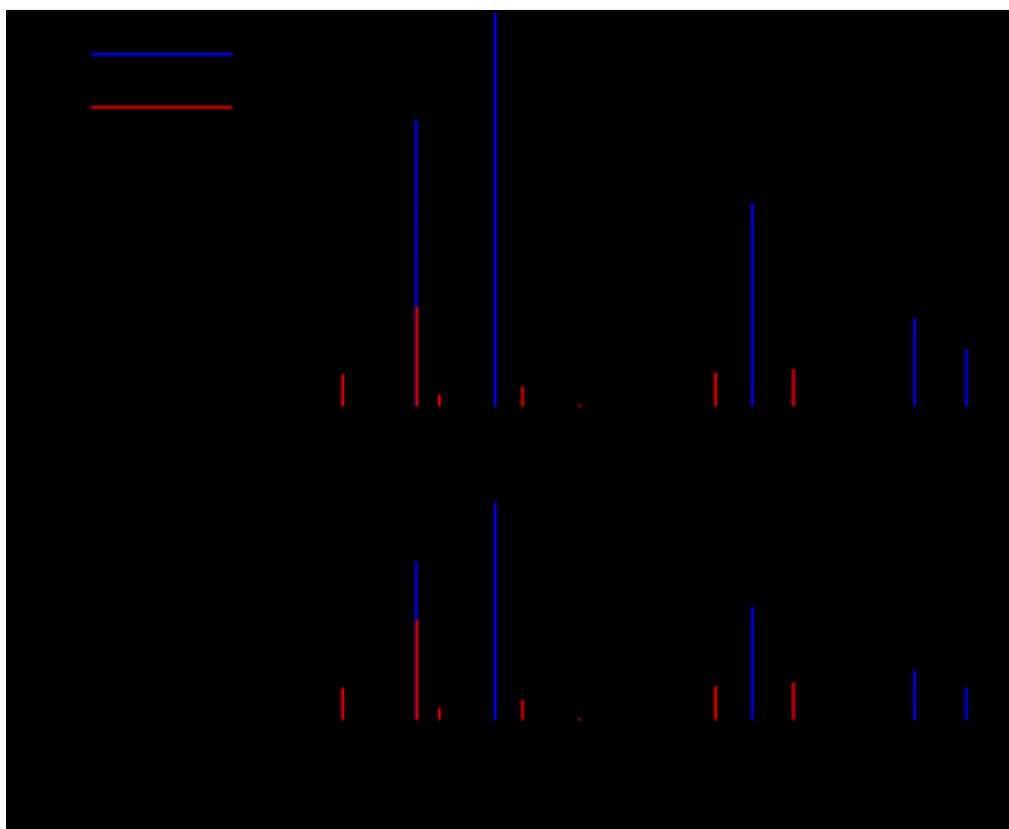


Figure 3.5 The XRD patterns of cr-CoO powder and bm-(CoO/CB)

Reducing crystallite size of binary metal compounds via ball milling with conductive additives has proven to be successful in improving the kinetics such that cycling performance

with lithium is enhanced.⁽¹⁰²⁾ The XRD patterns of cr-CoO and bm-(CoO/CB) are shown in Figure 3.5. The XRD pattern of cr-CoO matches that of the rocksalt phase, excepting the small peak at about 44°, which is likely from a small amount of Co metal impurity in the sample. Small broad peaks are also present in the cr-CoO XRD pattern and are coincident with Co₃O₄. The CoO peaks were broadened by ball milling, indicating a reduction in crystallite size. After ball milling, the average dimension of the crystallites was estimated to be about 50 nm by the CoO (200) peak using the Scherrer equation, which is almost half the grain size of cr-CoO (~97 nm).

3.3.5 Electrochemistry of Ball milled CoO

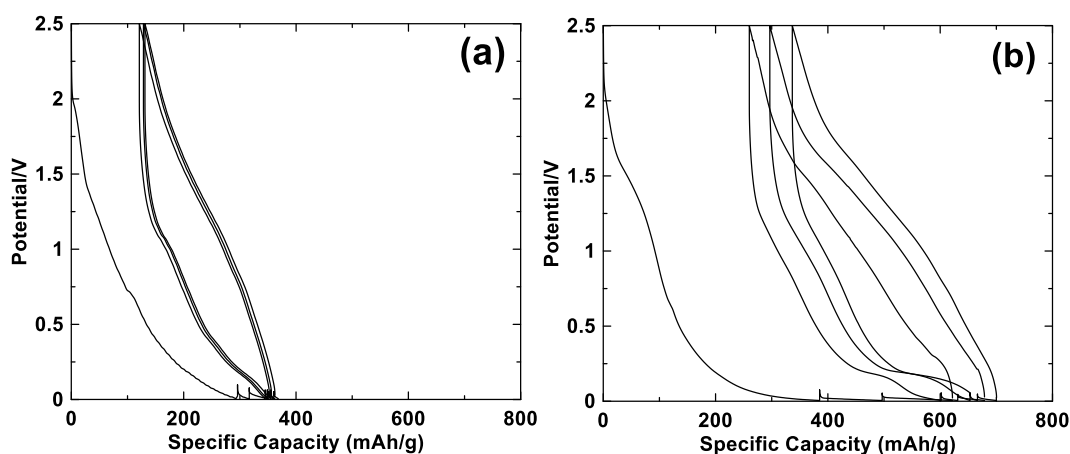


Figure 3.6 Potential vs capacity curves of the first three cycles of bm-(CoO/CB)/PI electrodes in sodium half cells at (a) 30°C and (b) 60°C.

The potential vs capacity curve for the first three cycles of bm-(CoO/SC)/PI sodium half-cells at 30°C and 60°C are shown in Figure 3.6(a) and (b), respectively. Ball milled CoO has a significant reversible capacity of 200 mAh g⁻¹ at 30°C. It appears ball milling CoO with CB is another method to activate CoO for room temperature electrochemistry with sodium. At 60°C, the reversible capacity was higher by 100 mAh/g, but there is also huge voltage curve slippage. This suggests more CoO might be accessed with high temperature sodiation, but that excessive electrolyte decomposition and/or particle disconnection occurs.

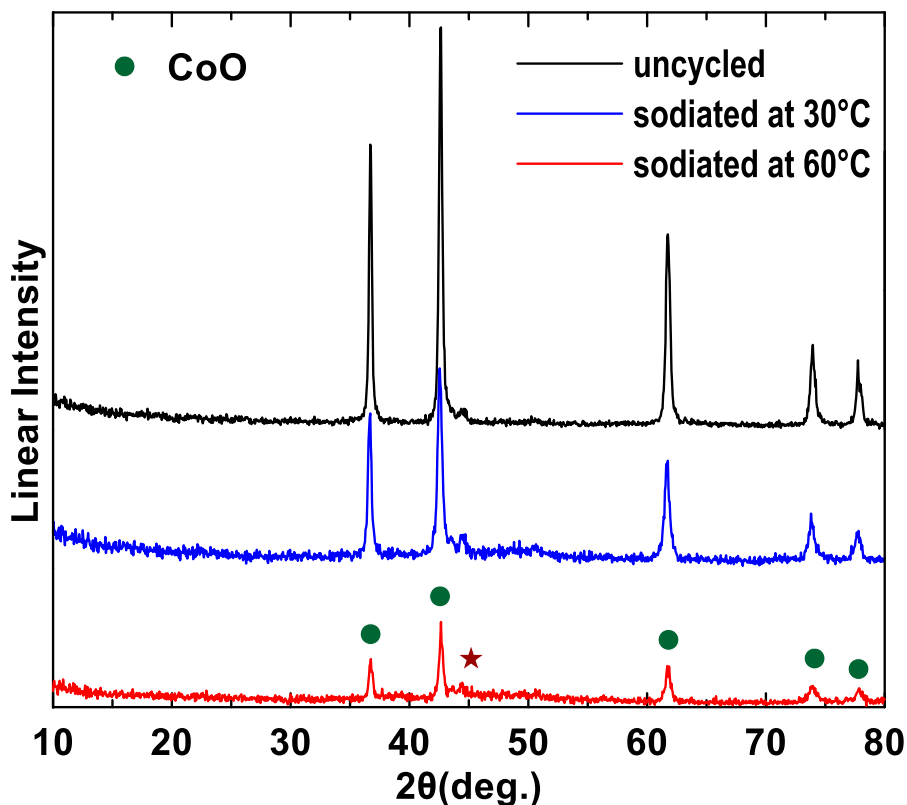


Figure 3.7 XRD patterns of cr-CoO/CB/PI electrodes: as made, after sodiation at 30°C and after sodiation at 60°C. The purple star represents the impurity

Figure 3.7 shows XRD patterns of an uncycled cr-CoO electrode and ones that have been fully sodiated at 60°C and 30°C. After sodiation at 30°C the cr-CoO peak intensity decreases, consistent with its reaction with Na. After sodiation at 60°C the peak intensity drops further, indicating a more complete sodiation reaction at this temperature. Both XRD patterns have increased intensity near 44°C, consistent with the formation of nanocrystalline Co. Features due to the formation of Na₂O, which has a main peak near 46° are difficult to discern from the background. A very broad peak centered near 50° is observed. The origin of this peak is not known, but may be due to SEI components. These results show that there is partial amorphization of the electrode during Na insertion, which is consistent with an incomplete conversion reaction. This is consistent with results from He et al.(101) Kinetics are improved at 60°C, resulting in a much improved achieved capacity, but also a greater degree of electrolyte decomposition.

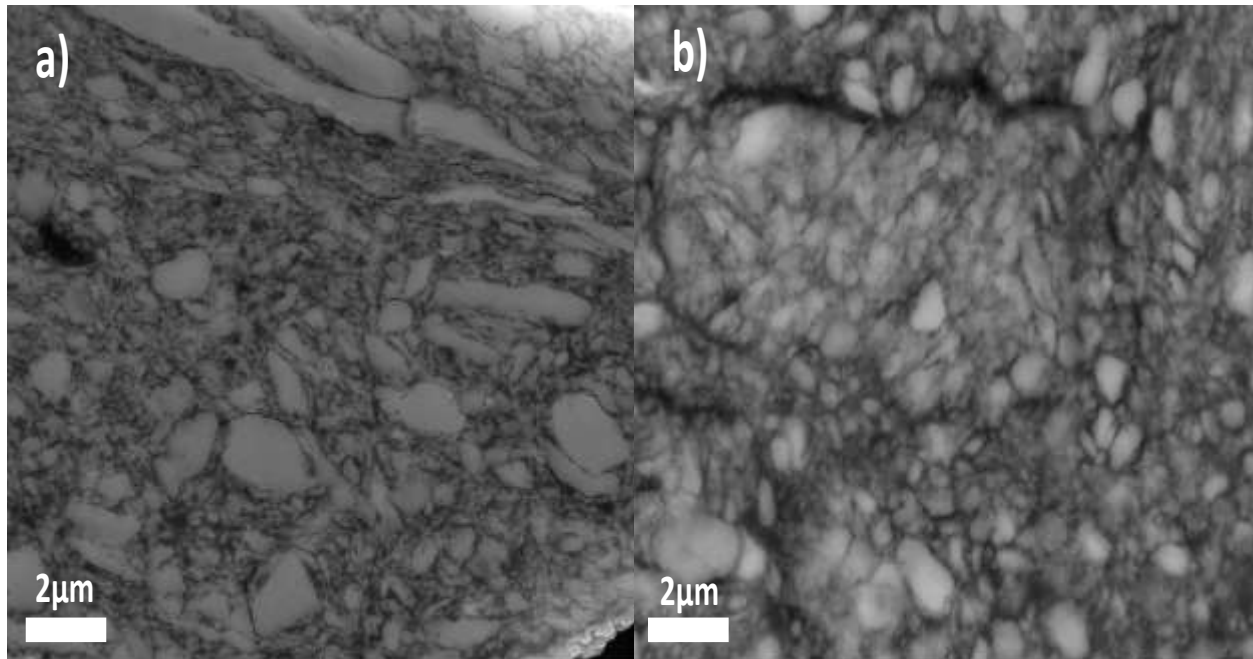


Figure 3.8 SEM images of cross sections of (a) the as-made cr-CoO electrode, and (b) the TA cr-CoO electrode

Figure 3.8 show SEM images of cross sections of the as-made cr-CoO electrode and the same electrode after thermoelectrochemical activation, respectively. The as-made cr-CoO electrode comprises CoO particles with well-defined edges. But after thermoelectrochemical activation, the particles have less well--defined edges and smaller particle sizes. These changes are likely due to particle fracture resulting from volume expansion during sodiation.

3.3.6 Thermochemical Activation of Ball milled CoO

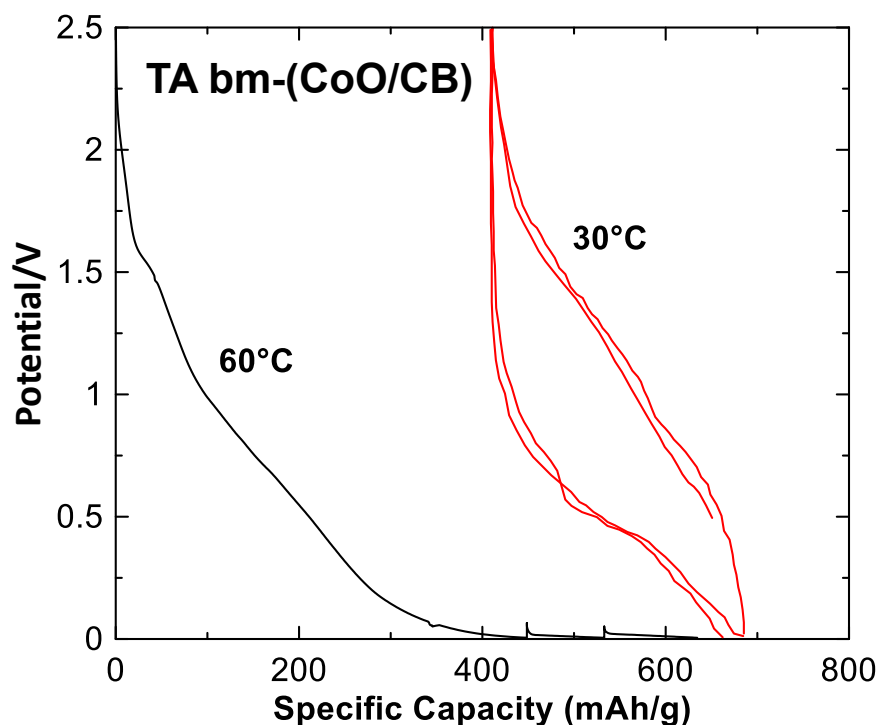


Figure 3.9 Potential vs capacity curve of a thermochemically activated bm-(CoO/CB)/PI electrode in a sodium half-cell. The first sodiation (black) was conducted at 60°C and subsequent cycling (red) was conducted at 30°C in a fresh cell

The above results show that grain size reduction by ball milling and increasing battery cycling temperature both help to increase the CoO capacity. Therefore, increasing temperature and decreasing grain size should simultaneously increase the capacity more than each method used individually. To explore this, cells were constructed using bm-(CoO/SC) and were thermochemically activated at 60°C. The voltage curve of the first three cycles of bm-(CoO/SC)/PI electrodes sodiated at 60°C and then cycled at 30°C in fresh cells is shown in Figure 3.9. As expected, a much larger sodiation capacity (extra ~100 mAh/g) was achieved during the first sodiation of ball milled CoO at 60°C compared to cr-CoO. Surprisingly, a larger reversible capacity is also achieved after this thermochemical activation, when the electrode is subsequently cycled at 30°C.

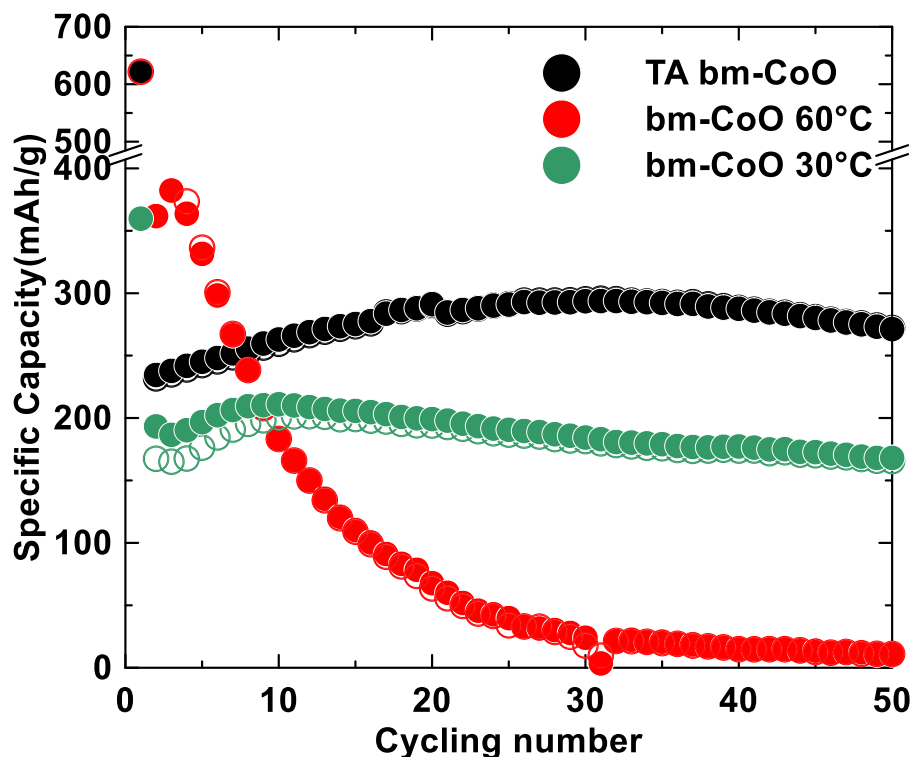


Figure 3.10 Cycling performance of bm-(CoO/CB) electrodes cycling at 30°C, at 60°C, and a thermoelectrochemically activated (TA) bm-(CoO/CB) electrode (sodiated at 60°C then placed in a fresh cell at 30°C). Closed symbols: sodiation, open symbols: desodiation

Figure 3.10 compares the cycling performance of bm-CoO cycled at 30°C, bm-CoO cycled at 60°C, and thermoelectrochemically activated bm-CoO cycled at 30°C. The capacity of bm-CoO cycled at 30°C increases during the first 10 cycles, followed by linear capacity fade. Apparently, more CoO can be accessed during the initial cycling process. This may be due to improved Na diffusion in cracks formed during the large volume expansion/contraction associated with the displacement reaction of Equation 3.1. We speculate that after being pulverized to a certain size, the resulting nano particles no longer fracture, capacity increase no longer occurs, and the material fades due to mechanical failure from repeated volume expansion/contraction. Cycling bm-CoO at 60°C results in rapid capacity fade. This is not surprising, since the higher surface area of the ball milled material combined with high temperature would result in severe electrolyte decomposition, as indicated by the severe voltage slippage of this electrode, shown in Figure 3.6(b). The thermoelectrochemically activated bm-CoO cycled at 30°C has a higher capacity and

improved capacity retention compared to bm-CoO cycled at 30°C. The combination of ball milling and thermochemical activation has made more CoO accessible to Na during cycling. The reversible capacity increases from 230 mAh/g to 295 mAh/g at cycle 30, and then begins to fade. Again, this indicates more CoO can be accessed every cycle to a certain extent.

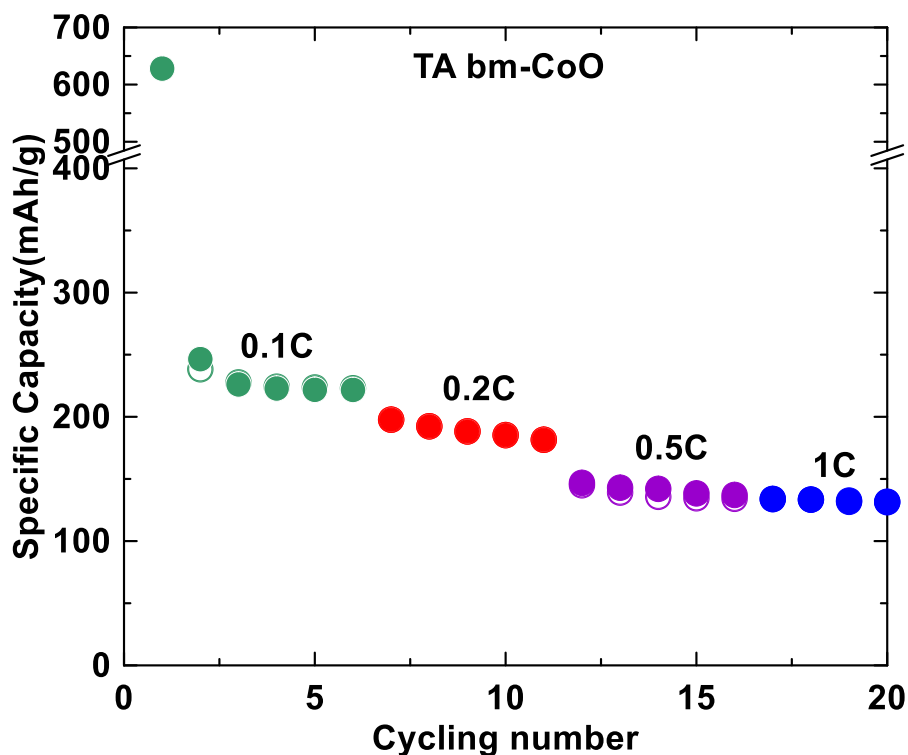


Figure 3.11 Rate performance study of the (TA) bm-(CoO/CB) electrode

The rate performance of bm-TA CoO is shown in Figure 3.11. About 60% of the 0.1C capacity is retained at C-rate cycling. This relatively low rate capability is likely due to the displacement type reaction required for Na insertion/removal, in which bonds must be reformed and broken.

Figures 3.3 and 3.6 demonstrate that thermoelectrochemical and mechanochemical activation are effective methods to activate conversion reactions. Mechanochemical activation alone resulted in a lower capacity and less capacity retention than thermoelectrochemical activation, while cycling at higher temperature resulted in higher capacity, but catastrophic fade. The combination of thermoelectrochemical and mechanochemical methods resulted in the highest level of activation and with the highest capacity retention. As such,

thermoelectrochemical activation and its combination with mechanochemical activation seems to be a promising method of increasing the capacity of kinetically hindered displacement or "conversion" type reactions.

3.4 Conclusions

Thermoelectrochemical activation was used to enable cycling of CoO, which has previously been reported as being inactive at room temperature in sodium cells. Activating CoO by sodiation at 60°C leads to a significant increase in specific capacity when the resulting electrode is cycled at 30°C. Activating CoO by ball milling with carbon black also leads to an increase in specific capacity. Coupling the two activation methods resulted in significantly better cycling performance as well as higher capacity. Using this method, a reversible capacity of nearly 300 mAh/g was achieved during 30°C cycling. However, this is still less than half of the theoretical capacity. Further characterization of the CoO reaction mechanism is required such as X-ray photoelectron spectroscopy or in-situ XRD. Specifically, a detailed investigation of the reaction products is necessary, since these are not fully understood. Due to the large volume expansions associated with the sodiation of CoO improved electrodes electrolytes are required since they seem to have a big impact on electrochemical performance. Nevertheless, the activation methods used in this work provided impressive increases in capacity and capacity retention and therefore are promising methods for use with other kinetically hindered displacement or "conversion" type reactions.

CHAPTER 4 THE IMPACTS OF CARBON DIOXIDE ADDITIVES ON SILICON ALLOY CELLS

4.1 Introduction

The exothermic decomposition of the electrolytes will lead to the gas generation in LIB cells. Many gaseous species have been identified during cell operation, such as CO₂, CO, H₂, etc., but their exact origin and effects on cell performance remain debatable.⁽¹⁰³⁾ Specifically, CO₂ has been shown to be an effective additive for establishing a stable solid electrolyte interphase on graphite electrodes.⁽¹⁰⁴⁾ Recently, Krause et al. have shown that by incorporating CO₂ in the electrolyte of cells with Si-based negative electrode materials, a considerable improvement in cycling performance can be achieved.⁽⁵⁰⁾ Subsequently, Solchenback et al. showed that lithium oxalate can be added to the positive electrode that decomposes as an in-situ source of carbon dioxide during cell operation, resulting in cycling enhancement of Si electrodes.⁽¹⁰⁵⁾ However, as with FEC, the CO₂ is continually consumed during cell operation and higher amounts of CO₂ in the electrolyte result in longer cycle life. Since the electrolyte has a limited solubility for CO₂, pouch cells bulge when a large amount of gas is introduced.

For the practical implementation of CO₂ as an additive, a better understanding of its consumption during cycling is needed. Furthermore, new electrolytes that can dissolve larger amounts of CO₂ would be advantageous to increase cycle life and reduce cell gassing.

In order to study the effect of CO₂ as an additive and to develop new electrolytes with increased CO₂ solubility, the CO₂ content in electrolytes must be quantitatively determined. However, this is not easily done. Methods used for quantitative CO₂ determination in solution include weighing methods, the vapor equilibrium method,⁽¹⁰⁶⁾ chemical absorption rate and gas chromatography–mass spectrometry (GC-MS). However, these methods have unavoidable drawbacks such as either being time consuming, destructive, or requiring large amounts of electrolyte sample. Here, it is shown that Fourier transform infrared spectroscopy (FTIR) can be used as a quick and accurate method for quantitative CO₂ determination in organic Li-ion battery electrolytes. Using this method, the impact of CO₂ additive on the electrochemical properties of silicon alloy cells is also studied.

4.2 Experimental

CO₂ was added to solvent and electrolyte samples without air exposure at 25°C using the procedure and apparatus shown in chapter 2. PC was obtained from BASF (battery grade). A standard electrolyte solution was prepared by dissolving 1 M LiPF₆ (BASF 98%) in EC, DEC (1:2 v/v, <50 ppm H₂O, BASF) by volume in an argon-filled glove box. Working electrodes consisted of V6 silicon alloy (3M), SFG6L (Imerys Graphite and Carbon), carbon black, and LiPAA {(lithium polyacrylate from a 10 wt% aqueous solution made by neutralizing a PAA solution (Sigma-Aldrich, average molecular weight ~250,000 g/mole, 35 wt% in H₂O) with LiOH·H₂O (Sigma Aldrich, 98%) in distilled water} (27) in a weight ratio of 60:28:2:10. 3M V6 alloy is "an active/inactive alloy where the Si domains and the inactive domains are less than 15 nm and evenly distributed throughout a micron size particle." It has a reversible capacity of ~900 mAh/g (1550 Ah/L), corresponding to a 105% volume expansion and a high initial coulombic efficiency of about 87%.⁽¹⁰⁵⁾ In our own experiments we have measured the capacity of V6 alloy to be 930 - 950 mAh/g. Excellent cycling characteristics have been demonstrated for this alloy, making it a good standard material for electrolyte evaluation studies. Further information regarding the electrochemical properties of this alloy can be found in References 50 and 104. The V6 alloy, CB and LiPAA components and additional distilled water were thoroughly mixed with three tungsten carbide balls in a Retsch PM200 rotary mill (100 rpm, 60 mins) to create a uniform slurry. The slurry was then coated onto copper foil (Furukawa) and dried at 120 °C in air for 1h. Following the drying process, coatings were punched into circular electrodes with an area of 1.3 cm² and dried under vacuum for 2h to remove excessive moisture.

Coin half cells (2325 type) were assembled in an Ar-glove box with V6/SFG6L working electrodes, lithium metal reference/counter electrodes, two Celgard 2300 separators (to avoid cell shorts from possible imperfections in hand-made electrode coatings) and about 100 μL of electrolyte. Cells were tested at 30.0 ± 0.1 °C using a Neware battery testing system at 0.1C for the first cycle and 0.2C for subsequent cycles in a voltage range of 5 mV - 0.9 V. Here C-rate is defined as the current required to fully lithiate the V6/SFG6L in the electrode based on a theoretical capacity of 950 mAh/g and 360 mAh/g for V6 and SFG6L, respectively.

FTIR spectra were measured and analyzed as mentioned in chapter 2.

4.3 Results and discussion

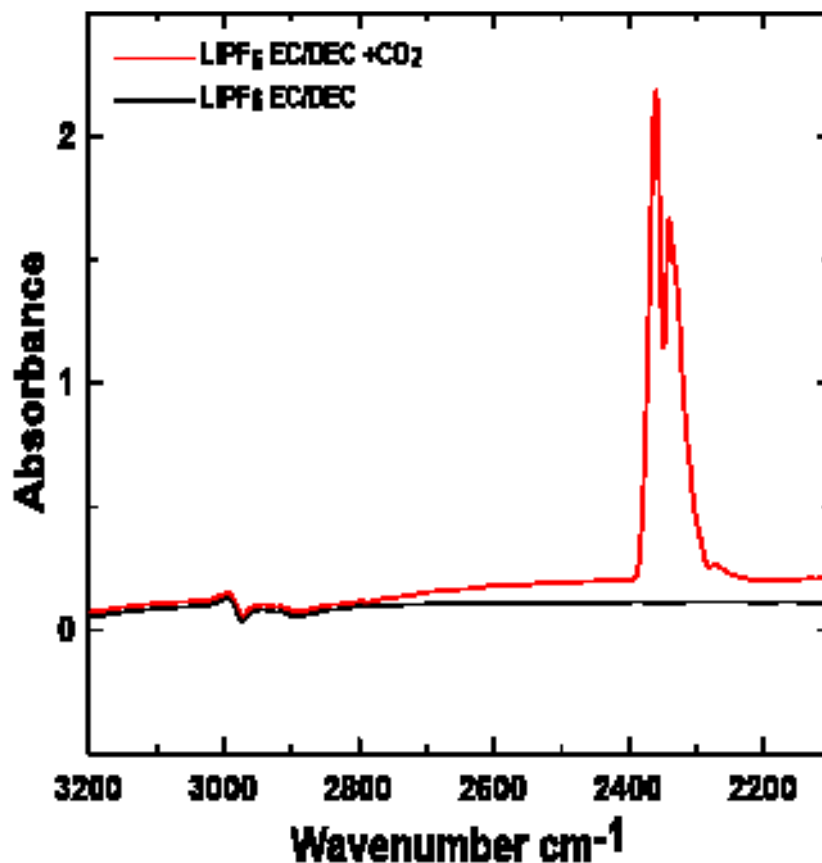


Figure 4.1 IR spectra of 1M LiPF₆ in EC/DEC solutions without CO₂ and saturated with CO₂.

Figure 4.1 shows the FTIR spectra of 1 M LiPF₆ in 1:2 EC:DEC (v:v) electrolyte saturated with CO₂ and without CO₂. There are two large peaks present in the CO₂-containing electrolyte at 2340 cm⁻¹ and 2360 cm⁻¹, whereas no features are present in this region for the electrolyte without CO₂. These peaks have been observed previously and assigned to CO₂ by Yang et al.(81) Since they appear in a region where the pure electrolyte has no features, these peaks are excellent candidates for the quantification of CO₂ content. According to FTIR quantification theory, the integrated peak area has a linear relationship with the concentration of dissolved species.(106) Therefore, the area of the spectrum near the 2350cm⁻¹ region can indicate the exact amount of CO₂ component in the electrolyte.

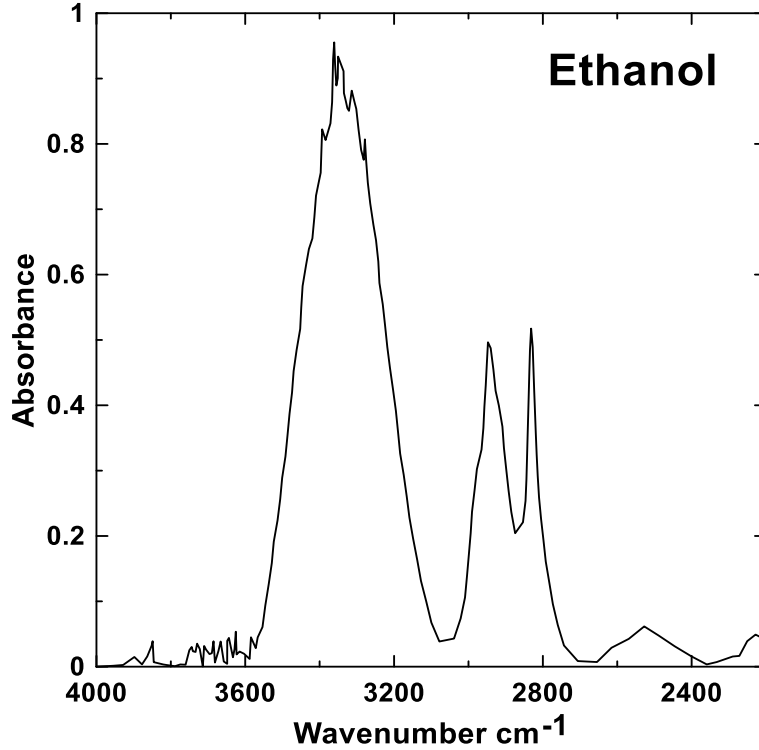


Figure 4.2 IR spectrum of ethanol

To establish a quantitative FTIR method, PC was chosen as a standard solution because it has a low vapor pressure and is able to dissolve more CO₂ than other electrolyte solvents.(107) The weight change of a PC sample before and after bubbling with CO₂ at 5 °C was measured and FTIR spectra were also collected. The concentration of CO₂ in PC after bubbling CO₂ for 100 minutes at 5 °C was 0.74 wt.% as determined by weight difference, which agrees well with the solubility limit measured by Blanchard et al.(107) at this temperature, verifying our weight difference analysis. This 5 °C saturated 0.74 wt.% CO₂ solution was used as a standard solution in following measurements and will be referred to as the "standard solution". To take into account any variations caused by sample loading or changes in the FTIR light source intensity over time, anhydrous 100% ethanol (100% Alfa) was used as an intensity standard. As shown in Figure 4.2, the ethanol FTIR spectrum has three distinct peaks that do not interfere with peaks from CO₂. Using the area under these peaks, the CO₂ concentration in electrolytes can be determined by:

$$\left(\frac{A_{CO_2,sample}^0}{A_{EtOH}^0}\right) / \left(\frac{A_{CO_2,standard}^1}{A_{EtOH}^1}\right) = C_{CO_2,sample} / C_{CO_2,standard} \quad (4.1)$$

Where $A^{0}_{CO_2,sample}$ and $A^{0}_{CO_2,standard}$ are the areas of the 2350 cm^{-1} CO_2 peaks in the electrolyte sample to be measured and the standard solution, respectively, A^{0}_{EtOH} is the total area of the three ethanol peaks in a sample of pure ethanol measured directly after the electrolyte sample FTIR measurement and A^{1}_{EtOH} is the total area of the three ethanol peaks in a sample of pure ethanol measured directly after the standard solution FTIR measurement. The CO_2 absorption peaks are not symmetric, so trapezoidal integration was used to calculate the area under peaks using Omnic analysis software. The integral region was fixed from 2400 cm^{-1} to 2280 cm^{-1} .

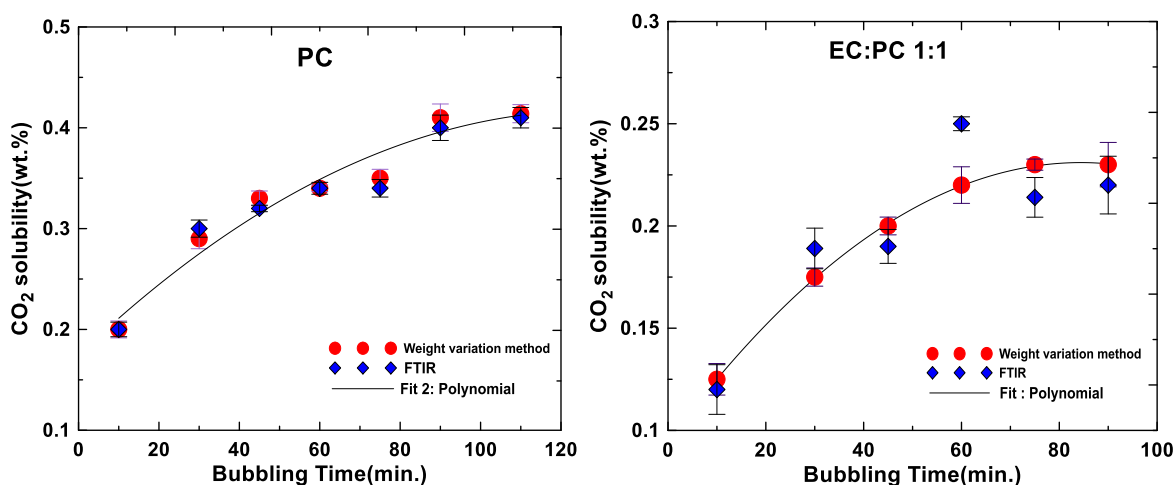


Figure 4.3 CO_2 solubility results from FTIR and weight variation methods in 1 M $LiPF_6$ PC(a) and EC:PC 1:1 (b) measured at $25^\circ C$, respectively. Fitted trendlines are added as a guide to the eye.

In order to test the validity of our FTIR quantitative method, measurements were made of CO_2 solubility after different CO_2 bubbling times in PC at $25^\circ C$ using both the weight variation and FTIR methods. As shown in Figure 4.3, both measurements agree closely and show that the CO_2 content increases roughly linearly with bubbling time. The variation between the weight and FTIR methods is $\pm 0.007\text{ wt.}\%$ or $\pm 3\%$ of the total CO_2 content measured in the sample. The experiment was also repeated for a EC:PC 1:1 (v:v) solution. For this solution, there is less CO_2 solubility and a correspondingly larger error between the FTIR results and the weight variation method. Nevertheless, the error between the two methods at these low CO_2 concentrations is $\pm 0.01\text{ wt.}\%$ or $\pm 7\%$ of the total CO_2 content measured in the sample. These experiments demonstrate that the FTIR method can be used for the quantitative measurement of CO_2 in

electrolytes for CO₂ concentrations at least within the concentration ranges measured in this study: i.e. above about 0.1 wt %, however it is possible that the method could be extended to the analysis of solutions with lower CO₂ content.

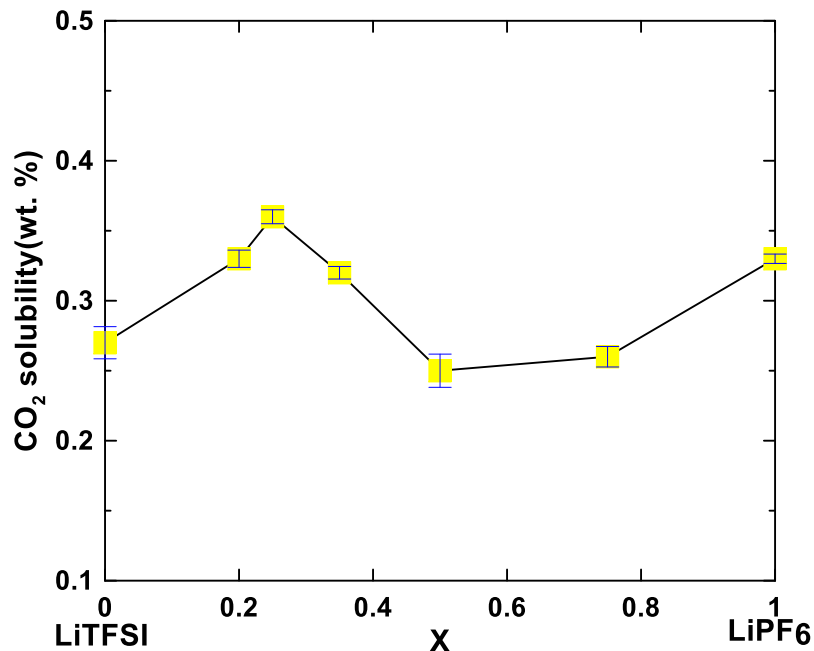


Figure 4.4 CO₂ solubility in EC/DEC 1:2 solvent with 1M of LiTFSI and LiPF₆ salt mixtures measured at 25°C, where x is the mole fraction of LiPF₆.

In order to demonstrate the utility of the FTIR method, measurements of CO₂ solubility in EC/DEC 1:2 v/v solvent containing 1M of LiPF₆/LiTFSI salt blends was investigated. The solubility of CO₂ in these electrolytes is shown in Figure 4.4. As the LiTFSI content is increased, the CO₂ solubility also decreases, until the LiTFSI content is 50 mole%. Further additions of LiTFSI result in an increased CO₂ solubility, until a maximum solubility of 0.37 wt.% is reached for a 75 at.% LiTFSI and 25 at.% LiPF₆ salt blend. These results show that the CO₂ solubility can have a complex dependence on the electrolyte composition and, furthermore, that the salt anion can significantly affect CO₂ solubility.

Table 4.1 Solubility of CO₂ in different solvents with 1M LiPF₆ electrolyte measured at 25°C.

Electrolyte (1M LiPF₆)	CO₂ solubility(wt.%)
PC	0.40±0.02
EC/PC 1:1	0.22±0.04
EC/DEC 1:2	0.33±0.07
EMC	0.39±0.04
DEC	0.35±0.02
EC/DMC 1:1	0.39±0.03

The CO₂ solubility of 1M LiPF₆ dissolved in different solvents was also measured and is summarized in the Table 4.1. These results show that for 1M LiPF₆ solutions, CO₂, as a non-polar molecule, is more soluble to solvents with low dielectric constants, so CO₂ has a relatively higher solubility in DMC, EMC and DEC. Meanwhile, CO₂ solubility is in the order of PC ≈ EMC > DEC for the pure solvents. This is a different trend than found by Blanchard et al., who found that the solubility of CO₂ in DEC was higher than that of PC.⁽¹⁰⁷⁾ However, Blanchard et al. studied pure solvents that contained no salts. In addition, as shown in Dougassa's⁽¹⁰⁸⁾ result, solvent shells formed by CO₂ molecules will be significantly reconstructed in PC/LiPF₆ electrolytes as a result of their strong interactions. The new solvent shells tend to bond more CO₂ molecules, so CO₂ solubility in PC electrolytes increased and became slightly higher than EMC. For mixed solvents with EC, the largest solubility of CO₂ occurs for EC/DMC, which has nearly the same CO₂ solubility as PC. Thus EC/DMC blends might be beneficial when high CO₂ contents are desired.

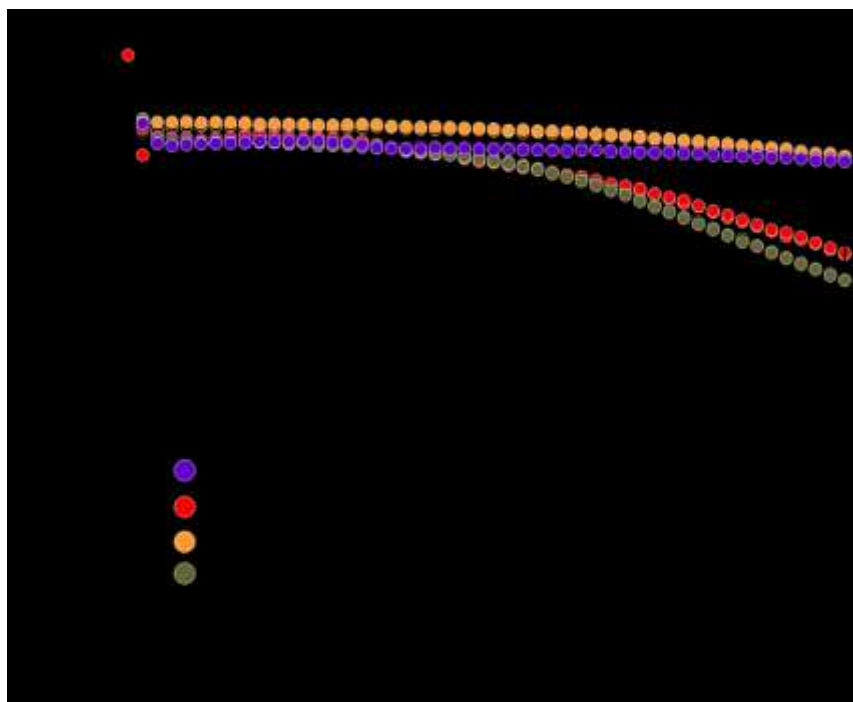


Figure 4.5 Cycling performance of V6 Electrodes in 1M LiPF₆ in EC:DEC electrolytes saturated with CO₂ and without CO₂. Cells with FEC additives are also shown for comparison.

To demonstrate the importance of CO₂ as an electrolyte component, the cycling performance of 3M V6 alloy was measured in 1M LiPF₆ electrolytes with EC/DEC 1:2 v/v solvent with and without CO₂ and FEC additives. The cycling performance of these cells is shown in Figure 4.5. The cell with no CO₂ or FEC additives fades quickly after 20 cycles. This is typical of alloy cells that require special additives to reduce electrolyte consumption due to the disruption of the SEI layer during alloy volume expansion. The addition of 0.25 wt% CO₂ to the electrolyte has little effect on the cycling performance. Increasing the CO₂ content to 0.33 wt% results in cells with little fade over the 50 cycles tested. This is in agreement with the recent results of Krause et al., who showed that higher CO₂ contents result in more improved cycling.⁽⁵⁰⁾ Cycling performance is also improved with the addition of 10 vol% FEC to the electrolyte, however, the improvement is not as great as for 0.33 wt% CO₂. Electrolytes with even higher CO₂ contents may result in even longer cycle life. Therefore, studies of the CO₂ content in electrolyte are important. The FTIR method presented here is well adapted to the rapid evaluation of CO₂ solubility in different electrolyte systems.

As discussed above, higher CO₂ contents (more than 0.33%) will extend the cycle life of silicon alloy cells. Therefore, several methods to increase CO₂ solubility in the electrolyte have been attempted. Some chemicals reported as “CO₂ scavengers” are extensively used in the capture of CO₂. Diethylenetriamine (DETA) with two groups as primary amines and one group as a secondary amine within its structure as shown in figure 4.6. It can form multiple carbamate species in CO₂ loaded solutions.(109) In this work, a certain amount of DETA was added into EC/DEC solution. Its impact on CO₂ solubility is shown in Figure 4.6.

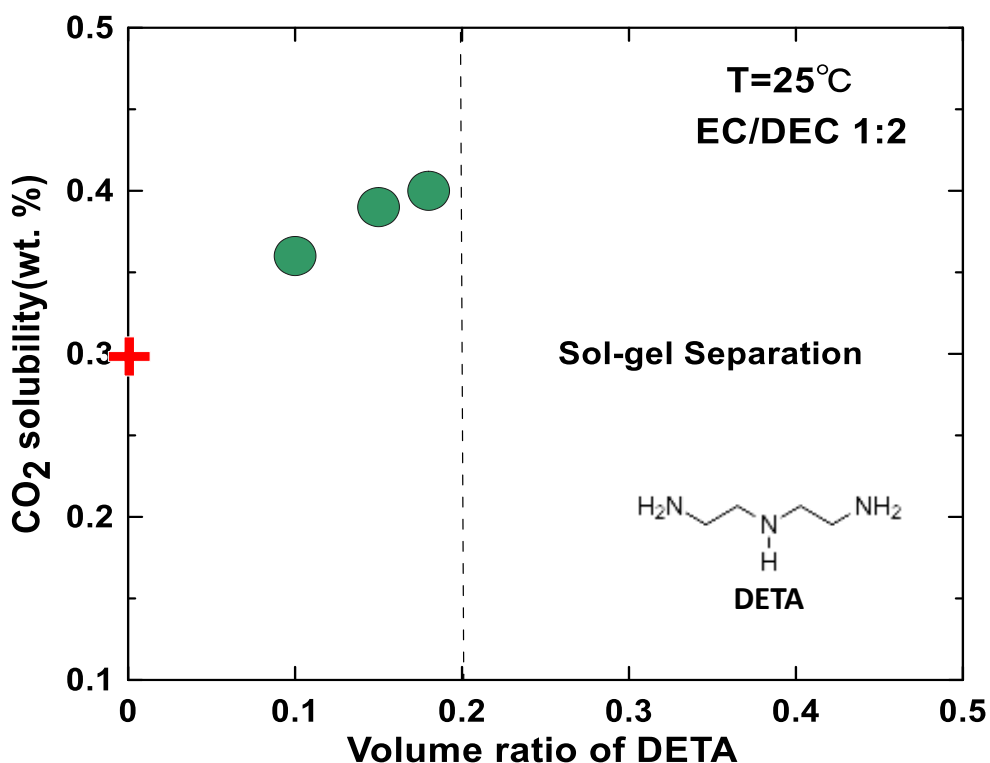


Figure 4.6 CO₂ solubility in EC/DEC 1:2 solvent with 10%,15%.18% DETA including the molecular sketch of DETA. The red cross marks the value without DETA. The dashed line indicates the beginning of phase separation.

Figure 4.6 shows the benefits of DETA on capturing the CO₂ and increasing its solubility at low concentration. As a higher ratio of DETA is added, more CO₂ is dissolved. CO₂ solubility shows a noticeable growth trend to 0.4% when 18% DETA is present in the solution. However, excessive DETA (over 20%) causes sol-gel separation. This experiment indicated a low concentration of CO₂

scavengers like DETA can effectively incorporate more CO₂ in solutions, but phase separation needs to be avoided.

4.4 Conclusions

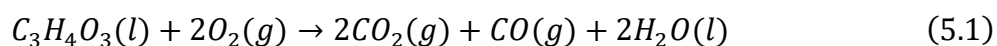
It was shown that CO₂ concentration can be accurately determined in electrolyte solutions using FTIR. This method is much more convenient than weighing methods and much smaller electrolyte volumes are required. Using this method, it was shown that the CO₂ solubility in EC/DEC 1:2 v/v solutions containing 1M Li⁺ depends significantly on the salt anion and in a complicated manner. The cycling performance of Si alloy cells was also shown to depend significantly on the CO₂ content in the electrolyte. CO₂ scavengers like DETA can increase the CO₂ solubility effectively at a low concentration, but higher concentrations of DETA cause phase separation. The FTIR method presented here is well adapted to the rapid evaluation of CO₂ solubility in different electrolyte systems. This can help gain an understanding of CO₂ solubility and allow for the rapid development of high performance electrolytes.

CHAPTER 5 ENHANCING NMC/SILICON ALLOY FULL CELL CYCLING BY ADDING WATER TO THE ELECTROLYTE

5.1 Introduction

In Chapter 4, CO₂ was shown to be an excellent additive for the enhancement of silicon alloy cycling. A higher CO₂ content was found to sustain a longer cycling life. However, since the CO₂ solubility in electrolyte is low, there are few practical ways to introduce CO₂ into electrolyte or cells. For example, adding dry ice directly into pouch cells results in improved cycling, but causes swelling of the pouch.⁽⁵⁰⁾ Using CO₂ scavenger additives, as discussed in Chapter 4, gives rise to phase separation when the additive amounts are increased. Thus, finding a proper method to incorporate CO₂ into cells is needed.

In order to maximize the CO₂ content in silicon alloy cells, in-situ gas generation is a promising method. As is reported previously, gas generation in LIB cells is mainly associated with reactions at the cathode, but the kind and the quantity of gas may vary significantly based on different interactions between cathode materials and electrolytes. In the case of LiCoO₂/graphite cells, the onset of CO₂ generation is usually around 3V, but the amount of CO₂ is minimal.⁽¹¹⁰⁾ In contrast, CO₂ formation is considerable if Mn or Ni are present in the cathode, even at a low potentials between 3.6 V and 4.1 V.⁽¹¹⁰⁾ Therefore, NMC could potentially generate CO₂ in-situ as full cells are cycled. Gasteiger et al. conducted a comprehensive study on the origin of CO₂ generation on the NMC surface and concluded that the oxygen release from the NMC is associated with CO₂ generation,⁽¹¹¹⁾ as opposed to the previous consensus that lithium carbonate impurities produced the CO₂.⁽¹¹²⁾ They proposed a mechanism that in the aid of free oxygen produced from NMC decomposition, EC will decompose and produce both CO and CO₂ as shown in the equation below.



The water produced by this reaction can be reduced at the anode to produce H₂ and OH⁻. Finally, the OH⁻ produced at the anode can react catalytically with EC, causing further CO₂ formation. In these studies of full cells with graphite anodes, the in-situ generation of CO₂ was viewed as undesirable. However, in full cells with Si-alloy anodes, the generation of CO₂ by

deliberate additions of water to the electrolyte may be desirable and lead to an increase of cycle life.

In this chapter, water was intentionally added into NMC/silicon alloy and LCO/silicon alloy full cells. Results showed the cycling performance of NMC/silicon full cell are greatly improved by the water additive. In fact, the addition of water resulted in an improvement in cycling similar to that achieved by traditional additives like FEC. Interestingly, the water additive has little impact when LCO is used as a cathode. This different behavior and corresponding mechanisms will be discussed in this chapter.

5.2 Experimental

Silicon alloy negative electrodes consisted of V6 silicon alloy (3M), SFG6L (Imerys Graphite and Carbon), carbon black (CB, Super C65, Imerys Graphite and Carbon), and a 10 wt% aqueous solution of LiPAA (made by neutralizing PAA solution (Sigma-Aldrich, average molecular weight~250,000 g/mole, 35 wt% in H₂O) with LiOH·H₂O (Sigma Aldrich, 98%) in a weight ratio of 44:44:2:10 in distilled water. These components were thoroughly mixed in with three tungsten carbide balls in a Retsch PM200 rotary mill (100 rpm, 60mins) to create a uniform slurry. The slurry was then coated onto copper foil (Furukawa) and dried at 120 °C in air for 1h. Graphite electrodes were composed of 90 wt% MAGE (MAGE, Hitachi), 5 wt% poly(vinylidene fluoride) (PVDF, HSV 900, KYNAR), and 5 wt% carbon black (CB, Super C, Timcal). The coating procedures are identical to the silicon alloy electrodes. The loading mass of all anodes was approximately 2.6 mAh/cm².

NMC positive electrodes were made by Novonix Battery Testing Services Inc., Bedford, Nova Scotia, Canada. LCO electrodes were made of LiCoO₂ (XD20, Umicore), PVDF, and carbon black in a weight ratio of 94:3:3 with NMP used as a slurry solvent. The slurry was mixed using the same conditions as the anode slurries, then coated onto aluminum foil and dried at 120 °C in air for 1h. All hand coated electrodes were calendered by an adjustable gap calender with 6" diameter rolls (DPM Solutions, Nova Scotia, Canada) to achieve a porosity of 20~30%. All coatings were punched into 2.52 cm² circular disk electrodes. The major parameters of all electrode

coatings are listed in Table 5.1. All hand-coated electrodes were dried in vacuum overnight prior to cell assembly.

For LCO half cells, LCO electrodes were transferred into an argon-filled glove box and assembled in 2325 coin-type cells with a lithium foil reference/counter electrode and an electrolyte composed of 1M LiPF₆ (BASF) in a solution of EC/DEC (1:2 v/v, <50ppm H₂O, BASF). Two layers of Celgard 2300 separators, a stainless steel spacer and a stainless steel spring were used in this cell. These cells were cycled at 30.0 ± 0.1 °C with a Maccor Series 4000 Automated Test System between 3 V and 4.4 V at 0.1C for the first cycle and 0.2C for subsequent cycles.

Full coin cells were assembled using an electrode alignment jig, as described in chapter 2. These full coin cells were filled with 1 M LiPF₆ in EC, DEC (1:2 v/v the same as above) electrolyte (control) with the optional addition of 10 Vol% FEC, or water (500 or 1000 ppm) as follows: control (EC/DEC no additives), control + 10% FEC, control + 500 ppm water, control + 1000 ppm water, control+2% FEC + 1000 ppm water, control+5% FEC + 1000 ppm water. These cells were cycled at 30.0 ± 0.1 °C with a Maccor Series 4000 Automated Test System between 3 to 4.2 V for cells with graphite, and 3 to 4.4 V for cells with silicon alloy. Full cells were cycled galvanostatically at 0.1C for the first cycle and 0.2C for subsequent cycles. The calculation of C-rate is based on the capacity of individual active materials as discussed in the chapter 2.

In addition, in order to analyze the gas composition after cell cycling, NMC-graphite pouch cells (Novonix Ltd.) were also made and filled with and without water. These cells were cycled with the same cycling protocol as the NMC-graphite cells above. After cycling, two extraction methods were employed. The first method was to soak the pouch cells into PC solvent in a glove box for three hours, then the solvent was transferred to the FTIR sample holder for FTIR measurement. The analysis of FTIR samples used the same method as described in chapter 4. Gas chromatography (GC) was also used for gas analysis. GC is a common technique in analytical chemistry for separating and analyzing compounds. The typical GC has a carrier gas, an injector, the separation column located in a temperature controlled oven and a detector. The majority of separation columns are long and narrow capillary tubes with a polyimide coated fused silica lining.⁽¹¹³⁾ When a gaseous sample is injected into the instrument the carrier gas will transport

the sample through the column where the sample interacts with the stationary phase. Different components will interact with the column to different degrees and exit from the column at different times. As a result, the sample will be separated, and individual components will be detected one by one by the detector if suitable conditions are applied. In this chapter, the gas in the pouch cells was collected by extracting gas from the jelly roll mandrill after cycling using a 100 μ l syringe. The gas was then injected into the GC immediately. The oven temperature was 230 °C and the carrier gas was chosen to be He. The overall separation time was 40 minutes, which was long enough to detect all gaseous compounds in the sample.

Electrodes	Specific capacity (mAh/g)	Loading mass (mAh/cm²)	
LCO	~150(4.2 V) ~170(4.4 V)	2.3(4.2 V) 2.4(4.4 V)	Table 5.1 Major parameters of all electrode coatings used.
NMC	~150(4.2 V) ~170(4.4 V)	2.3(4.2 V) 2.4(4.4 V)	
Si V6/SFG6L	650	2.7	
MAGE	360	2.7	
	360	2.6	

5.3 Results and discussions

5.3.1 NMC-graphite full cells

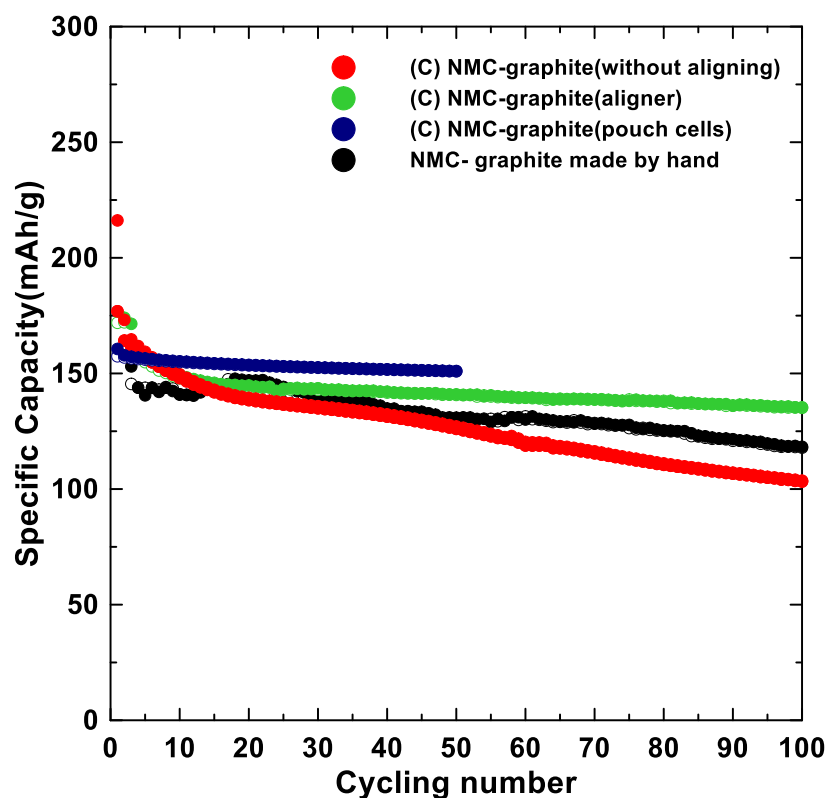


Figure 5.1 The cycling performances of NMC-graphite without aligning, aligner, and hand made graphite. Letter C indicates these electrodes are from Novonix commercial NMC-graphite pouch cells. The data of pouch cells cycling is from the Novonix company

Figure 5.1 compares NMC/graphite coin cells and pouch cells made using commercially coated and hand coated electrodes, and made with and without an alignment jig, as indicated. For full coin cells made with commercial NMC and graphite coatings, the cells made without utilizing the alignment jig suffered from unstable cycling and fade. In contrast, excellent cycling was achieved (cycles 15-100) in full coin cells made with commercial electrodes when an alignment jig was utilized during their construction. In fact, the fade is identical to the data from commercial pouch cells. However, severe capacity fade was observed during the first 15 cycles in both aligned and unaligned cells. This fade could arise from SEI formation in cells that have not had formation cycles. Therefore, an optimized cycling protocol needs to be further studied for a better SEI formation to suppress side reactions. These results illustrate that using the aligner can

easily solve the misalignment issue in full coin cells resulting in more stable cycling with less fade. The cells with the hand made graphite were also assembled to pair with Novonix NMC electrodes. The cycling performance is acceptable with 10% capacity loss after 100 cycles. This indicates that the technique for hand made coatings is reliable for making different kinds of electrodes for other full cells in this thesis.

5.3.2 Karl Fischer results

Table 5.2 Karl Fischer results of samples with different water contents.

Water content estimation	Karl Fischer results(ppm)
Standard (1MLiPF ₆ EC:DEC 1:2)	(3.0±0.3)*10
Standard + 250 ppm H ₂ O	(3.0±0.4)*10 ²
Standard + 500 ppm H ₂ O	(5.7±0.6)*10 ²
Standard + 1000 ppm H ₂ O	(9.8±0.4)*10 ²

In order to verify the added water content, the Karl Fischer titration was conducted to obtain the actual water content in electrolyte samples. Overall, Karl Fischer results are consistent with estimated water content with only 10% error. However, the Karl Fischer titration used in this thesis can be improved. A minimal amount of Iodine will react with carbonates during the measurement, so it will lead to an extra consumption of iodine giving a higher result. Thus, the method will become more accurate if the reactant has a less reactivity with carbonates.

5.3.3 NMC-silicon alloy full cells

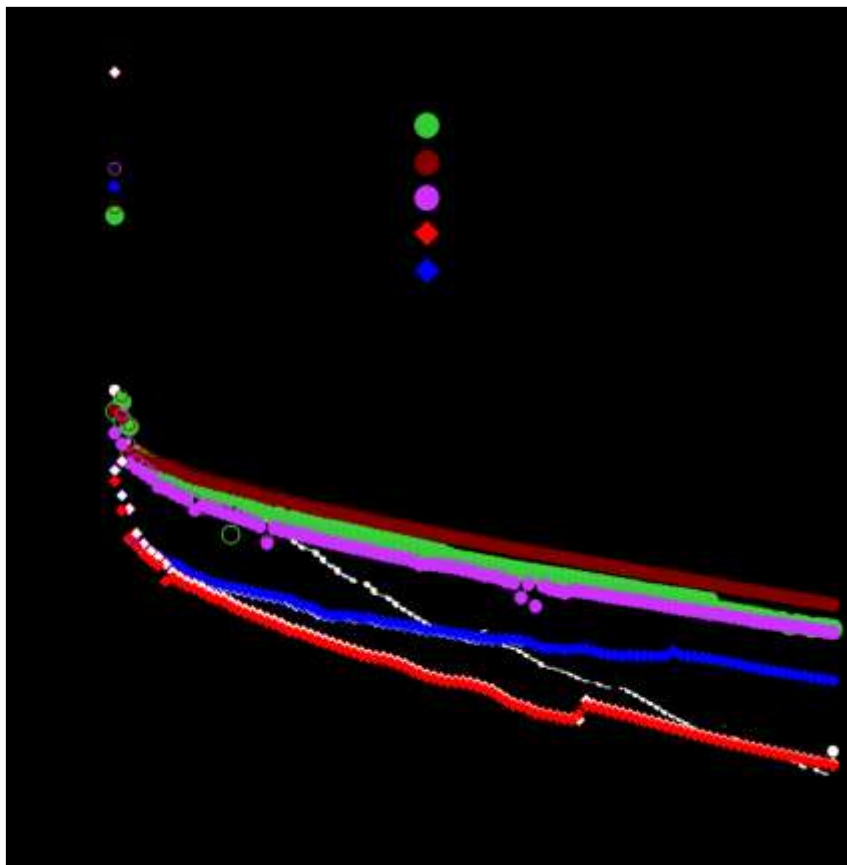


Figure 5.2 The cycling performance of NMC-V6/SFG6L full cells with different additives. The N/P ratio is 1.13

Figure 5.2 shows the enhancement in cycling performance of NMC-V6/SFG6L full cells by the water additive. The cells containing 1000 ppm water have a dramatic improvement on the cycling stability comparing to cells without any additives. Its capacity retention is 82% after 100 cycles analogous to cells with 10% FEC. However, if the water content reduces to half, it starts to lose capacity after 80 cycles. This result indicates two things. First, the water additive may be consumed continuously during the cells cycling. Second, a critical concentration point may exist for the water additive to be functional. It is expected that the consumption rate of water additives on silicon surface is even higher since more surface area will be generated by the massive structural changes associated with cycling a silicon alloy. In addition, the combination of dual additives has been attempted to extend the cycling even longer; however, no significant

difference was found. These results are surprising and can give some insights for further artificial SEI design on the silicon. The SEI created by FEC contains both fluorine and oxygen. Therefore, including sources for both these elements in the electrolyte may lead to good cycling on silicon surface.

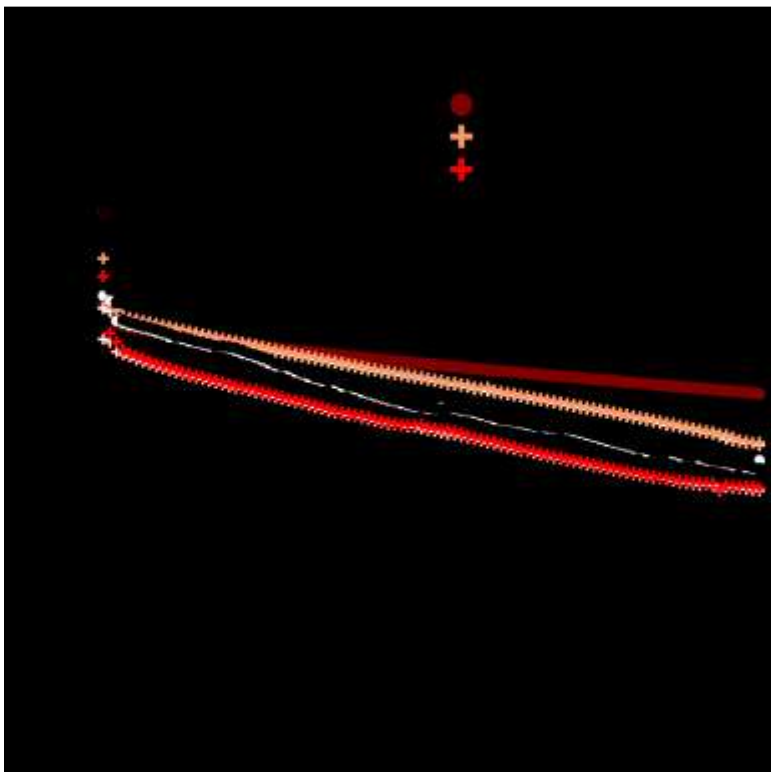
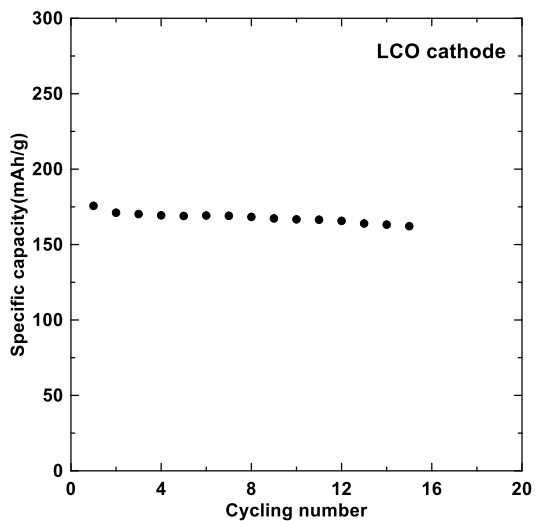


Figure 5.3 The cycling performance of LCO half cells (top) and NMC/V6-SFG6L vs LCO/V6-SFG6L full cells with and without water additive. (bottom) The N/P ratio is 1.13.

In order to demonstrate the benefits of water additive on different cathodes, the cycling performance of NMC/V6-SFG6L is compared with LCO/ V6-SFG6L with and without water additive in Figure 5.3. When there is no water additive in the system, LCO shows a similar capacity fading trend as NMC, and this capacity loss can be attributed to the mechanical failure of the silicon alloy, since no capacity fade was observed in LCO half cell cycling. When water is added to the electrolyte, a dramatic difference between NMC and LCO cells is observed. A better capacity retention results when water is added to NMC full cells. However, a worse capacity fade occurred for LCO full cells. It is speculated that water may oxidize on the cathode surface to form O_2 , which can then react with EC to form CO_2 , according to Equation 1. The NMC surface may act as a catalyst for the reaction, while this reaction appears to be prohibited in cells with LCO cathode.

5.3.4 GC results

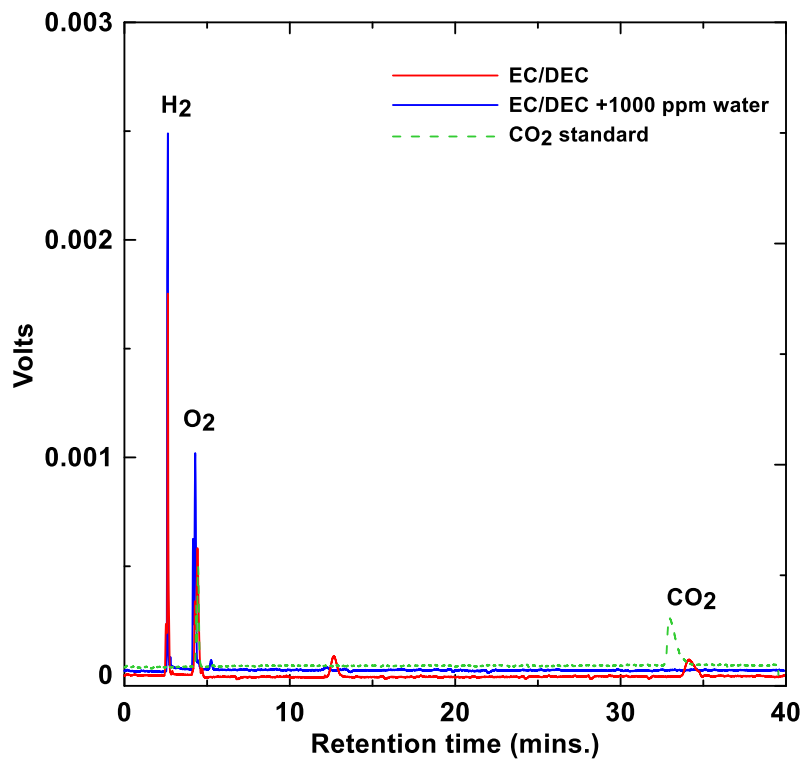


Figure 5.4 The gas chromatograms of NMC-graphite pouch cells with and without 1000 ppm water. Green dash line indicates the CO_2 standard sample. (The volume of sample is $10\mu l$)

To see if the addition of water results in increased CO_2 generation in NMC cells, GC measurements were conducted on the gas extracted from NMC-graphite pouch cells with and

without 1000 ppm water in their electrolyte. As shown in the chromatograms in Figure 5.4, the gas generated in dry cells (without water) was mainly composed of H₂, O₂ and CO₂, which is consistent with previous studies.⁽¹¹⁴⁾ If water is added to cells, the CO₂ peak disappears. This result contradicts the hypothesis of more CO₂ generation in cells with water added. This may be because the cells were not charged to a high enough potential to drive CO₂ formation. Further experiments to measure the gas generated during cycle inside cells with water additive are ongoing.

5.4 Conclusions

Full coin cells assembled by an aligner demonstrated their practicality and obtained a stable cycling performance. Karl Fischer results accurately measured the water content of water-doped electrolyte samples. The measured water loading was consistent with the designed amount. NMC-silicon alloy cells showed an enhanced cycling performance with 500 or 1000 ppm water. Moreover, the water additive has unique benefits for NMC cells but limited impacts on LCO cells. These results suggest that the generation of CO₂ is associated with specific interactions between the cathode and electrolyte. The mechanism of water chemistry in these cells is unknown, so further fundamental characterization is needed to determine the exact mechanism of how the water additive is involved in electrochemical reactions in NMC-silicon cells and its relationship to CO₂ production. The water additive might be a big breakthrough for the optimization of silicon alloy full cells. Its exceptional benefits and low cost will make it a promising additive for the future design of silicon alloy full cells.

CHAPTER 6 CONCLUSIONS AND FUTURE WORK

6.1 Conclusions

The essential goal of this thesis is to find different methods to improve the cycling performance of LIBs and SIBs. The reasons for poor cycling performance depend on many factors, such as mechanical failure or electrolyte degradation. These can be improved by many methods. In this thesis, some novel methods, such as thermoelectrochemical activation and the use of CO₂ electrolyte additive were employed to achieve good cycling performance. These results could give researchers some innovative ideas to further enhance cycle life.

In Chapter 3, inactive CoO was successfully activated by a thermoelectrochemical method. Activating CoO by sodiation at 60°C led to a significant increase in specific capacity when the resulting electrode is subsequently cycled at 30°C. A reversible capacity of nearly 300 mAh/g was achieved by using this method. Ball milling CoO with carbon black also effectively increased the activity of CoO. Combining the two activation methods resulted in significantly better cycling performance as well as higher capacity. XRD and SEM images both indicated that the thermoelectrochemical method decreases grain size and improves the conversion kinetics.

In Chapter 4, a new efficient method to measure CO₂ solubility in organic electrolytes was established by using FTIR. The results show good consistency and accuracy. It was found that CO₂ solubility in EC/DEC 1:2 v/v solutions containing 1M Li⁺ depends significantly on the electrolyte composition and in a complicated manner. CO₂ was found to be highly soluble in PC and less soluble in polar solvents like EC, but no unified theory has found to explain the correlation between the CO₂ solubility and solvent properties. The cycling performance of Si alloy cells was also shown to depend significantly on the CO₂ content in electrolyte. Electrolyte with 0.33% CO₂ provides the best cycling performance, but electrolyte with unsaturated CO₂ has limited improvement. CO₂ scavengers like DETA can increase the CO₂ solubility at a low concentration, but higher concentrations might cause phase separation.

In Chapter 5, an alignment tool was used to obtain near-perfect electrode alignment, resulting in stable cycling performance. These cells enabled a study of the effect of water additions on the cycling of full cells with Si alloy negative electrodes. Karl Fischer titration was

used to measure the water content in the electrolyte. NMC-silicon alloy cells showed an enhanced cycling performance with 500 or 1000 ppm water in the electrolyte. This is analogous performance to cells with 10% FEC. The beneficial behavior was only observed in NMC cells, but has limited impact on LCO. Cells with dual additives of 1000 ppm water and 5% FEC can protect silicon cells from losing capacity within 100 cycles. These results suggest that the water additive is consumed continuously to participate in forming a special and stable SEI to enhance the cycling, but the enhancement relies on the catalyzing activity of different cathodes.

6.2 Ongoing future work

The new thermoelectrochemical activation method has successfully activated inactive CoO. However, this is still less than half of the theoretical capacity of CoO. Further characterization of the CoO reaction mechanism is required. Specifically, a detailed investigation of the reaction products is necessary, since these are not fully understood. Complex compounds such as Na_xCoO_y will possibly form and a considerable amount of capacity could be lost accordingly. In addition, the sodiation of CoO was shown to be hindered kinetically, which can be improved by cycling at a higher temperature, but electrolyte decomposition at high temperature restricts this method. Therefore, finding a suitable electrolyte is needed for cells to operate under high temperature conditions. This method could potentially provide a massive specific capacity increase for other conversion type metal oxide materials as well.

An efficient FTIR method to determine CO_2 concentration is described in Chapter 4. This enabled the measurement of CO_2 solubility in a variety of electrolytes. Another important question is the CO_2 content change during cells cycling. It is extremely helpful to study the mechanism of how CO_2 effects silicon cycling, but it is unmeasurable by using the current FTIR set up. Thus, an in-situ FTIR holder is needed to measure the CO_2 content of electrolyte during cell cycling. A general design can be found in some references.(115) By using an in-situ method, the CO_2 concentration during cell cycling can be quantified by using the same method as the current solubility measurement. Moreover, it was found that a higher CO_2 content results in a longer cycling life. The use of a CO_2 scavenger may be a great method to increase the CO_2 solubility only if phase separation can be avoided. So some other CO_2 scavengers should be tried and investigated.(116) These compounds have impressive CO_2 absorption capacity, but their

impact on cell electrochemistry is unknown and a careful evaluation is required before the use of these compounds.

Benefits of adding water to NMC-silicon alloy full cells were discovered, but the precise working mechanism is mysterious. A fundamental study on the role of water additives needs to be conducted, and especially its interactions with different cathodes. The hypothesis is that the water additive will increase the production of CO_2 that will help to form a stable SEI on the silicon surface or it assists in LiF generation. According to previous simulation results, LiF has a special bonding effect between the lithium and fluorine in the SEI. Therefore, generation of LiF, which is probably accompanied by water decomposition during delithiation, might decrease the SEI crack formation.⁽¹¹⁷⁾ More comprehensive investigations are needed to determine the exact reaction path. In addition, H_2O might be providing an oxygen source, resulting in the improvement in cycling of NMC vs Si-alloy full cells, so other additives are worthy of trying if they will provide the oxygen free radicals and minimize other gas production like H_2 .

REFERENCES

1. Taiyou, “Global Market for Lithium-Ion Batteries - Forecast , Trends & Opportunities 2014-2020” (2020).
2. A. Yoshino, The Birth of the Lithium-Ion Battery. *Angew. Chem.* **51**, 5798–5800 (2012).
3. D. D. MacNeil, Z. Lu, Z. Chen, J. R. Dahn, A comparison of the electrode/electrolyte reaction at elevated temperatures for various Li-ion battery cathodes. *J. Power Sources.* **108**, 8–14 (2002).
4. H. Arai, S. Okada, Y. Sakurai, J. Yamaki, Reversibility of LiNiO₂ cathode. *Solid State Ion.* **95**, 275–282 (1997).
5. S. L. Wu, W. Zhang, X. Song, A. K. Shukla, G. Liu, V. Battaglia, V. Srinivasan, High rate capability of Li (Ni_{1/3}Mn_{1/3}Co_{1/3}) O₂ electrode for Li-ion batteries. *J. Electrochem. Soc.* **159**, A438–A444 (2012).
6. R. Fong, H. Al-Janby, J. R. Dahn, Carbonaceous electrodes for lithium cells (1991).
7. A. R. Kamali, D. J. Fray, Review on carbon and silicon based materials as anode materials for lithium ion batteries. *J. New Mater. Electrochem. Syst.* **13**, 147–160 (2010).
8. H. Kim, E. J. Lee, Y. K. Sun, Recent advances in the Si-based nanocomposite materials as high capacity anode materials for lithium ion batteries. *Mater. Today.* **17**, 285–297 (2014).
9. C. K. Chan, H. Peng, G. Liu, K. McIlwrath, X. F. Zhang, R. A. Huggins, Y. Cui, High-performance lithium battery anodes using silicon nanowires. *Nat. Nanotechnol.* **3**, 31 (2008).
10. T. Song, H. Cheng, H. Choi, J.-H. Lee, H. Han, D. H. Lee, D. S. Yoo, M.-S. Kwon, J.M. Choi, S. G. Doo, Si/Ge double-layered nanotube array as a lithium ion battery anode. *ACS Nano.* **6**, 303–309 (2011).
11. M. Pharr, K. Zhao, X. Wang, Z. Suo, J. J. Vlassak, Kinetics of initial lithiation of crystalline silicon electrodes of lithium-ion batteries. *Nano Lett.* **12**, 5039–5047 (2012).
12. Y.-T. Zheng, M. He, G. Cheng, Z. Zhang, F.-Z. Xuan, Z. Wang, The mechanism of carbon-addition-enhanced electrochemical kinetics. *Chem. Phys. Lett.* **732**, 136665 (2019).

13. X. Shen, Z. Tian, R. Fan, L. Shao, D. Zhang, G. Cao, L. Kou, Y. Bai, Research progress on silicon/carbon composite anode materials for lithium-ion battery. *J. Energy Chem.* **27**, 1067–1090 (2018).
14. N. Liu, Z. Lu, J. Zhao, M. T. McDowell, H.-W. Lee, W. Zhao, Y. Cui, A pomegranate-inspired nanoscale design for large-volume-change lithium battery anodes. *Nat. Nanotechnol.* **9**, 187 (2014).
15. M. N. Obrovac, V. L. Chevrier, Alloy Negative Electrodes for Li-Ion Batteries. *Chem. Rev.* **114**, 11444–11502 (2014).
16. M. N. Obrovac, L. Christensen, D. B. Le, J. R. Dahn, Alloy design for lithium-ion battery anodes. *J. Electrochem. Soc.* **154**, A849–A855 (2007).
17. M. S. Ding, K. Xu, S. Zhang, T. R. Jow, Liquid/solid phase diagrams of binary carbonates for lithium batteries part II. *J. Electrochem. Soc.* **148**, A299–A304 (2001).
18. D. R. Lide, *Handbook of organic solvents*, CRC Press, 1994.
19. M. C. Smart, B. V Ratnakumar, S. Surampudi, Use of organic esters as cosolvents in electrolytes for lithium-ion batteries with improved low temperature performance. *J. Electrochem. Soc.* **149**, A361–A370 (2002).
20. K. Tasaki, Solvent decompositions and physical properties of decomposition compounds in Li-ion battery electrolytes studied by DFT calculations and molecular dynamics simulations. *J. Phys. Chem. B.* **109**, 2920–2933 (2005).
21. J. O. Besenhard, *Handbook of battery materials*, John Wiley & Sons, 2008.
22. K. Xu, Nonaqueous liquid electrolytes for lithium-based rechargeable batteries. *Chem. Rev.* **104**, 4303–4418 (2004).
23. I. Yoshimatsu, T. Hirai, J. Yamaki, Lithium electrode morphology during cycling in lithium cells. *J. Electrochem. Soc.* **135**, 2422–2427 (1988).
24. L. Gireaud, S. Grugeon, S. Laruelle, S. Pilard, J.-M. Tarascon, Identification of Li battery electrolyte degradation products through direct synthesis and characterization of alkyl carbonate salts. *J. Electrochem. Soc.* **152**, A850–A857 (2005).

25. L. Ma, S. L. Glazier, R. Petibon, J. Xia, J. M. Peters, Q. Liu, J. Allen, R. N. C. Doig, J. R. Dahn, A guide to ethylene carbonate-free electrolyte making for Li-ion cells. *J. Electrochem. Soc.* **164**, A5008–A5018 (2017).
26. R. Petibon, C. P. Aiken, N. N. Sinha, J. C. Burns, H. Ye, C. M. VanElzen, G. Jain, S. Trussler, J. R. Dahn, Study of electrolyte additives using electrochemical impedance spectroscopy on symmetric cells. *J. Electrochem. Soc.* **160**, A117–A124 (2013).
27. C. G. Barlowz, Reaction of water with hexafluorophosphates and with Li bis (perfluoroethylsulfonyl) imide salt. *Electrochem. Solid State Lett.* **2**, 362–364 (1999).
28. G. D. Smith, O. Borodin, J. J. Magda, R. H. Boyd, Y. Wang, J. E. Bara, S. Miller, D. L. Gin, R. D. Noble, A comparison of fluoroalkyl-derivatized imidazolium: TFSI and alkyl-derivatized imidazolium: TFSI ionic liquids: a molecular dynamics simulation study. *Phys. Chem. Chem. Phys.* **12**, 7064–7076 (2010).
29. S. Zhang, M. S. Ding, K. Xu, J. Allen, T. R. Jow, Understanding solid electrolyte interface film formation on graphite electrodes. *Electrochem. Solid State Lett.* **4**, A206–A208 (2001).
30. L. El Ouatani, R. Dedryvere, C. Siret, P. Biensan, S. Reynaud, P. Iratçabal, D. Gonbeau, The effect of vinylene carbonate additive on surface film formation on both electrodes in Li-ion batteries. *J. Electrochem. Soc.* **156**, A103–A113 (2009).
31. N.-S. Choi, K. H. Yew, K. Y. Lee, M. Sung, H. Kim, S.-S. Kim, Effect of fluoroethylene carbonate additive on interfacial properties of silicon thin-film electrode. *J. Power Sources.* **161**, 1254–1259 (2006).
32. M. Armand, Polymer solid electrolytes-an overview. *Solid State Ion.* **9**, 745–754 (1983).
33. R. C. Agrawal, G. P. Pandey, Solid polymer electrolytes: materials designing and all-solid-state battery applications: an overview. *J. Phys. D.* **41**, 223001 (2008).
34. D. E. Fenton, Complexes of alkali metal ions with poly (ethylene oxide). *Polymer.* **14**, 589 (1973).
35. J. Mindemark, M. J. Lacey, T. Bowden, D. Brandell, Beyond PEO—alternative host materials for Li⁺-conducting solid polymer electrolytes. *Prog. Polym. Sci.* **81**, 114–143

- (2018).
36. W. Wiczorek, J. R. Stevens, Z. Florjańczyk, Composite polyether based solid electrolytes. The Lewis acid-base approach. *Solid State Ion.* **85**, 67–72 (1996).
 37. E. Peled, D. Golodnitsky, C. Menachem, D. Bar-Tow, An advanced tool for the selection of electrolyte components for rechargeable lithium batteries. *J. Electrochem. Soc.* **145**, 3482–3486 (1998).
 38. E. Nakamura, I. Kuwajima, Fluoride catalyzed addition of silylacetylenes to carbonyl compounds. *Angew. Chem.* **15**, 498–499 (1976).
 39. S. S. Zhang, A review on electrolyte additives for lithium-ion batteries. *J. Power Sources.* **162**, 1379–1394 (2006).
 40. P. Novák, D. Goers, L. Hardwick, M. Holzzapfel, W. Scheifele, J. Ufheil, A. Würsig, Advanced in situ characterization methods applied to carbonaceous materials. *J. Power Sources.* **146**, 15–20 (2005).
 41. M. Inaba, H. Tomiyasu, A. Tasaka, S.-K. Jeong, Z. Ogumi, Atomic force microscopy study on the stability of a surface film formed on a graphite negative electrode at elevated temperatures. *Langmuir.* **20**, 1348–1355 (2004).
 42. E. Peled, D. B. Tow, A. Merson, A. Gladkich, L. Burstein, D. Golodnitsky, Composition, depth profiles and lateral distribution of materials in the SEI built on HOPG-TOF SIMS and XPS studies. *J. Power Sources.* **97**, 52–57 (2001).
 43. M. A. McArthur, S. Trussler, J. R. Dahn, In situ investigations of SEI layer growth on electrode materials for lithium-ion batteries using spectroscopic ellipsometry. *J. Am. Chem. Soc.* **159**, A198–A207 (2012).
 44. D. Aurbach, Review of selected electrode–solution interactions which determine the performance of Li and Li ion batteries. *J. Power Sources.* **89**, 206–218 (2000).
 45. C. Wang, A. J. Appleby, F. E. Little, Charge–discharge stability of graphite anodes for lithium-ion batteries. *J. Electrochem. Soc.* **497**, 33–46 (2001).
 46. A. J. Smith, J. C. Burns, X. Zhao, D. Xiong, J. R. Dahn, A high precision coulometry study

- of the SEI growth in Li/graphite cells. *J. Electrochem. Soc.* **158**, A447–A452 (2011).
47. P. M. Attia, S. Das, S. J. Harris, M. Z. Bazant, W. C. Chueh, Electrochemical Kinetics of SEI Growth on Carbon Black: Part I. Experiments. *J. Electrochem. Soc.* **166**, E97–E106 (2019).
 48. X. Yuan, H. Liu, J. Zhang, *Lithium-ion batteries: advanced materials and technologies*, CRC press, 2011.
 49. D. Aurbach, The Correlation Between Surface Chemistry, Surface Morphology, and Cycling Efficiency of Lithium Electrodes in a Few Polar Aprotic Systems. *J. Electrochem. Soc.* **136**, 3198 (1989).
 50. L. J. Krause, V. L. Chevrier, L. D. Jensen, T. Brandt, The Effect of Carbon Dioxide on the Cycle Life and Electrolyte Stability of Li-Ion Full Cells Containing Silicon Alloy. *J. Electrochem. Soc.* **164**, A2527–A2533 (2017).
 51. K. Schroder, J. Alvarado, T. A. Yersak, J. Li, N. Dudney, L. J. Webb, Y. S. Meng, K. J. Stevenson, The Effect of Fluoroethylene Carbonate as an Additive on the Solid Electrolyte Interphase on Silicon Lithium-Ion Electrodes. *Chem. Mater.* **27**, 5531–5542 (2015).
 52. K. Takeno, M. Ichimura, K. Takano, J. Yamaki, Influence of cycle capacity deterioration and storage capacity deterioration on Li-ion batteries used in mobile phones. *J. Power Sources.* **142**, 298–305 (2005).
 53. E. Endo, M. Ata, K. Sekai, K. Tanaka, Spin trapping study of gradual decomposition of electrolyte solutions for lithium secondary batteries. *J. Electrochem. Soc.* **146**, 49–53 (1999).
 54. L. Bodenes, R. Naturel, H. Martinez, R. Dedryvère, M. Menetrier, L. Croguennec, J.-P. Pérès, C. Tessier, F. Fischer, Lithium secondary batteries working at very high temperature: Capacity fade and understanding of aging mechanisms. *J. Power Sources.* **236**, 265–275 (2013).
 55. A. R. Armstrong, A. J. Paterson, A. D. Robertson, P. G. Bruce, Nonstoichiometric Layered $\text{Li}_x\text{Mn}_y\text{O}_2$ with a High Capacity for Lithium Intercalation/Deintercalation. *Chem. Mater.* **14**, 710–719 (2002).

56. T. Waldmann, B.-I. Hogg, M. Wohlfahrt-Mehrens, Li plating as unwanted side reaction in commercial Li-ion cells—A review. *J. Power Sources*. **384**, 107–124 (2018).
57. Z. Yan, M. N. Obrovac, Electrolyte Reactivity on Graphite and Copper as Measured in Lithium Double Half Cells. *J. Electrochem. Soc.* **164**, A2977–A2986 (2017).
58. Z. Mao, M. Farkhondeh, M. Pritzker, M. Fowler, Z. Chen, M. Safari, Model-based prediction of composition of an unknown blended lithium-ion battery cathode. *J. Electrochem. Soc.* **162**, A716–A721 (2015).
59. K. Mizushima, P. C. Jones, P. J. Wiseman, J. B. Goodenough, Li_xCoO_2 ($0 < x < 1$): A new cathode material for batteries of high energy density. *Mater. Res. Bull.* **15**, 783–789 (1980).
60. B. Jache, P. Adelhelm, Use of Graphite as a Highly Reversible Electrode with Superior Cycle Life for Sodium-Ion Batteries by Making Use of Co-Intercalation Phenomena. *Angew. Chem.* **53**, 10169–10173 (2014).
61. M. D. Slater, D. Kim, E. Lee, C. S. Johnson, Sodium-ion batteries. *Adv. Funct. Mater.* **23**, 947–958 (2013).
62. G. Hasegawa, K. Kanamori, N. Kannari, J. Ozaki, K. Nakanishi, T. Abe, Hard Carbon Anodes for Na-Ion Batteries: Toward a Practical Use. *ChemElectroChem.* **2**, 1917–1920 (2015).
63. D. A. Stevens, J. R. Dahn, An In Situ Small-Angle X-Ray Scattering Study of Sodium Insertion into a Nanoporous Carbon Anode Material within an Operating Electrochemical Cell. *J. Electrochem. Soc.* **147**, 4428 (2000).
64. K. Gotoh, T. Ishikawa, S. Shimadzu, N. Yabuuchi, S. Komaba, K. Takeda, A. Goto, K. Deguchi, S. Ohki, K. Hashi, NMR study for electrochemically inserted Na in hard carbon electrode of sodium ion battery. *J. Power Sources*. **225**, 137–140 (2013).
65. Y. Lee, D.-W. Kim, J. K. Lee, W. Choi, Carbon-coated $\text{Li}_4\text{Ti}_5\text{O}_{12}$ as anode material for sodium-ion batteries. *J. Nanosci. Nanotechnol.* **15**, 7049–7053 (2015).
66. R. Fielden and M. N. Obrovac, Low Voltage Sodium Intercalation in $\text{Na}_x\text{Ni}_{x/2}\text{Ti}_{1-x/2}\text{O}_2$ ($0.5 \leq x \leq 1.0$). *J. Electrochem. Soc.* **161**, A1158–A1163 (2014).

67. B. D. Cullity, *Elements of X-ray diffraction*, Addison-Wesley Pub. Co., Reading, Mass., 1956.
68. B. D. Cullity, *Elements of X-ray Diffraction*, New Jersey: Prentice hall, 2001.
69. L. Zheng, R. A. Dunlap, M. N. Obrovac, The Electrochemical Reaction Mechanism of Tin Phosphide with Sodium. *J. Electrochem. Soc.* **163**, A1188–A1191 (2016).
70. C. R. Brundle, C. A. Evans, S. Wilson, *Encyclopedia of materials characterization: surfaces, interfaces, thin films*, Gulf Professional Publishing, 1992.
71. S. A. Khan, S. B. Khan, L. U. Khan, A. Farooq, K. Akhtar, A. M. Asiri, in *Handbook of Materials Characterization* (Springer, 2018), pp. 317–344.
72. L. Ellis, Doctoral thesis, Dalhousie (2018).
73. M. Ammam, *Applications of Nernst Equation: Basic Concepts with Resolved Questions and Problems (Section 6)* (2018).
74. T. D. Hatchard, P. Bissonnette, M. N. Obrovac, Phenolic resin as an inexpensive high performance binder for li-ion battery alloy negative electrodes. *J. Electrochem. Soc.* **163**, A2035–A2039 (2016).
75. M. Ender, A. Weber, I.-T. Ellen, Analysis of three-electrode setups for AC-impedance measurements on lithium-ion cells by FEM simulations. *J. Electrochem. Soc.* **159**, A128–A136 (2011).
76. T. Zheng, Y. Liu, E. W. Fuller, S. Tseng, U. Von Sacken, J. R. Dahn, Lithium insertion in high capacity carbonaceous materials. *J. Electrochem. Soc.* **142**, 2581–2590 (1995).
77. B. R. Long, S. G. Rinaldo, K. G. Gallagher, D. W. Dees, S. E. Trask, B. J. Polzin, A. N. Jansen, D. P. Abraham, I. Bloom, J. Bareño, Enabling high-energy, high-voltage lithium-ion cells: Standardization of coin-cell assembly, electrochemical testing, and evaluation of full cells. *J. Electrochem. Soc.* **163**, A2999–A3009 (2016).
78. V. Murray, D. S. Hall, J. R. Dahn, A Guide to Full Coin Cell Making for Academic Researchers. *J. Electrochem. Soc.* **166**, A329–A333 (2019).

79. C. C. Goosen, Carburetor throttle valve method and apparatus (1983).
80. A. T. Cheng, Method and apparatus for dispersing a gas into a liquid (1990).
81. M. Anouti, Y. R. Dougassa, C. Tessier, L. El Ouatani, J. Jacquemin, Low pressure carbon dioxide solubility in pure electrolyte solvents for lithium-ion batteries as a function of temperature. Measurement and prediction. *J. Chem. Thermodyn.* **50**, 71–79 (2012).
82. H.-J. Muhr, R. Rohner, “Good Titration Practice TM in Karl Fischer Titration” (2011), (available <http://fr.mt.com/dam/LabDiv/Campaigns/TestingLabs2013/moisture/package/gtp-karl-fischer-EN.pdf>) at
83. M. Dahbi, N. Yabuuchi, K. Kubota, K. Tokiwa, S. Komaba, Negative electrodes for Na-ion batteries. *Phys. Chem. Chem. Phys.* **16**, 15007–15028 (2014).
84. Y. Jiang, M. Hu, D. Zhang, T. Yuan, W. Sun, B. Xu, M. Yan, Transition metal oxides for high performance sodium ion battery anodes. *Nano Energy.* **5**, 60 (2014).
85. F. Klein, B. Jache, A. Bhide, P. Adelhelm, Conversion reactions for sodium-ion batteries. *Phys. Chem. Chem. Phys.* **15**, 15876 (2013).
86. P. Poizot, S. Laruelle, S. Grugeon, L. Dupont, J. M. Tarascon, Nano-sized transition-metal oxides as negative-electrode materials for lithium-ion batteries. *Nature.* **407**, 496 (2000).
87. R. Thorpe, R. A. Bartynski, Doctoral thesis, The state University of New Jersey, New Jersey (2016).
88. D. Andre, S.-J. Kim, P. Lamp, S. F. Lux, F. Maglia, O. Paschos, B. Stiaszny, Future generations of cathode materials: an automotive industry perspective. *J. Mater. Chem. A.* **3**, 6709–6732 (2015).
89. L. Croguennec, M. R. Palacin, Recent achievements on inorganic electrode materials for lithium ion batteries. *J. Am. Chem. Soc.* **137**, 3140 (2015).
90. S. Laruelle, S. Grugeon, P. Poizot, M. Dollé, L. Dupont, J.-M. Tarascon, On the Origin of the Extra Electrochemical Capacity Displayed by MO/Li Cells at Low Potential. *J. Electrochem. Soc.* **149**, A627 (2002).

91. A. Ponrouch, P. L. Taberna, P. Simon, M. R. Palacin, On the origin of the extra capacity at low potential in materials for Li batteries reacting through conversion reaction. *Electrochim. Acta.* **61**, 13–18 (2012).
92. G. Gachot, S. Grugeon, M. Armand, S. Pilard, P. Guenot, J. M. Tarascon, S. Laruelle, Deciphering the multi-step degradation mechanisms of carbonate-based electrolyte in Li batteries. *J. Power Sources.* **178**, 409–421 (2008).
93. X. Li, L. Qiao, D. Li, X. Wang, W. Xie, D. He, Three-dimensional network structured α -Fe₂O₃ made from a stainless steel plate as a high-performance electrode for lithium ion batteries. *J. Mater. Chem. A.* **1**, 6400 (2013).
94. J. Y. Kwon, J. H. Ryu, Y. S. Jung, S. M. Oh, Thermo-electrochemical activation of Cu₃Sn negative electrode for lithium-ion batteries. *J. Alloy. Compd.* **509**, 7595 (2011).
95. J. H. Ku, Y. S. Jung, K. T. Lee, C. H. Kim, S. M. Oh, Thermo-electrochemically Activated MoO Powder Electrode for Lithium Secondary Batteries. *J. Electrochem. Soc.* **156**, A688 (2009).
96. Y. S. Jung, K. T. Lee, J. H. Kim, J. Y. Kwon, S. M. Oh, Thermo-electrochemical activation of an In-Cu intermetallic electrode for the anode in lithium secondary batteries. *Adv. Funct. Mater.* **18**, 3010 (2008).
97. F. Badway, F. Cosandey, N. Pereira, G. G. Amatucci, Carbon metal fluoride nanocomposites - High-capacity reversible metal fluoride conversion materials as rechargeable positive electrodes for Li batteries. *J. Electrochem. Soc.* **150**, A1318–A1327 (2003).
98. B. N. Wilkes, Z. L. Brown, L. J. Krause, M. Triemert, M. N. Obrovac, The Electrochemical Behavior of Polyimide Binders in Li and Na Cells. *J. Electrochem. Soc.* **163**, A364–A372 (2016).
99. K. E. Gregorczyk, Y. Liu, J. P. Sullivan, G. W. Rubloff, In Situ Transmission Electron Microscopy Study of Electrochemical Lithiation and Delithiation Cycling of the Conversion Anode RuO₂. *ACS Nano.* **7**, 6354–6360 (2013).

100. S.-W. Kim, D.-H. Seo, X. Ma, G. Ceder, K. Kang, Electrode Materials for Rechargeable Sodium-Ion Batteries: Potential Alternatives to Current Lithium-Ion Batteries. *Adv. Energy Mater.* **2**, 710 (2012).
101. F. L. Kai He Yizhou Zhu, Xiqian Yu, Jing Li, Ruoqian Lin, Dennis Nordlund, Tsu-Chien Weng, Ryan M. Richards, Xiao-Qing Yang, Marca M. Doeff, *Nano Lett.*, **15**, 5755–5763 (2015).
102. F. Badway, F. Cosandey, N. Pereira, G. G. Amatucci, Carbon Metal Fluoride Nanocomposites. *J. Am. Chem. Soc.* **150**, A1318 (2003).
103. M. Onuki, S. Kinoshita, Y. Sakata, M. Yanagidate, Y. Otake, M. Ue, M. Deguchi, Identification of the source of evolved gas in Li-ion batteries using# 2# 1-labeled solvents. *J. Electrochem. Soc.* **155**, A794–A797 (2008).
104. B. Strehle, S. Solchenbach, M. Metzger, K. U. Schwenke, H. A. Gasteiger, The Effect of CO₂ on Alkyl Carbonate Trans-Esterification during Formation of Graphite Electrodes in Li-Ion Batteries. *J. Electrochem. Soc.* **164**, A2513–A2526 (2017).
105. S. Solchenbach, M. Wetjen, D. Pritzl, K. U. Schwenke, H. A. Gasteiger, Lithium Oxalate as Capacity and Cycle-Life Enhancer in LNMO/Graphite and LNMO/SiG Full Cells. *J. Electrochem. Soc.* **165**, A512–A524 (2018).
106. J. Li, Z. Du, R. E. Ruther, S. J. An, L. A. David, K. Hays, M. Wood, N. D. Phillip, Y. Sheng, C. Mao, Toward low-cost, high-energy density, and high-power density lithium-ion batteries. *Jom.* **69**, 1484–1496 (2017).
107. F. Blanchard, B. Carré, F. Bonhomme, P. Biensan, D. Lemordant, Solubility of carbon dioxide in alkylcarbonates and lactones. *Can. J. Chem.* **81**, 385–391 (2003).
108. Y. R. Dougassa, J. Jacquemin, L. El Ouatani, C. Tessier, M. Anouti, Viscosity and carbon dioxide solubility for LiPF₆, LiTFSI, and LiFAP in alkyl carbonates: lithium salt nature and concentration effect. *J. Phys. Chem. B.* **118**, 3973–3980 (2014).
109. P. Muchan, J. Narku-Tetteh, C. Saiwan, R. Idem, T. Supap, Effect of number of amine groups in aqueous polyamine solution on carbon dioxide (CO₂) capture activities. *Sep. Purif.*

- Technol.* **184**, 128–134 (2017).
110. A. Wuersig, W. Scheifele, P. Novák, CO₂ gas evolution on cathode materials for lithium-ion batteries. *J. Electrochem. Soc.* **154**, A449–A454 (2007).
 111. R. Jung, M. Metzger, F. Maglia, C. Stinner, H. A. Gasteiger, Oxygen release and its effect on the cycling stability of LiNi_xMn_yCo_zO₂ (NMC) cathode materials for Li-ion batteries. *J. Electrochem. Soc.* **164**, A1361–A1377 (2017).
 112. S. A. Freunberger, Y. Chen, Z. Peng, J. M. Griffin, L. J. Hardwick, F. Bardé, P. Novák, P. G. Bruce, Reactions in the rechargeable lithium–O₂ battery with alkyl carbonate electrolytes. *J. Am. Chem. Soc.* **133**, 8040–8047 (2011).
 113. D. Xiong, Doctoral thesis, Dalhousie Univeristy (2017).
 114. J. C. Burns, N. N. Sinha, G. Jain, H. Ye, C. M. VanElzen, E. Scott, A. Xiao, W. M. Lamanna, J. R. Dahn, The Impact of Intentionally Added Water to the Electrolyte of Li-ion Cells I. Cells with Graphite Negative Electrodes. *J. Electrochem. Soc.* **160**, A2281–A2287 (2013).
 115. J. Y. Ye, Y. X. Jiang, T. Sheng, S. G. Sun, In-situ FTIR spectroscopic studies of electrocatalytic reactions and processes. *Nano Energy.* **29**, 414–427 (2016).
 116. S. Supasitmongkol, P. Styring, High CO₂ solubility in ionic liquids and a tetraalkylammonium-based poly(ionic liquid). *Energy Environ. Sci.* **3**, 1961–1972 (2010).
 117. A. Schiele, B. Breitung, T. Hatsukade, B. B. Berkes, P. Hartmann, J. Janek, T. Brezesinski, The critical role of fluoroethylene carbonate in the gassing of silicon anodes for lithium-ion batteries. *ACS Energy Lett.* **2**, 2228–2233 (2017).

APPENDIX THE COPYRIGHT PERMISSION LETTER

Copyright Information

The copyright information is outlined in this section, with the permission granted for Figures used in this thesis.

This is not an invoice

Order Details

Journal of the Electrochemical Society

Billing Status:
N/A

Order detail ID: 72012807
ISSN: 1945-7111
Publication Type: e-Journal
Volume:
Issue:
Start page:
Publisher: Electrochemical Society
Author/Editor: Electrochemical Society

Permission Status:  **Granted**
Permission type: Republish or display content
Type of use: Republish in a thesis/dissertation
Order License Id: 4671970063212

Hide details

Requestor type	Author of requested content
Format	Print, Electronic
Portion	chart/graph/table/figure
Number of charts/graphs/tables/figures	2
The requesting person/organization	HAONAN YU
Title or numeric reference of the portion(s)	Schematic model of lithium ion battery cell
Title of the article or chapter the portion is from	Introduction
Editor of portion(s)	N/A
Author of portion(s)	Haonan Yu
Volume of serial or monograph	93
Page range of portion	11-12
Publication date of portion	Aug
Rights for	Main product
Duration of use	Current edition and up to 15 years
Creation of copies for the disabled	no
With minor editing privileges	yes
For distribution to	Canada
In the following language(s)	Original language of publication
With incidental promotional use	yes
Lifetime unit quantity of new product	Up to 499
Title	Cycling performance of batteries
Institution name	DALHOUSIE University
Expected presentation date	Nov 2019

Note: This item was invoiced separately through our [RightsLink service](#). [More info](#)

\$ 0.00

Order detail ID: 72012825
 ISSN: 0013-4651
 Publication Type: Journal
 Volume:
 Issue:
 Start page:
 Publisher: ELECTROCHEMICAL SOCIETY,
 Author/Editor: ELECTROCHEMICAL SOCIETY

Permission Status:  **Granted**
 Permission type: Republish or display content
 Type of use: Republish in a thesis/dissertation
 Order License Id: 4671970064360

Hide details

Requestor type	Author of requested content
Format	Print, Electronic
Portion	chart/graph/table/figure
Number of charts/graphs/tables/figures	2
The requesting person/organization	HAONAN YU
Title or numeric reference of the portion(s)	Proposed mechanism for the oxidation of EC with reactive oxygen
Title of the article or chapter the portion is from	Cycling performance of batteries
Editor of portion(s)	N/A
Author of portion(s)	Haonan Yu
Volume of serial or monograph	93
Page range of portion	15
Publication date of portion	Nov. 2019
Rights for	Main product
Duration of use	Current edition and up to 15 years
Creation of copies for the disabled	no
With minor editing privileges	yes
For distribution to	Canada
In the following language(s)	Original language of publication
With incidental promotional use	yes
Lifetime unit quantity of new product	Up to 499
Title	Cycling performance of batteries
Institution name	DALHOUSIE Univeristy
Expected presentation date	Nov 2019

Note: This item was invoiced separately through our [RightsLink service](#). [More info](#)

\$ 0.00

SPRINGER NATURE LICENSE
TERMS AND CONDITIONS

Sep 24, 2019

This Agreement between DALHOUSIE University – HAONAN YU ("You") and Springer Nature ("Springer Nature") consists of your license details and the terms and conditions provided by Springer Nature and Copyright Clearance Center.

License Number	4671970860279
License date	Sep 18, 2019
Licensed Content Publisher	Springer Nature
Licensed Content Publication	Nature Materials
Licensed Content Title	Detection of subsurface structures underneath dendrites formed on cycled lithium metal electrodes
Licensed Content Author	Katherine J. Harry, Daniel T. Hallinan, Dilworth Y. Parkinson, Alastair A. MacDowell, Nitash P. Balsara
Licensed Content Date	Nov 24, 2013
Licensed Content Volume	13
Licensed Content Issue	1
Type of Use	Thesis/Dissertation
Requestor type	non-commercial (non-profit)
Format	print and electronic
Portion	figures/tables/illustrations
Number of figures/tables/illustrations	1
High-res required	no
Will you be translating?	no
Circulation/distribution	1 - 29
Author of this Springer Nature content	no
Title	Cycling performance of batteries
Institution name	DALHOUSIE University
Expected presentation date	Nov 2019
Portions	Cross-section images of dendrite growth. The current density increases from a (0 C/cm ²), b (9 C/cm ²), c (84 C/cm ²) to d (296 C/cm ²).
Requestor Location	DALHOUSIE University 1030 South Park Street 419 Halifax, NS B3H2W3 Canada Attn: DALHOUSIE University
Total	0.00 CAD
Terms and Conditions	

Title: Research Development on
Sodium-Ion Batteries
Author: Naoaki Yabuuchi, Kei Kubota,
Mouad Dahbi, et al
Publication: Chemical Reviews
Publisher: American Chemical Society
Date: Dec 1, 2014
Copyright © 2014, American Chemical Society

LOGINLOGIN

If you're a **copyright.com user**, you can login to RightsLink using your copyright.com credentials. Already a **RightsLink user** or want to [learn more?](#)

PERMISSION/LICENSE IS GRANTED FOR YOUR ORDER AT NO CHARGE

This type of permission/license, instead of the standard Terms & Conditions, is sent to you because no fee is being charged for your order. Please note the following:

- Permission is granted for your request in both print and electronic formats, and translations.
- If figures and/or tables were requested, they may be adapted or used in part.
- Please print this page for your records and send a copy of it to your publisher/graduate school.
- Appropriate credit for the requested material should be given as follows: "Reprinted (adapted) with permission from (COMPLETE REFERENCE CITATION). Copyright (YEAR) American Chemical Society." Insert appropriate information in place of the capitalized words.
- One-time permission is granted only for the use specified in your request. No additional uses are granted (such as derivative works or other editions). For any other uses, please submit a new request.

If credit is given to another source for the material you requested, permission must be obtained from that source.

**JOHN WILEY AND SONS LICENSE
TERMS AND CONDITIONS**

Sep 24, 2019

This Agreement between DALHOUSIE Univeristy -- HAONAN YU ("You") and John Wiley and Sons ("John Wiley and Sons") consists of your license details and the terms and conditions provided by John Wiley and Sons and Copyright Clearance Center.

License Number	4671990803761
License date	Sep 18, 2019
Licensed Content Publisher	John Wiley and Sons
Licensed Content Publication	Angewandte Chemie International Edition
Licensed Content Title	A Layered P2- and O3-Type Composite as a High-Energy Cathode for Rechargeable Sodium-Ion Batteries
Licensed Content Author	Haoshen Zhou, Masayoshi Ishida, Mingwei Chen, et al
Licensed Content Date	Apr 1, 2015
Licensed Content Volume	54
Licensed Content Issue	20
Licensed Content Pages	6
Type of use	Dissertation/Thesis
Requestor type	University/Academic
Format	Print and electronic
Portion	Figure/table
Number of figures/tables	1
Original Wiley figure/table number(s)	a) O3 and b) P2 structure of sodium transition metal oxide cathode materials.
Will you be translating?	No
Title of your thesis / dissertation	Cycling performance of batteries
Expected completion date	Nov 2019
Expected size (number of pages)	1
Requestor Location	DALHOUSIE Univeristy 1030 South Park Street 419 Halifax, NS B3H2W3 Canada Attn: DALHOUSIE Univeristy
Publisher Tax ID	EU826007151
Total	0.00 CAD
Terms and Conditions	